SATBAYEV UNIVERSITY

ISSN 2959-2348 (Online)

ENGINEERING JOURNAL of Satbayev University

Volume 147 (Issue 6)
December 2025

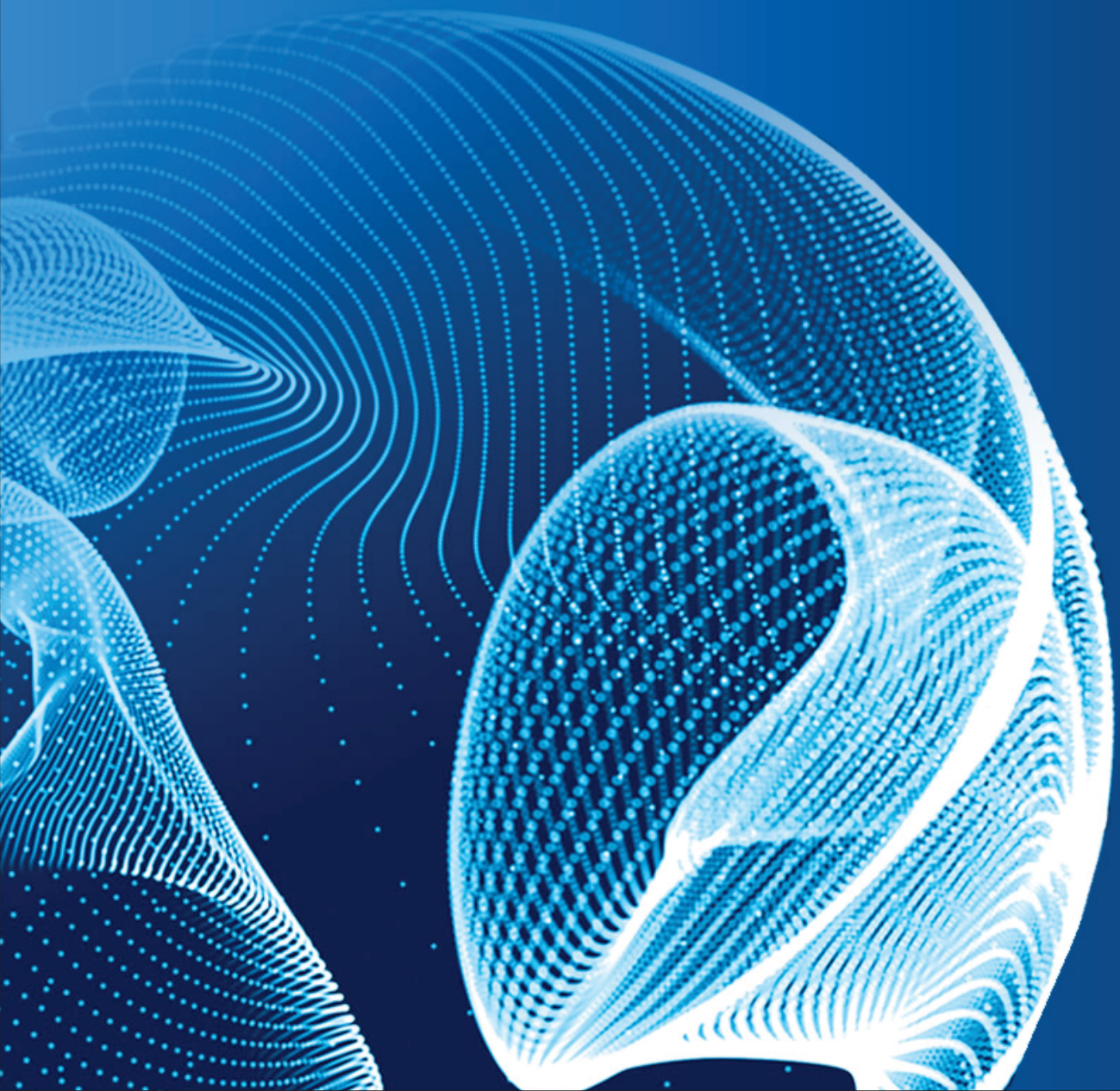

eISSN 2959-2348

eISSN 2959-2348

eISSN 2959-2348

SATBAYEV UNIVERSITY

Engineering Journal of Satbayev University

Volume 147 (2025), Issue 6, 1-7

https://doi.org/10.51301/ejsu.2025.i6.01

Investigation of electrodialysis membrane processes for sodium sulfate solutions with alkaline and acid regeneration

B.S. Baimbetov[1], V.S. Mamyachenkov[2], A.A. Dauletbakova[1*], G.Zh. Moldabayeva[1], Ye.B. Tazhiyev[1]

[1]*Satbayev University, Almaty, Kazakhstan*

[2]*Ural Federal University named after the first President of Russia B.N. Yeltsin, Yekaterinburg, Russia*

**Corresponding author: a.dauletbakova@satbayev.university*

Abstract. This article considers the possibility of processing sodium sulfate (Na_2SO_4) solutions generated in various industrial processes into valuable products - sulfuric acid (H_2SO_4) and sodium hydroxide (NaOH) using the electrodialysis method. The problem of processing sodium sulphate solutions is relevant due to their significant volume and high content of inorganic impurities, while traditional methods of purification are energy-intensive and economically inexpedient. The authors have analysed the existing methods of obtaining and processing sodium sulphate solutions by electrodialysis using MC-40, MA-41 and MB-2I membranes and Ralex BM membranes. In purpose of electrodialysis the schemes of 3-chamber and 6-section electrodialyzers using cation- and anion-exchange membranes of MC-40, MA-41 (RF) and EDC1R, EAC1R (PRC) grades were applied. The scheme of bench installation of a multichamber electrodialyzer using EDAM and EDCM membrane brands was considered. The conditions of experiments on 3 installations according to the method of probabilistic-deterministic planning of experiments by Malyshev V.P. The dependences for the first installation were obtained: the degree of conversion on the concentration of Na_2SO_4, the duration of the process on the cathodic density and the content of $MgSO_4$ impurity. Dependences of energy consumption on concentration of initial solution and current density at 3 installations allow to judge about expediency of electrodialysis process.

Keywords: *sodium sulfate, electrodialysis, membrane processes, sodium hydroxide, sulfuric acid*.

Received: 28 July 2025
Accepted: 15 December 2025
Available online: 31 December 2025

1. Introduction

In the industrial cycle of ore and concentrate processing, which involves the extensive use of reagents such as H_2SO_4 and NaOH, a low-concentration sodium sulfate solution is generated as a waste or by-product. The purification of such dilute solutions is considered economically unfeasible and energy-intensive. One of the methods for converting sodium sulfate into concentrated alkali and acid is through membrane-based electrodialysis processes [1-8] driven by an electric current.

In article [9], the process of electrodialysis of a Na_2SO_4 solution using MC-40, MA-41, and MB-2I membranes is studied, with the aim of producing concentrated solutions of alkali and acid. The sodium sulfate solution used is a by-product of the battery scrap recycling process. The authors conducted experiments using model solutions of Na_2SO_4 (0.5 mol/l), H_2SO_4 (0.005 mol/l), and NaOH (0.01 mol/l), and presented several cell configurations employing ion-exchange membranes. The best results were achieved using a three-compartment, non-flow-type electrodialyzer equipped with cation- and anion-exchange membranes. The resulting concentrations of the products were 0.34 mol/l for NaOH and 0.23 mol/l for H_2SO_4, with specific energy consumptions of 0.84 kWh/mol for NaOH and 1.10 kWh/mol for H_2SO_4. The main drawbacks of the process include low productivity and significant gas evolution in the cell compartments.

Publication [10] presents a process flow diagram for the treatment of $Na_2SO_4 \cdot 10H_2O$ precipitate via electrodialysis. This precipitate forms at temperatures of 8–10ºC. The technological scheme includes the following equipment: a three-compartment electrolyzer, with a PbO_2 anode and a stainless-steel cathode; circulation pumps; and solution storage tanks. The initial concentrations of the solutions were: sodium sulfate – 120 g/l, NaOH – 5 g/l, and H_2SO_4 – 7 g/l. Upon completion of the process, the resulting concentrations reached 150 g/l for NaOH and 182 g/l for H_2SO_4, under a current density of 2 A/dm^2 and a processing time of 5 hours. The system demonstrated a productivity of approximately 1 kg/(m^2·h) and a specific energy consumption of 7.5 kWh/kg. The authors note the following drawbacks of the process: significant gas evolution, the need for preliminary purification of the solutions from impurities, and a limitation on current density-exceeding 3 A/dm^2 is undesirable due to the potential deterioration of process parameters.

Research [11] describes the conversion of sodium sulfate into H_2SO_4 and NaOH using Ralex BM membranes. The investigation focused on the effects of current density and the concentrations of acid and alkali on membrane transport

b.baimbetov@satbayev.university; svmamyachenkov@yandex.ru; a.dauletbakova@satbayev.university; gulnara.moldabayeva@satbayev.university; y.tazhiyev@satbayev.university
Engineering Journal of Satbayev University. eISSN 2959-2348. Published by Satbayev University

efficiency. The system's productivity increased proportionally with current density and decreased as Na_2SO_4 conversion progressed. The current density in the experiments ranged from 200 to 1000 A/m^2, while the concentrations of acid and alkali varied from 0.5 to 4 N. The setup employed platinized electrodes, with a solution circulation rate of 2.5 l/h.

2. Materials and methods

Sodium sulfate solutions were prepared using analytical grade Na_2SO_4 reagent in accordance with GOST 195–77 [12]. The chemical composition of the substance used is presented in Table 1.

Table 1. Composition of initial sodium sulfate

Name of indicator	Pure for analysis
Mass fraction of sodium sulfur dioxide Na_2SO_3, %, not less than	98
Mass fraction of water-insoluble substances, %, not more than	0.003
Acidity	Shall withstand the tests outlined in s. 3.4.
Mass fraction of alkali Na_2CO_3, %, not more than	0.05
Mass fraction of thiosulfates (S_2O_3), %, not more than	0.02
Mass fraction of chlorides (Cl), %, not more than	0.005
Mass fraction of iron (Fe), %, not more than	0.0005
Mass fraction of arsenic (As), %, not more than	0.00002
Mass fraction of heavy non-ferrous metals (Pb), %, not more than	0.0005

In the present work, experiments were conducted on three setups differing in design and solution circulation schemes, in order to compare key performance indicators.

For electrodialysis of sodium sulfate solutions with $MgSO_4$ admixture to obtain H_2SO_4 and NaOH, an installation in the form of rectangular plates and frames made of Plexiglas was made. The electrodialysis process was carried out in a three-compartment apparatus (Figure 1) using MC-40 and MA-41 ion-exchange membranes [13, 14]. According to the manufacturers' specifications, the average electrical resistance of both membrane types is in the range of 10.0-11.0 Ω·cm^2.

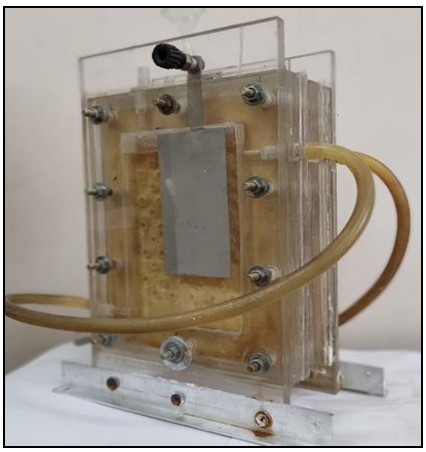

Figure 1. Electrodialyzer 3-section

The initial sodium sulfate solution, with a concentration of 20-80 g/l and supplemented with $MgSO_4$, was fed into the central (working) compartment of the apparatus. The catholyte and anolyte were prepared as follows:

– catholyte, distilled water with the addition of 2 ml of 30% NaOH solution;

– anolyte, distilled water with the addition of 2 ml of 300 g/l H_2SO_4 solution.

A platinized electrode served as the anode, with dimensions of 50×100×2 mm and an anode surface area of 37.5 cm^2; the cathode was made of stainless steel, sized 55×100×1 mm with a surface area of 41.25 cm^2.

Experiments were conducted varying the following parameters:

– current intensity from 0.4 to 1.0 A;

– electrodialysis duration from 2 to 8 hours;

– $MgSO_4$ impurity concentrations of 2, 4, 6 and 8 g/l.

Figure 2 shows an improved design of a three-compartment electrodialyzer with solution circulation and pressurized tanks. The total solution volume, including the pressurized tanks, was 600 ml.

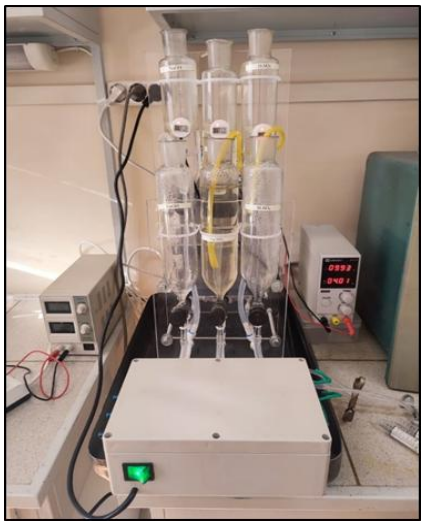

Figure 2. Electrodialysis plant with continuous circulation of solutions

Electrodialysis was performed using ion-exchange membranes EDC1R and EAC1R (PRC) [15, 16]. According to the manufacturers' data, the electrical resistance of these membranes averages 4.5-5.5 Ω·cm^2. The setup consists of six compartments arranged in the following order: cathode – cation-exchange membrane (CEM) – anion-exchange membrane (AEM) – anode – AEM – CEM – cathode. The distance between compartments is 10 mm. A platinized platinum (Pt) anode is installed in the central compartment, while iron (Fe) and titanium (Ti) cathodes are placed in the outer compartments.

Electrodialysis of sodium sulfate solutions on the pilot-scale setup was carried out in continuous circulation mode with simultaneous concentration of alkali and acid solutions (Figure 3). The volumes of H_2SO_4, NaOH, and Na_2SO_4 solutions were each 2 L. EDAM and EDCM [17] ion-exchange membranes with a specific electrical resistance of 2.5-3 Ω·cm^2 were used. A platinized electrode served as the anode, while a stainless-steel electrode was employed as the cathode.

In the last two setups, the circulation rate of electrolytes was controlled by adjusting the power supply voltage to the membrane pumps and by the electrolyte level in the pressurized tanks. The densities of the Na_2SO_4, H_2SO_4, and NaOH solutions were measured using a D6 Excellence digital densitometer.

Figure 3. Bench installation for electrodialysis of Na_2SO_4 solutions

Electrodialysis experiments with sodium sulfate solutions were conducted following the probabilistic-deterministic experimental design method developed by V.P. Malyshev [18-20].

3. Results and discussion

The conditions of experiments on electrodialysis of sodium sulfate with magnesium sulfate admixture in a 3-chamber electrodialyzer, and the results of experiments are given in Table 2.

Table 2. Conditions of experiments on electrodialysis of Na_2SO_4+$MgSO_4$ solutions

N	Na_2SO_4, g/l	$MgSO_4$, g/l	Current intensity, A	Duration, hour	$Y_{(i)}$ exp
1	20	4.00	0.60	4	63.92
2	20	4.00	0.40	2	16.01
3	20	4.00	1.00	8	93.05
4	20	4.00	0.80	6	66.7
5	40	2.00	0.60	2	34.66
6	40	2.00	0.40	8	53.1
7	40	2.00	1.00	6	53.42
8	40	2.00	0.80	4	50.67
9	60	8.00	0.60	2	13.53
10	60	8.00	0.40	8	35.55
11	60	8.00	1.00	6	48.43
12	60	8.00	0.80	4	24.61
13	80	6.00	0.60	2	22.97
14	80	6.00	0.40	8	32.35
15	80	6.00	1.00	6	39.22
16	80	6.00	0.80	4	16.48

Figure 4 presents the dependencies of the conversion degree of the solution on the initial Na_2SO_4 concentration, cathodic current density (ranging from 50 to 125 A/m^2), electrodialysis duration and $MgSO_4$ impurity content.

Electrodialysis was performed at cathode current densities, $d_{(k)}$, ranging from 50 to 125 A/m^2. According to the presented graphs, the degree of Na_2SO_4 conversion increases with both the current density and the duration of the process.

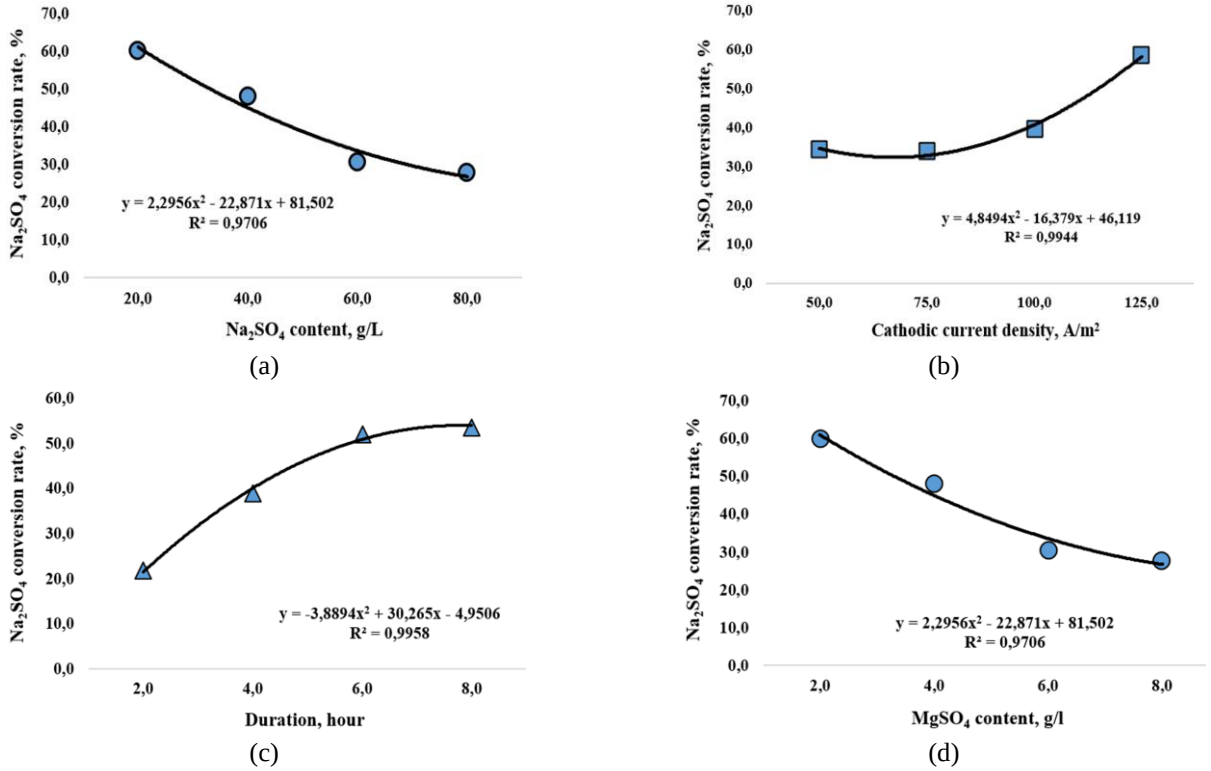

Figure 4. Dependence of the Na_2SO_4 conversion degree on various factors: (a) – initial Na_2SO_4 concentration; (b) – cathodic current density; (c) – electrodialysis duration; (d) – $MgSO_4$ impurity concentration

Figure 5 illustrates the dependence of the current strength on the duration of electrodialysis.

The gradual decrease in current strength at the end of the sodium sulfate electrodialysis process under a constant voltage is due to the reduction in salt concentration in the central compartment, which in turn leads to a decrease in the solution's electrical conductivity.

Figure 6 shows the dependence of specific energy consumption during electrodialysis of sodium sulfate solution on the initial Na_2SO_4 concentration, cathode current density, and $MgSO_4$ impurity content. Figure 6a shows that at high initial sodium sulfate concentrations (60-80 g/l), the specific energy consumption for electrodialysis is approximately 5 kWh per 1 kg of Na_2SO_4.

With an increase in current density (Figure 6b), energy consumption increases accordingly.

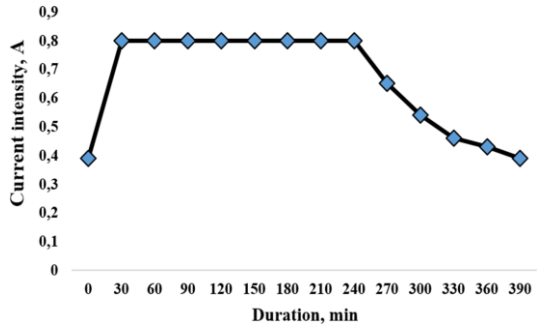

Figure 5. Dependence of current strength on the duration of Na_2SO_4 solution electrodialysis

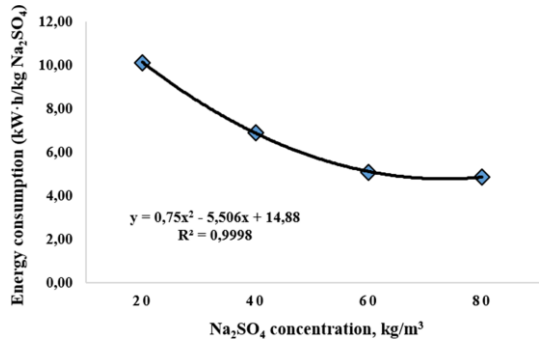

(a)

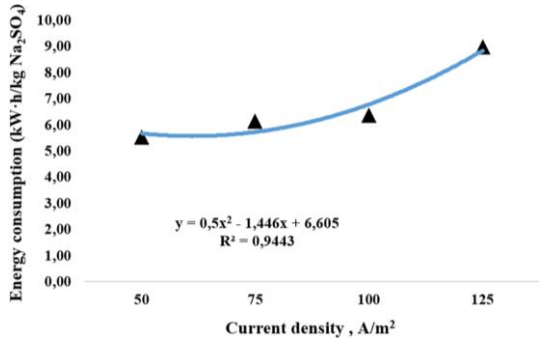

(b)

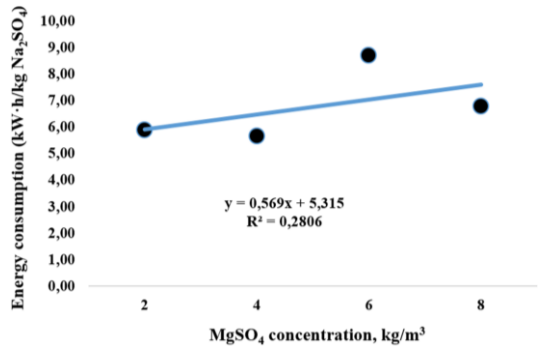

(c)

Figure 6. Dependence of specific energy consumption during electrodialysis on various factors: (a) – initial Na_2SO_4 concentration; (b) – current density; (c) – MgSO4 impurity concentration

In the circulation setup, a dependence (Figure 7) was established between energy consumption per unit mass of salt and an average current density at the platinized anode of 60 A/m^2. At sodium sulfate concentrations ranging from 60 to 150 g/l, energy consumption was found to be in the range of 4-7 kW·h/kg.

Reducing the salt concentration in the solution entering the electrodialysis leads to a significant increase in energy consumption from 7 to 34 kW·h/kg. In the apparatus the distance between the cathode and anode was 3 cm. The increase in energy consumption was attributed to the rise in electrical losses along the circuit: platinized anode – H_2SO_4 solution – anion-exchange membrane – Na_2SO_4 solution – cation-exchange membrane – NaOH solution – steel cathode. Depending on the temperature and composition of the solutions in the electrodialysis cell compartments, the total electrical resistance of the system ranged from 2.8 to 10.9 Ω.

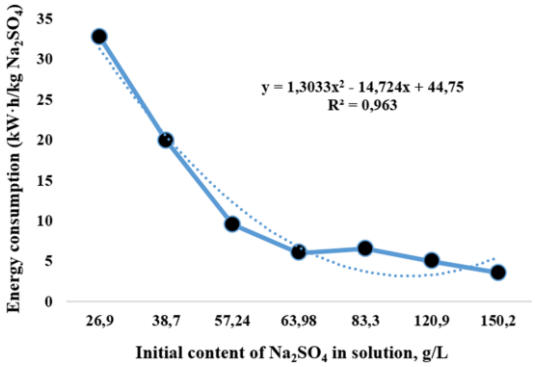

Figure 7. Dependence of specific energy consumption per 1 kg of Na_2SO_4 on the initial sodium sulfate concentration

For comparison of electrodialysis performance, experiments were conducted on a pilot-scale setup equipped with 10 pairs of ion-exchange membranes. The conditions of the sodium sulfate electrodialysis experiments, as well as the conversion degree values obtained on the pilot setup at different initial solution concentrations and current densities, are presented in Table 3.

Table 3. Conditions of experiments

N	Na_2SO_4 g/l	Current density, A/m^2	Duration, min	Na_2SO_4 conversion rate, %
1	86.3	17.02	600	8.7
2	78.8	14.15	1140	13.73
3	66.7	13.16	1080	7.20
4	61.9	23.10	300	5.53
5	79.6	118.57	240	36.53
6	50.5	60.24	300	22.92
7	39.0	89.64	300	42.33
N	NaOH circulation volume, L	H_2SO_4 circulation volume, L	Na_2SO_4 circulation volume, L	
1	14.2	14.6	13.9	
2	71.86	75.45	69.1	
3	67.19	65.92	65.68	
4	21.48	19.46	19.23	
5	17.68	12.77	12.98	
6	23.97	19.90	23.91	
7	20.94	21.51	22.17	

At duration of electrodialysis from 4 to 19 hours, consumption of initial solution of sodium sulfate (Na_2SO_4) 13.9-69.1 liters and current density 13.2-118.6 A/m^2 the degree of conversion of sodium sulfate was 5.5-42.33%. The energy consumption for the electrochemical process was 0.95-2.11 kW·h per 1 kg of Na_2SO_4.

Figure 8 shows the dependence of energy consumption for electrodialysis on the initial concentration of sodium sulfate.

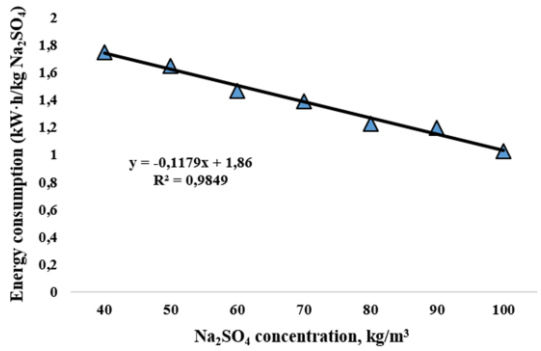

Figure 8. Dependence of energy consumption for electrodialysis on initial concentration of sodium sulfate

For predicting the required duration of the electrodialysis process of sodium sulfate solutions to achieve the desired degree of conversion, a dependence of the degree of conversion on the current density was established. Based on the data from Table 3, the values of current density and degree of conversion were recalculated using interpolation. Figure 9 presents the dependence of the degree of conversion of Na_2SO_4 on the current density at an electrodialysis duration of 1 hour and an average salt concentration of 65 g/L.

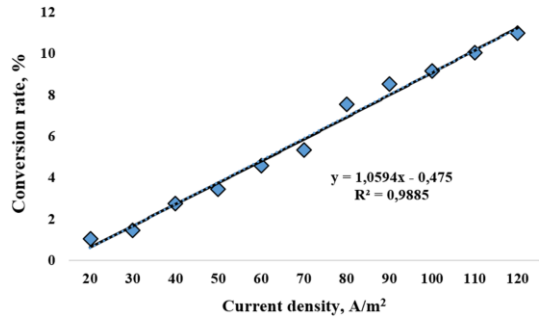

Figure 9. Dependence of conversion rate on current density

Figure 9 clearly demonstrates that an increase in current density leads to a consistent increase in the degree of conversion of sodium sulfate during the electrodialysis process.

4. Conclusions

A series of experiments by the method of planning experiments with solutions of Na_2SO_4, in the presence of magnesium sulfate impurity $MgSO_4$ at concentrations from 2 to 8 g/l was carried out. During the electrodialysis process, the possibility of magnesium precipitation as a hydrated precipitate was identified, along with the simultaneous production of target products – alkali and acid.

A series of experiments was conducted using the experimental design method with sodium sulfate (Na_2SO_4) solutions of varying concentrations. The methodology was refined, and dependencies of the key electrodialysis parameters were obtained under steady-state conditions without solution circulation. This enabled the development of an approach for predicting the process duration required to achieve complete conversion of the initial solution, as well as determining the calculated number of electrodialysis stages needed for operation of the unit in continuous flow mode.

The main performance indicators of the sodium sulfate electrodialysis process, determined based on solution density and controlled according to Faraday's law, are the degree of conversion and the specific energy consumption per unit mass of Na_2SO_4.

Dependences of sodium sulfate conversion degree on initial solution concentration, current density during electrodialysis and process duration are described by polynomials of the second degree.

The scaling up of sodium sulfate solution electrodialysis technology is significantly limited by the high specific energy consumption for salt processing. From this perspective, the use of multi-chamber electrodialyzers is advisable, as they enable an increase in the energy efficiency of the process.

Author contributions

Conceptualization: BSB; Data curation: AAD, GZM; Formal analysis: YBT, AAD, BSB; Funding acquisition: VSM, GZM; Investigation: YBT, GZM; Methodology: BSB, GZM; Project administration: BSB, VSM; Resources: AAD, GZM; Software: BSB; Supervision: VSM, YBT; Validation: YBT, VSM; Visualization: AAD, BSB; Writing – original draft: AAD, BSB; Writing – review & editing: BSB, YBT. All authors have read and agreed to the published version of the manuscript.

Funding

The research was carried out within the framework of grant funding from the Science Committee of the Ministry of Science and Higher Education of the Republic of Kazakhstan for 2023-2025 in the priority area «Rational use of natural resources, including water resources, geology, processing, new materials and technologies, safe products and structures», project No. AP19677216 «Research and development of technologies, equipment for electrodialysis of solutions of tungstate, sodium sulfate with the regeneration of alkalis, acids».

Acknowledgements

The authors express their sincere gratitude to the editor and anonymous reviewers for their constructive comments and valuable suggestions, which have significantly improved the quality of this manuscript.

Conflicts of interests

The authors declare no conflict of interest.

Data availability statement

The original contributions presented in this study are included in the article. Further inquiries can be directed to the corresponding author.

References

[1] Dzhubari, M.K. & Alekseeva, N.V. (2020). Efficiency of electrodialysis in industrial wastewater treatment. *Bulletin of the Technological University, 23*(7), 33-39

[2] Kemerovo, M.A. (2019). Electrodialysis of a binary solution containing sodium and zinc ions using MK-100 M membranes. *Electronic Processing of Materials, 55*(6), 73-78. https://doi.org/10.5281/zenodo.3522283

[3] Vasiunina, N., Dubova, I., Druzhinin, K. & Ghilmanshina, T. (2024). Processing of sludge water from alumina production by electrodialysis. *Ecology and Industry of Russia, 28*(11), 28-32. https://doi.org/10.18412/1816-0395-2024-11-28-32

[4] Krasnova, T.A. (2012). The experience of using electrodialysis for processing wastewater from organic industries. *Sorbtsionnye I Khromatograficheskie Protsessy*, *12*(3), 419-427. https://journals.vsu.ru/sorpchrom/article/view/1797
[5] Melnikov, S.S., Mugtamov, O.A. & Zabolotsky, V.I. (2020). Study of electrodialysis concentration process of inorganic acids and salts for the two-stage conversion of salts into acids utilizing bipolar electrodialysis. *Separation and Purification Technology*, *235*, 116206. https://doi.org/10.1016/j.seppur.2019.116206
[6] Gonova, V. (2023). Experimental investigation of the purification of solutions from nickel ions by electrodialysis. Modern High-Tech Technologies. *Regional Application*, (1), 37-41. https://doi.org/10.60/snt.20237301.0005
[7] Sadyrbaeva, T.J. (2019). Electrodialysis extraction of zinc(II) by liquid membranes based on di-(2-ethylhexyl) phosphoric acid. *Electrochemistry*, *55*(5), 609-618. https://doi.org/10.1134/S0424857019050104
[8] Xiao, L., Wang, W., Zhang, Q. & et al. (1999). Electrode selection of electrolysis with membrane for sodium tungstate solution. *Journal of Central South University of Technology*, *6*(2), 107-110. https://doi.org/10.1007/s11771-999-0009-3
[9] Niftaliev, S.I., Kozaderova, O.A., Kim, K.B. & Velho, F. (2014). The use of electrodialysis to produce acid and alkali from a concentrated solution of sodium sulfate. *Bulletin of the Voronezh State University of Engineering Technologies*, (4), 175-178. https://doi.org/10.20914/2310-1202-2014-4-175-178
[10] Abakumov, M.V., Kolesnikov, A.V., Brodskiy, V.A., & Nyein, Ch.M. (2022). Utilization of salt wastes by electrodialysis with obtaining secondary products. *Theoretical and Applied Ecology*, (4), 96-103. https://doi.org/10.25750/1995-4301-2022-4-096-103
[11] Nowak, M., Jaroszek, H., & Turkowska, M. (2014). Conversion of waste sodium sulfate with bipolar membrane electrodialysis. In Membranes and membrane processes in environmental protection. Monographs of the Environmental Engineering Committee, Polish Academy of Sciences, (119), 337-349.
[12] GOST 195–77. (1977). State standard of the USSR. Reagents. Sodium sulfite. *Moscow: Izdatel'stvo standartov*
[13] Shokhakimova, A.A. (2022). Study of heterogeneous cation-exchange membranes obtained on the basis of inert polymers. *Universum: Technical Sciences*, *1*(94), 12989. https://doi.org/10.32743/UniTech.2022.94.1.12989
[14] Dauletbakova, A., Baimbetov, B., Tazhiyev, Y. & Moldabayeva, G. (2025). Investigation of the electrodialysis of sodium tungstate solutions for the production of tungstic acid. *Applied Sciences*, *15*, 7033. https://doi.org/10.3390/app15137033
[15] Wang, W., Zhang, Y., Yang, X., Sun, H., Wu, Y. & Shao, L. (2023). Monovalent cation exchange membranes with Janus charged structure for ion separation. *Engineering*, *25*, 204-213. https://doi.org/10.1016/j.eng.2021.09.020
[16] Li, X.D., Zhao, X.L., Ye, Y., Wang, B.D. & Xiong, R.H. (2022). Study on the regeneration process of CO2 absorbent based on electrodialysis technology. *Power Generation Technology*, *43*(4), 593-599. https://doi.org/10.12096/j.2096-4528.pgt.22019
[17] Strathmann, H. (2010). Electrodialysis, a mature technology with a multitude of new applications. *Desalination*, *264*(3), 268-288. https://doi.org/10.1016/j.desal.2010.04.069
[18] Malyshev, V.P. (1981). Veroyatnostno-determiniruyushcheye planirovanie eksperimenta [Probabilistic-deterministic planning of experiment]. *Almaty: Nauka*
[19] Spirin, N.A., Lavrov, V.V., Zainullin, L.A., Bondin, A.R. & Burykin, A.A. (2015). Methods of planning and processing engineering experiment results. *Ekaterinburg: Ural Federal University*
[20] Kosenko, E.A. (2023). Planirovaniye eksperimenta: uchebnoye posobiye [Experimental planning: textbook]. *Moscow: MADI*

Сілті және қышқыл регенерациясымен натрий сульфаты ерітінділерінің электродиализінің мембраналық процестерін зерттеу

Б.С. Баимбетов[1], С.В. Мамяченков[2], А.А. Даулетбакова[1*], Г.Ж. Молдабаева[1], Е.Б. Тажиев[1]

[1]*Satbayev University, Алматы, Қазақстан*
[2]*Ресейдің тұңғыш президенті Б.Н. Ельцин атындағы Орал Федералдық университеті, Екатеринбург, Ресей*

**Корреспонденция үшін автор: a.dauletbakova@satbayev.university*

Аңдатпа. Бұл жұмыста әртүрлі өндірістік процестерде түзілетін натрий сульфаты (Na_2SO_4) ерітінділерін электродиализ әдісі арқылы құнды өнімдерге – күкірт қышқылына (H_2SO_4) және натрий гидроксидіне (NaOH) қайта өңдеу мүмкіндігі қарастырылады. Натрий сульфаты ерітінділерін қайта өңдеу мәселесі олардың көп мөлшерде түзілуімен және бейорганикалық қоспалардың жоғары құрамымен өзекті, ал дәстүрлі тазарту әдістері энергияны көп қажет етеді және экономикалық тұрғыдан тиімсіз. Авторлар МК-40, МА-41 және МВ-2И, сондай-ақ Ralex BM мембраналарын қолдана отырып, натрий сульфаты ерітінділерін электродиализ арқылы өндіру мен қайта өңдеудің қолданыстағы әдістеріне талдау жүргізді. Электродиализ жүргізу үшін катион- және анионалмастырғыш МК-40, МА-41 (РФ) және EDC1R, EAC1R (ҚХР) маркалы мембраналары қолданылған 3 камералы және 6 секциялы электродиализатор сұлбалары пайдаланылды. Сондай-ақ EDAM және EDCM маркалы мембраналар қолданылған көп камералы стендтік қондырғының сұлбасы қарастырылды. Үш қондырғыда тәжірибелер жүргізу шарттары В.П. Малышевтің ықтималдық-детерминистік эксперименттерді жоспарлау әдісімен құрастырылды. Бірінші қондырғы үшін келесі тәуелділіктер алынды: Na_2SO_4 концентрациясынан конверсия дәрежесі, катодтық ток тығыздығы мен $MgSO_4$ қоспасының мөлшеріне байланысты процесс ұзақтығы. Бастапқы ерітіндінің концентрациясы мен ток тығыздығына байланысты энергия шығынының үш қондырғы бойынша алынған тәуелділіктері электродиализ процесінің орындылығын бағалауға мүмкіндік береді.

Негізгі сөздер: *натрий сульфаты, электродиализ, мембраналық процестер, натрий гидроксиді, күкірт қышқылы.*

Исследование мембранных процессов электродиализа растворов сульфата натрия с регенерацией щелочи и кислоты

Б.С. Баимбетов[1], С.В. Мамяченков[2], А.А. Даулетбакова[1*], Г.Ж. Молдабаева[1], Е.Б. Тажиев[1]

[1]*Satbayev University, Алматы, Казахстан*
[2]*Уральский федеральный университет имени первого Президента России Б.Н. Ельцина, Екатеринбург, Россия*
**Автор для корреспонденции: a.dauletbakova@satbayev.university*

Аннотация. В данной работе рассматривается возможность переработки растворов сульфата натрия (Na_2SO_4), образующихся в различных промышленных процессах, в ценные продукты – серную кислоту (H_2SO_4) и гидроксид натрия (NaOH) с использованием метода электродиализа. Проблема переработки растворов сульфата натрия актуальна в связи с их значительным объемом и высоким содержанием неорганических примесей, при этом традиционные методы очистки являются энергоемкими и экономически нецелесообразными. Авторами проведен анализ существующих методик получения и переработки растворов сульфата натрия электродиализом с использованием мембран МК-40, МА-41 и МБ-2И и мембран Ralex BM. С целью проведения электродиализа применены схемы 3-х камерного и 6-ти секционного электродиализаторов с использованием катионо-, анионообменных мембран марок МК-40, МА-41 (РФ) и EDC1R, EAC1R (КНР). Рассматривалась схема стендовой установки многокамерного электродиализатора с использованием мембран марки мембран EDAM и EDCM. Составлены условия проведения экспериментов на 3-х установках по методу вероятностно-детерминированного планирования экспериментов Малышева В.П. Получены зависимости для первой установки: степень конверсии от концентрации Na_2SO_4, продолжительности процесса от катодной плотности и содержание примеси $MgSO_4$. Зависимости расхода энергии от концентрации начального раствора и плотности тока на 3-х установках позволяют судить о целесообразности проведения процесса электродиализа.

Ключевые слова: *сульфат натрия, электродиализ, мембранные процессы, гидроксид натрия, серная кислота*.

Publisher's note

All claims expressed in this manuscript are solely those of the authors and do not necessarily represent those of their affiliated organizations, or those of the publisher, the editors and the reviewers.

SATBAYEV UNIVERSITY

Engineering Journal of Satbayev University

Volume 147 (2025), Issue 6, 8-16

https://doi.org/10.51301/ejsu.2025.i6.02

The effect of iron on the production of ferrosilicon and the volatilization of non-ferrous metals from a mixture of sulfide ores from the Shalkiya and Zhayrem deposits

D.K. Aitkulov[1], V.M. Shevko[2*], A.D. Badikova[2], T.I. Adam[2]

[1]*National Center on complex processing of mineral raw materials of the Republic of Kazakhstan, Almaty, Kazakhstan*
[2]*M. Auezov South Kazakhstan University, Shymkent, Kazakhstan*

**Corresponding author: shevkovm@mail.ru*

Abstract. The article presents the results of studies on the complex processing of ores from the Shalkiya and Zhayrem deposits, a distinctive feature of which is not only a low degree of floatability (due to close mutual intergrowth of zinc and lead ore minerals with non-metallic minerals), but also a high content (40-50%) of silica. The studies were carried out by thermodynamic modeling methods using the HSC-6.0 software package based on the principle of minimum Gibbs energy, second-order planning and electric smelting in an arc single-electrode furnace of sulfide ores from the Shalkiya and Zhayrem deposits (with a ratio of 1:1) together with carbon (coke) and iron (steel cuttings). The effect of temperature and the amount of iron on the equilibrium distribution of silicon, zinc, lead, the composition of the silicon-containing alloy and sublimates containing zinc and lead was determined. Conditions for the equilibrium formation of grade ferrosilicon with the transition of 60 to 85% silicon, at least 99% zinc and 48-89% lead into sublimates were determined. Ferrosilicon grade FeSi45 was obtained by electric smelting of a mixture of the Shalkiya and Zhayrem ores in the presence of 26% coke and 18% steel cuttings, and ferrosilicon grade FeSi25 was obtained in the presence of 26% coke and 38% iron. Sublimates of electric smelting contain 25.0-26.1% zinc and 10.5-11.8% lead.

Keywords: *lead-zinc polymetallic ores, ferrosilicon, sublimates, thermodynamic modelling, electrosmelting.*

Received: 28 July 2025
Accepted: 15 December 2025
Available online: 31 December 2025

1. Introduction

The existing approaches to zinc production and extraction, mainly based on traditional pyrometallurgical and hydrometallurgical processing of sulfide ores, face a number of significant difficulties [1-3]. Despite the fact that up to 80% of the world's zinc is obtained from sulfide raw materials according to the classical scheme [4-9], it is characterized by a significant number of stages: crushing, grinding, enrichment, roasting, leaching, solution purification, electrolysis and obtaining cathode zinc. This approach leads to relatively low rates of valuable metal extraction and the formation of a large amount of waste, such as enrichment tailings and leaching cakes. Research in the field of enrichment and hydrometallurgical processing of lead-zinc ores is also not able to completely solve the problem of low zinc and lead extraction into concentrate, and is also associated with the formation of multi-ton waste – enrichment tailings [10-13]. These problems are especially relevant for the Shalkiya and Zhayrem complex polymetallic ore deposits. The reserves of these deposits are significant: Shalkiya contains 129.35 million tons of balance and 119.56 million tons of off-balance ores (3.49-4.27% Zn, 0.8-1.28% Pb) [14-16], and Zhayrem contains 136.7 million tons of barite-polymetallic ore and 62.9 million tons of lead-zinc barite-free ore [17], containing 3.4-5.73% Zn, 0.56-1.5% Pb [18]. A distinctive feature of these ores is the high silica content (49.63-56.0%), which makes them not only a source of non-ferrous metals, but also a potential raw material for the production of silicon-containing ferroalloys, such as ferrosilicon.

In M. Auezov South Kazakhstan University, together with National Center for Complex Processing of Mineral Raw Materials of the Republic of Kazakhstan, a technology for complex processing of complex polymetallic ores of the Shalkiya and Zhayrem deposits is being developed [19-21]. The technology is based on the joint production in one unit – an electric furnace, of several types of products - silicon ferroalloy and non-ferrous metal sublimates. The developed technology significantly increases the efficiency of non-ferrous metal extraction and the complex use of raw materials, significantly reducing. Previously, studies were focused on the processing of ore from the Shalkiya deposit. At the present stage, joint processing of the Shalkiya and Zhayrem ores is becoming relevant, with the organization of their industrial processing in one of the regions of Kazakhstan. Previously, studies were conducted to determine the thermodynamic probability of joint processing of a mixture of the Shalkiya and Zhayrem ores with a carbon and iron content of 22% [22].

aitkulov_dk@mail.ru; shevkovm@mail.ru; sunstroke_91@mail.ru; mstarr@mail.ru
Engineering Journal of Satbayev University. eISSN 2959-2348. Published by Satbayev University

The paper presents the results of studies on the effect of the amount of iron on the formation of ferroalloy and distillation of non-ferrous metals in relation to the joint processing of ores from the Zhayrem and Shalkiya deposits, with a ratio of 1:1.

2. Materials and methods

The studies were carried out by thermodynamic modeling using the HSC Chemistry 6.0 software package, with the Equilibrium Compositions module [23]. To calculate the equilibrium distribution of components (α, %), an algorithm created by employees of Department of Metallurgy of M. Auezov SKU was used [24].

Calculations were carried out in the temperature range of 500-2000°C with an interval of 100°C and a pressure of 1 bar. The amount of carbon was determined based on what was theoretically necessary for the complete reduction of zinc, lead, silicon and iron, and amounted to 26% of the mass of the ore mixture. The amount of iron in the mixture varied from 13 to 47% of the mass of the ore mixture. Composition of the original mixture, mass. %: 49.1 SiO_2, 19.1 CaO, 7.9 Al_2O_3, 3.1 FeS_2, 1.3 PbS, 6.2 ZnS, 3.6 MgO, 0.8 MnO, 5.7 Fe_2O_3, 0.4 Na2O, 3.1 $BaSO_4$.

The determination of the optimal technological parameters for ore processing was carried out using the method of second-order rototable planning (Box-Hunter plan) [25, 26]. The MathCAD program [27] was used to visualize the optimization parameters and create three-dimensional and flat graphic models.

3. Results and discussion

Using the software package, primary information was obtained on the quantitative (kg) distribution of substances in the system of 50 kg Shalkiya ore, 50 kg Zhayrem ore, 26 kg carbon, 30 kg iron, using the algorithm [24] the equilibrium degree of distribution of components in the system was calculated.

From Figure 1 it is evident that the formation of FeSi and Fe_3Si begins at a temperature of 1200ºC, Fe_5Si_3 at 1400ºC, $FeSi_2$ and $FeSi_{2,33}$ at 1500ºC, CaSi at 1800ºC. The highest degree of distribution of silicon in elemental form is observed at 2000ºC and is 16.1%.

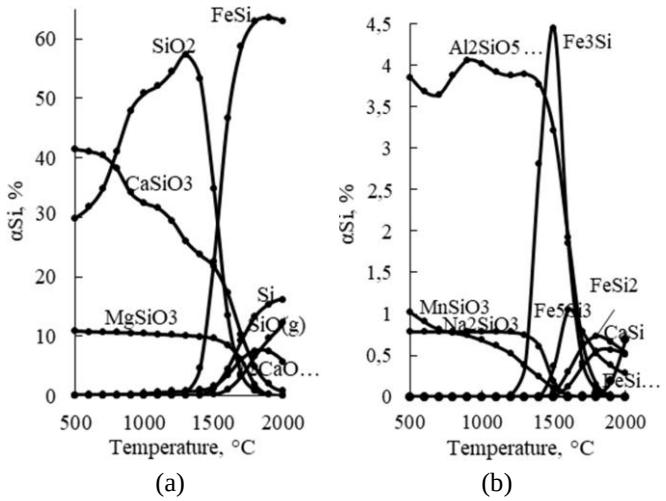

Figure 1. Effect of temperature on the equilibrium distribution of silicon: (a) – formation of ferrosilicon phases and elemental silicon; (b) – transition of silicon into the gas phase in the form of SiO

A further increase in temperature leads to a decrease in the proportion of silicon in elemental form, which is associated with the transition of silicon into gaseous oxide – SiOg (at 2000ºC, the degree of extraction of silicon in SiOg is 12.3%).

Figure 2 shows the effect of temperature on the equilibrium distribution of zinc and lead, from which it is evident that zinc simultaneously begins to be reduced and converted into gas at 1100ºC. At 1700ºC, more than 99% of it passes into the gas phase.

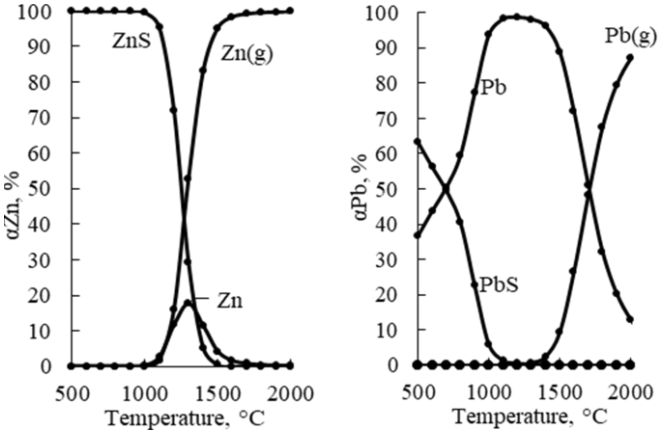

Figure 2. Effect of temperature on the equilibrium degree of distribution of zinc (a) and lead (b)

Lead in the system is almost completely reduced at 1200-1300ºC. Then, with increasing temperature, it passes into gas, reaching a maximum of 87.03% at a temperature of 2000ºC.

Depending on the temperature, the following elements pass into the alloy: Al, Ca, Fe, Mg, Mn, Na, Pb, Si, Zn, and the following elements pass into the gas phase: Al, Ca, Mg, Mn, Na, Pb, Si, Zn. Figure 3 shows the extraction of elements into the alloy and into the gas phase.

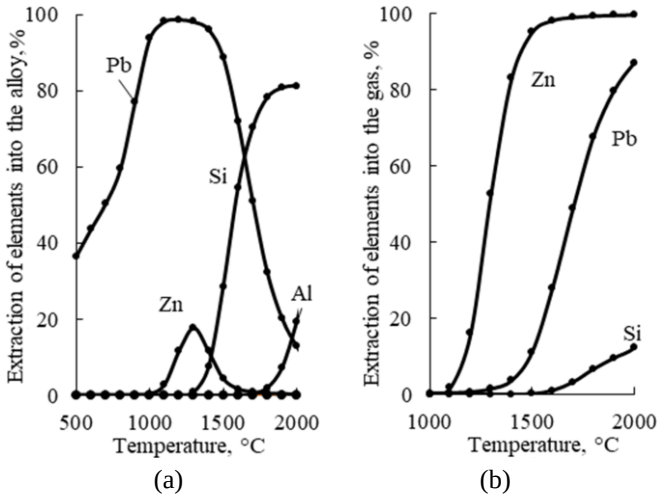

Figure 3. Effect of temperature on the degree of extraction of elements into the alloy (a) and into the gas phase (b)

The highest degree of silicon extraction into the alloy is observed at 2000ºC (81.2%). Aluminum is transferred to the alloy to the maximum (19.3%) at 2000ºC. The degree of silicon extraction ($\Sigma\alpha Si(g) = \alpha Si(g) + \alpha SiO(g)$) into the gas phase is 3.26% at 1700ºC and 12.3 at 2000ºC.

Figure 4 shows information on the content of Si, Pb, Zn, Al in the alloy (excluding iron) and the concentration of Zn, Si, Pb in the gas phase (excluding Ca, Mg, Mn, Na, CO, CO_2, SO_2).

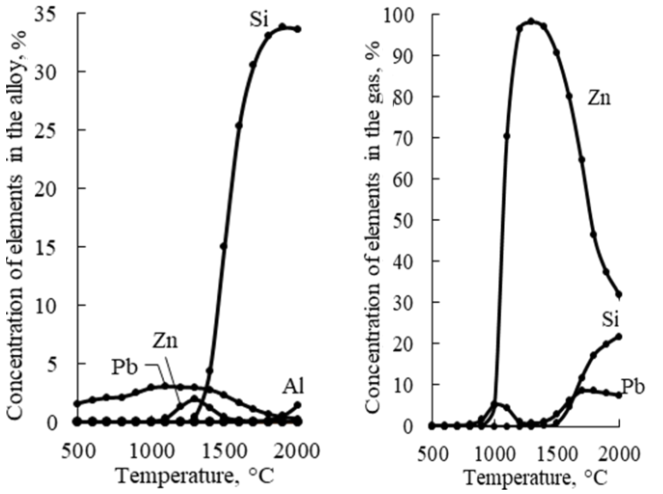

(a) (b)

Figure 4. Effect of temperature on the content of elements in the alloy (a) and gas phase (b)

At 1800ºC the alloy contains 65.18% Fe, 33.06% Si, 0.16% Al, 0.02% Ca, 0.03% Mg, 0.84% Mn, 0.01% Na, 0.67% Pb, 0.04% Zn. The maximum silicon content in the alloy (33.75%) is observed at 1900ºC. The aluminum content in the alloy reaches 1.5% at 2000ºC. The content of elements in the gas phase (excluding CO(g), CO_2(g), COS(g), CS2(g), CS(g), SO2(g)) at 1800ºC is as follows: 46.46% Zn, 8.55% Pb, 17.25% Si, 0.02% Al, 0.05% Ca, 12.75% Mg, 1.78% Mn, 3.3% Na, 9.83% O, 0.01% S. The highest concentration of zinc in the gas phase (98.1%) is observed at 1300ºC, and lead – 8.6% at 1700ºC. Silicon (as the sum of Si(g) and SiO(g)) also passes into the gas phase, its content is maximum at 2000ºC – 21.7%.

Effect of temperature and iron content on the degree of silicon extraction and its concentration in the alloy is shown in Figure 5. As follows from Figure 5, changing the amount of iron significantly affects the technological parameters.

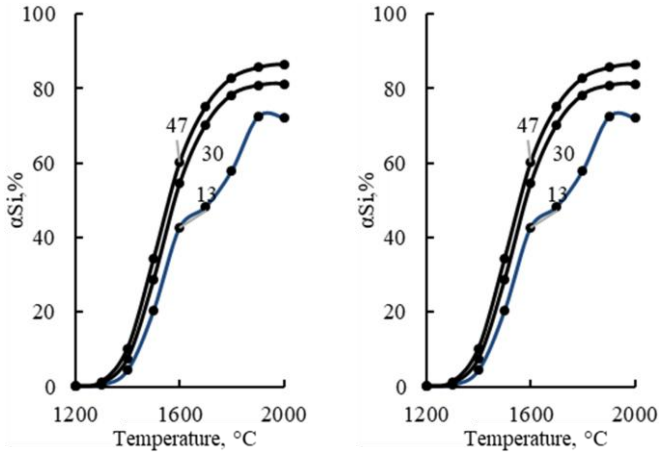

(a) (b)

Figure 5. Effect of temperature and iron on the extraction (a) and concentration (b) of silicon in the alloy. The numbers near the lines are the amount of iron, %

With an increase in the amount of iron in the system, the degree of silicon extraction into the alloy increases, while the concentration, on the contrary, decreases. The maximum degree of silicon extraction (86.5%) is observed at 2000ºC and 47% iron. The highest concentration of silicon in the alloy (45.9%) is observed at 1900ºC and a minimum iron content (13%), while the degree of silicon extraction does not exceed 72.4%.

Changing the amount of iron does not significantly affect the degree of zinc and lead extraction into the gas (Figure 6a). The degree of silicon extraction into the gas phase in the form of Σ (SiO and Si) decreases with increasing iron. For example, at a temperature of 2000ºC and 13% iron, the degree of silicon extraction into the gas is 21.2%, and at 47% iron – 7.3%.

From Figure 6b it is evident that changing the amount of iron has little effect on the lead concentration in the gas. The maximum lead concentration is observed at 1800ºC (7.7-9.5%). Up to 1600ºC, the amount of iron has virtually no effect on the zinc concentration in the gas. Then, up to 2000ºC, with an increase in the amount of iron, the zinc concentration increases. The maximum zinc concentration (98.2%) occurs at 1300ºC regardless of the amount of iron.

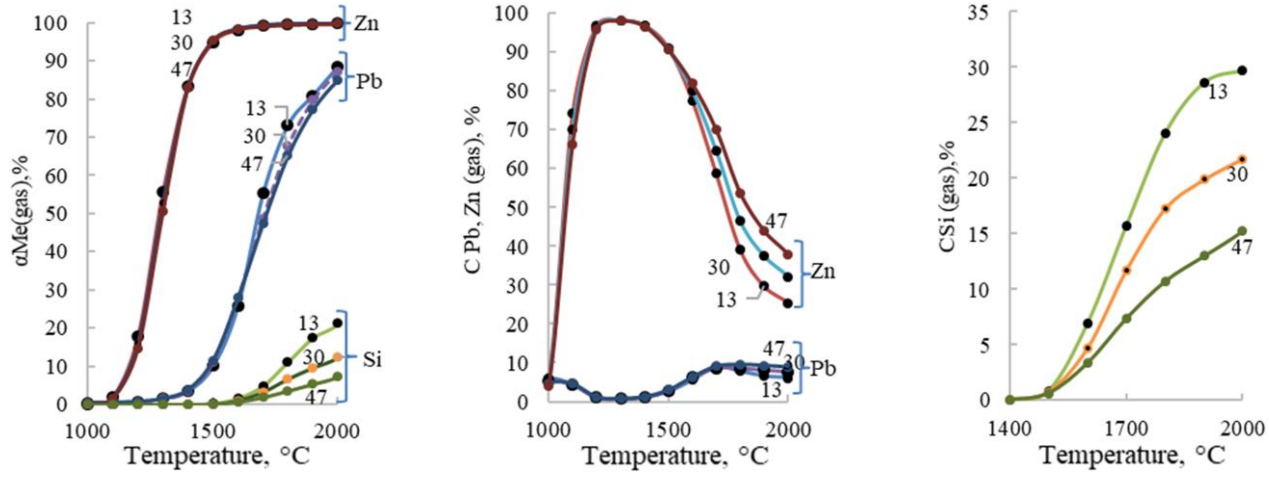

(a) (b) (c)

Figure 6. Effect of temperature and amount of iron on the degree of metal extraction into gas (a), concentration of zinc and lead (b) and silicon (c) in the gas phase. The numbers near the lines are the amount of iron, %

The silicon content in the gas phase (Figure 6c) decreases significantly with increasing iron content. At 1800ºC and 13% iron, the silicon concentration in the gas is 24.04%, and at 47% iron – 10.73%. In order to determine the optimal equilibrium parameters of the effect of iron on the formation of alloy and lead-zinc sublimates from the mixture of the Zhayrem and Shalkiya ores, the studies were conducted using the second-order rototable planning method. The study planning matrix is given in Table 1.

Table 1. Planning matrix and results of studies of the effect of temperature and amount of iron on technological indicators

No.	Variables				$\alpha Si_{(alloy)}$, %	$CSi_{(alloy)}$, %	$\alpha Zn_{(gas)}$, %	$CZn_{(gas)}$, %	$\alpha Pb_{(gas)}$, %	$CPb_{(gas)}$, %	$\alpha Si_{(gas)}$, %	$CSi_{(gas)}$, %
	Coded view		Natural view									
	X_1	X_2	T, °C	Fe, %								
1	-1	-1	1743.6	17.9	67.00	38.50	99.42	50.00	58.60	7.90	7.50	20.00
2	+1	-1	1956.4	17.9	75.50	41.00	99.78	29.30	85.20	6.33	16.80	27.00
3	-1	+1	1743.6	42.1	78.30	27.00	99.34	61.50	56.40	9.20	3.00	10.00
4	+1	+1	1956.4	42.1	85.38	27.00	99.73	39.00	82.80	8.80	7.20	15.80
5	1.414	0	2000	30	81.18	33.56	99.80	32.01	87.10	7.50	12.30	21.76
6	-1.414	0	1700	30	70.22	30.57	99.17	64.57	48.82	8.60	3.26	11.69
7	0	1.414	1850	47	84.26	26.59	99.58	48.82	71.25	9.38	4.47	11.87
8	0	-1.414	1850	12	65.20	43.35	99.69	34.39	77.08	7.10	14.26	26.32
9	0	0	1850	30	79.54	33.40	99.63	41.96	73.72	8.33	8.15	18.57
10	0	0	1850	30	78.80	33.50	99.63	41.80	72.80	8.42	8.10	18.40
11	0	0	1850	30	80.40	33.30	99.65	42.20	73.83	8.30	8.22	18.60
12	0	0	1850	30	79.10	33.20	99.64	41.70	73.75	8.26	8.25	18.30
13	0	0	1850	30	80.00	33.80	99.62	42.30	73.85	8.38	8.13	18.70

Based on the results of the research according to the plans presented in Table 1, the regression equations were obtained:

$$\alpha Si_{(alloy)} = -515.189 + 0.569 \cdot T + 1.863 \cdot Fe - 1.415 \cdot 10^{-4} \cdot T^2 - 1.43 \cdot 10^{-2} \cdot Fe^2 - 2.757 \cdot 10^{-4} \cdot T \cdot Fe \quad (1)$$

$$CSi_{(alloy)} = -206.971 + 0.259 \cdot T + 0.091 \cdot Fe - 6.386 \cdot T^2 + 4.979 \cdot 10^{-3} \cdot Fe^2 - 4.855 \cdot 10^{-4} \cdot T \cdot Fe \quad (2)$$

$$\alpha Zn_{(gas)} = 74.723 + 0.025 \cdot T - 0.016 \cdot Fe - 6.369 \cdot 10^{-6} \cdot T^2 + 2.049 \cdot Fe^2 + 6.214 \cdot 10^{-6} \cdot T \cdot Fe \quad (3)$$

$$CZn_{(gas)} = 1154.65 - 1.124 \cdot T + 1.156 \cdot Fe + 2.78 \cdot 10^{-4} \cdot T^2 - 1.318 \cdot 10^{-3} \cdot Fe^2 - 3.495 \cdot 10^{-4} \cdot T \cdot Fe \quad (4)$$

$$\alpha Pb_{(gas)} = -1030.71 + 1.073 \cdot T - 0.147 \cdot Fe - 2.555 \cdot 10^{-4} \cdot T^2 + 1.427 \cdot 10^{-3} \cdot Fe^2 - 3.884 \cdot 10^{-5} \cdot T \cdot Fe \quad (5)$$

$$CPb_{(gas)} = -24.16 + 0.043 \cdot T - 0.318 \cdot Fe - 1.465 \cdot T^2 - 4.849 \cdot 10^{-4} \cdot Fe^2 + 2.268 \cdot 10^{-4} \cdot T \cdot Fe \quad (6)$$

$$\alpha Si_{(gas)} = -146.464 + 0.12 \cdot T + 1.293 \cdot Fe - 1.606 \cdot 10^{-4} \cdot T^2 + 4.173 \cdot 10^{-3} \cdot Fe^2 - 9.903 \cdot 10^{-4} \cdot T \cdot Fe \quad (7)$$

$$CSi_{(gas)} = -286.557 + 0.307 \cdot T - 0.148 \cdot Fe - 7.261 \cdot 10^{-5} \cdot T^2 + 2.479 \cdot 10^{-3} \cdot Fe^2 - 2.33 \cdot 10^{-4} \cdot T \cdot Fe \quad (8)$$

Using which 3D models and their horizontal response surfaces were constructed (Figures 7-10).

From Figure 7 it follows that the highest degree of silicon extraction into the alloy – 85.69% is observed at a temperature of 1960ºC and 47% iron, and the maximum concentration is 44.5% at 1960ºC and 13% iron.

From Figures 8-10 it is evident that at 13% iron and a temperature of 2000ºC the maximum degree of zinc extraction is 99.82%, lead – 89.49% and silicon – 21.08% into the gas phase, as well as the highest silicon content in the gas phase – 30.27%. The highest concentration of zinc (71.8%) and lead (9.36%) in the gas phase is observed at 47% iron and a temperature of 1700ºC and 1775ºC, respectively.

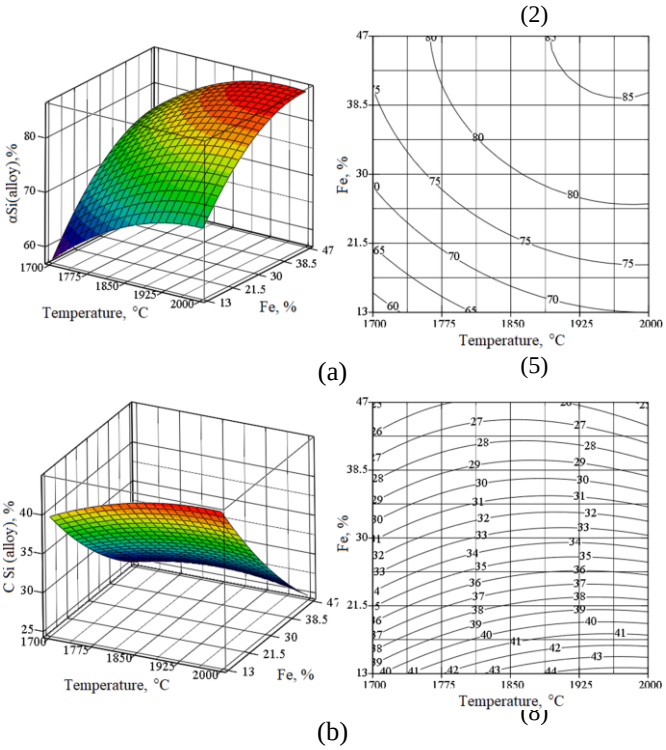

Figure 7. 3D models and planar projections illustrating the effect of temperature and iron content on silicon behavior: (a) – degree of silicon extraction into the alloy; (b) – silicon concentration in the alloy

The basis for determining the optimal equilibrium technological parameters was the silicon concentration in the alloy corresponding to its grade.

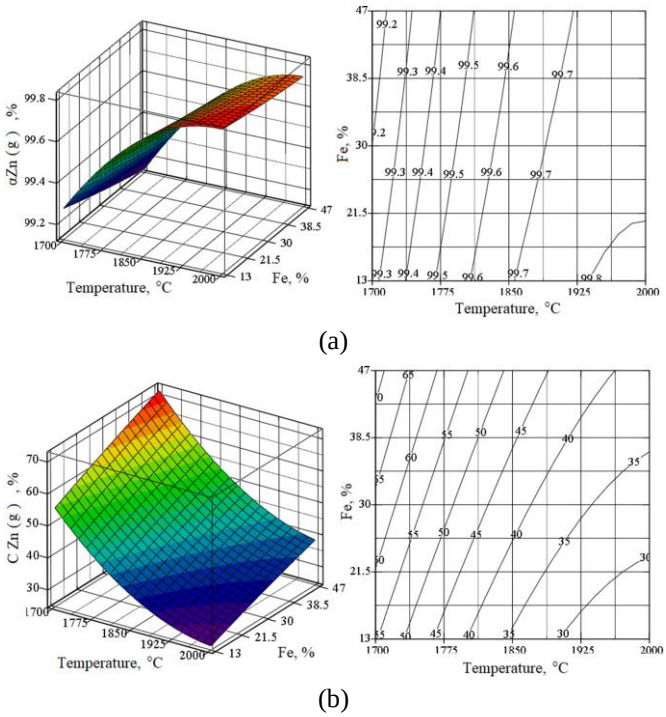

Figure 8. 3D models and planar projections illustrating the effect of temperature and iron content on zinc behavior: (a) – degree of zinc extraction into the alloy; (b) – zinc concentration in the gas phase

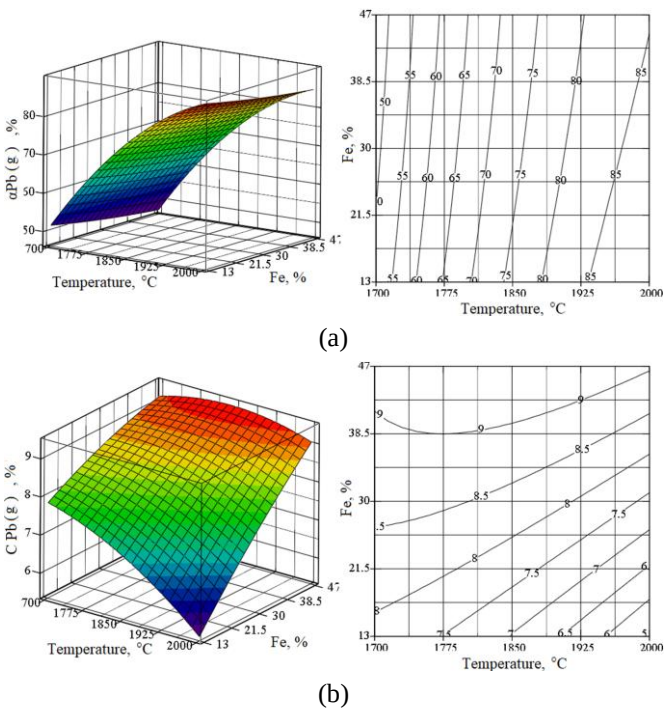

Figure 9. 3D models and planar projections illustrating the effect of temperature and iron content on lead behavior: (a) – degree of lead extraction into the alloy; (b) – lead concentration in the gas phase

Geometric optimization was performed by superimposing the dependencies αSi(alloy) = f(T, Fe) and CSi(alloy) = f(T, Fe) on one horizontal plane with the determination of αZn(gas), αPb(gas) and αSi(gas) at the points of the boundary regions (Figure 11 and Table 2). Table 2 shows the technological indicators at the points of Figure 11.

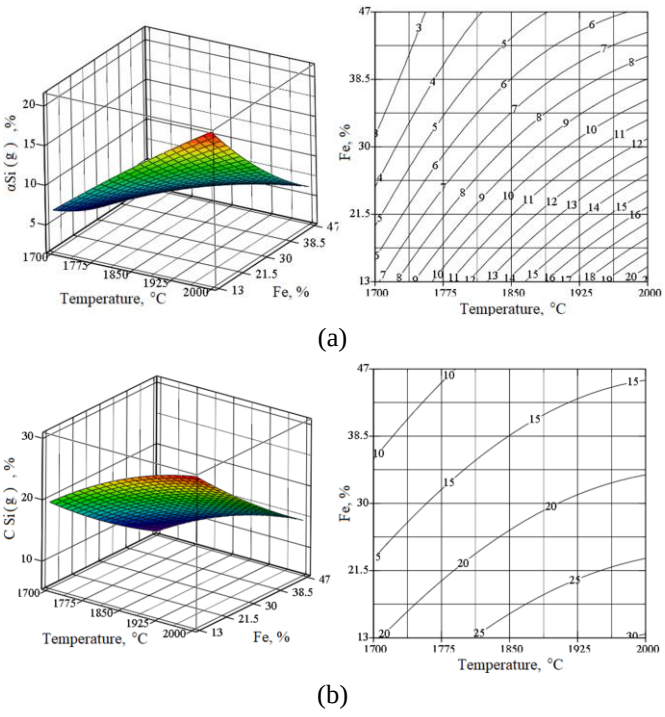

Figure 10. 3D models and planar projections illustrating the effect of temperature and iron content on silicon behavior in the gas phase: (a) – degree of silicon extraction; (b) – silicon concentration in the gas phase

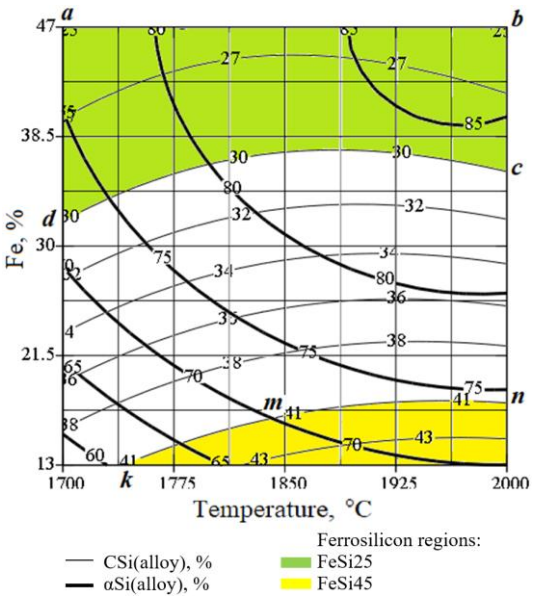

Figure 11. Combined picture of the effect of temperature and amount of iron on technological parameters

It is evident from Figure 11 that ferrosilicon grade FeSi25with the extraction degree of 75.9-85.5% silicon is formed in the temperature range of 1700-2000ºC and 35.87-47% iron. At the same time, 99.1-99.2% zinc, 47.2-86.0% lead, and 2.0-10.0% silicon pass into the gas phase containing 34.7-71.8% Zn, 8.0-9.1% Pb, and 6.1-11.4% Si.

In the temperature range of 1741-2000ºC at 13-17.83% iron, ferrosilicon grade FeSi45 is formed, into which silicon passes by 60.8-74.2%. The content of metals in the gas phase: zinc – 25.7-48.4%, lead – 5.4-7.7%, silicon – 21.8-30.3%. In this case, 99.4-99.8% Zn, 59.4-89.5% Pb, 21.8-30.3% Si pass into the gas phase.

Table 2. Values of technological parameters at the points of Figure 11

Points of Figure	T, °C	Fe, %	$\alpha Si_{(alloy)}$, %	$CSi_{(alloy)}$, %	$\alpha Zn_{(gas)}$, %	$CZn_{(gas)}$, %	$\alpha Pb_{(gas)}$ %	$CPb_{(gas)}$, %	$\alpha Si_{(gas)}$, %	$CSi_{(gas)}$, %	Alloy grade
a	1700	47	75.9	24.9	99.1	71.8	47.2	9.1	2.0	6.1	FeSi25
b	2000	47	85.5	24.7	99.8	38.6	84.8	9.1	6.2	14.5	
c	2000	35.87	84.0	29.9	99.8	34.7	86.0	8.0	10.0	19.0	
d	1700	31.9	71.9	30.0	99.2	64.9	48.7	8.7	2.9	11.4	
k	1741	13	60.8	41.0	99.4	48.4	59.4	7.7	8.9	21.8	FeSi45
m	1845	16.6	70.1	41.1	99.7	36.5	75.0	7.3	12.6	24.5	
n	2000	17.83	74.2	41.0	99.8	27.7	88.6	6.0	18.4	27.7	
l	2000	13	70.0	44.5	99.8	25.7	89.5	5.4	21.1	30.3	

Photographs of ferroalloys obtained by electric smelting of batches No. 1 and No. 2 are shown in Figure 12. SEM analysis of the alloy of batch No. 2 is shown in Figure 13.

(a) (b)

Figure 12. Photographs of the obtained ferroalloys. (a) – batch No. 1, (b) – batch No. 2

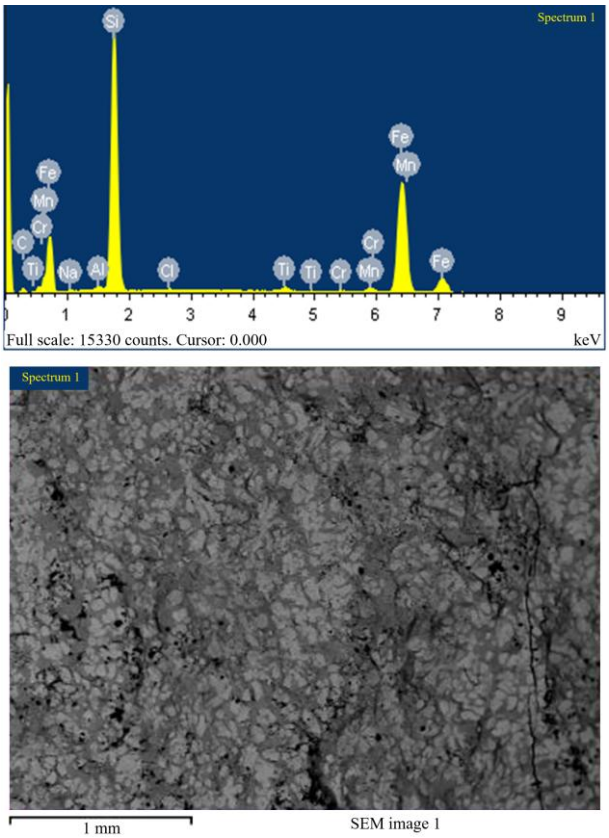

Figure 13. SEM microstructure and EDS spectrum of the alloy obtained from batch No. 2. Elemental composition (wt.%): 8.59 C, 0.46 Na, 0.40 Al, 33.45 Si, 0.26 Cl, 0.91 Ti, 0.30 Cr, 1.47 Mn, and 54.17 Fe.

Experimental exploratory electric smelting of the mixture of the Shalkiya and Zhayrem ores with different amounts of iron was carried out. (A detailed description of the electric smelting technique is presented in [28, 29]). The electric smelting of batch (No. 1) containing the mixture of the Shalkiya and Zhayrem ores, 26% coke, and 16.4% iron yielded ferrosilicon with a silicon content of 36.0-41.5%, which corresponds to ferrosilicon grade FeSi45 [30].

The resulting sublimates contain 27.0-29.1% zinc and 12.5-14.2% lead. The electric smelting of batch (No. 2) containing the mixture of the Shalkiya and Zhayrem ores, 26% coke, and 38% iron yielded ferrosilicon with a silicon content of 28.8-37.2%, which corresponds to ferrosilicon grade FeSi25. The process resulted in the formation of sublimates containing 25.0-26.1% zinc and 10.5-11.8% lead (the analysis of the sublimates was carried out by titrimetric method in Central Analytical Laboratory of A-Mega Trading LLP).

4. Conclusions

Based on the obtained results on the effect of the amount of iron on the formation of ferroalloy and distillation of non-ferrous metals during the processing of the mixture of ores from the Zhayrem and Shalkiya deposits, in a ratio of 1:1, it was established that:

Under equilibrium conditions:

- the interaction products in the system are: $CO_{(g)}$, FeSi, $CaSiO_3$, $FeSiO_3$, $*2CaO*SiO_2$, $SiO_{(g)}$, CaS, $MgSiO_3$, $CaO*Al_2O_3$, Fe_3Si, ZnS, $Ca_{(g)}$, Al_2O_3, Al_2SiO_5(A), $Zn_{(g)}$, FeO, Si, $*3CaO*Al_2O_3$, $Mg_{(g)}$, BaO, Al, MgO, CaO, $Al_{(g)}$, Pb, $MnSiO_3$, $Pb_{(g)}$, Fe_5Si_3, PbS, Na_2SiO_3, Zn, CaSi, Mn, $Mn_{(g)}$, MnO, $FeSi_2$, $CO_{2(g)}$, $Na_{(g)}$, $FeSi_{2.33}$, $*2CaO*Al_2O_3$, $COS_{(g)}$, $Si_{(g)}$, $FeSi_{2.43}$.

– with an increase in the amount of iron in the system, the degree of silicon extraction into the alloy increases, while the concentration, on the contrary, decreases;

– ferrosilicon grade FeSi25, which contains 24.7-30% Si, is formed in the range of 1700-2000ºC in the presence of 35.87-47% iron. The degree of silicon extraction into the alloy is 75.9-85.5%. 34.7-71.8% zinc, 8.0-9.1 lead and 6.1-11.4% silicon pass into sublimates;

– ferrosilicon grade FeSi45 is formed in the range of 1741-2000ºC with the iron content of 13-17.83%. The degree of silicon extraction into the alloy is 60.8-74.2%. The sublimes contain 25.7-48.4% zinc, 5.4-77% lead and 21.8-30.3% silicon.

Ferrosilicon grade FeSi45 was obtained by electric smelting of the mixture of the Shalkiya and Zhayrem ores in the presence of 26% coke and 18% steel cuttings, and ferrosilicon grade FeSi25 was obtained in the presence of 26% coke and 38% iron. The sublimes formed in this case contain 25.0-26.1% zinc and 10.5-11.8% lead.

Author contributions

Conceptualization: DKA, VMS; Data curation: DKA, VMS; Formal analysis: VMS; Funding acquisition: DKA; Investigation: VMS, ADB, TIA; Methodology: VMS; Project administration: ADB; Resources: DKA, VMS; Software: VMS; Supervision: DKA, VMS; Validation: ADB, TIA; Visualization: ADB, TIA; Writing – original draft: VMS, ADB, TIA; Writing – review & editing: DKA. All authors have read and agreed to the published version of the manuscript.

Funding

This research was funded by Industry Committee of the Ministry of Industry and Construction of the Republic of Kazakhstan, grant number BR19777171.

Acknowledgements

The authors express their sincere gratitude to the editor and anonymous reviewers for their constructive comments and valuable suggestions, which have significantly improved the quality of this manuscript.

Conflicts of interests

The authors declare no conflict of interest.

Data availability statement

The original contributions presented in this study are included in the article. Further inquiries can be directed to the corresponding author.

References

[1] Haghighi, Hossein & Irannajad, Mehdi. (2025). A New Solvent Extraction Process for Zinc Cathode and Manganese Salt Production from ZnS Concentrates. *JOM*, *77*, 2419-2433. https://doi.org/10.1007/s11837-024-07055-7

[2] Hara, Y.R.S., Tembo, D., Hara, R., Hara, R., Old, A.O.N., Parirenyatwa, S. (2024). Production of Zinc Oxide from Willemite Containing Ore from Kabwe Town in Zambia. In: Peng, Z., et al. Characterization of Minerals, Metals, and Materials. The Minerals, Metals & Materials Series. *Springer, Cham.* https://doi.org/10.1007/978-3-031-50304-7_14

[3] Mudd, G.M., Jowitt, S.M. & Werner, T.T. (2017). The world's lead-zinc mineral resources: Scarcity, data, issues and opportunities. *Ore Geology Reviews*, *80*, 1160-1190. https://doi.org/10.1016/j.oregeorev.2016.08.010

[4] Yakubov, M., Kholikulov, D., Maksudhodjaeva, M. & Yoqubov, O. (2024). Improvement of the technological scheme for processing zinc concentrates by hydrometallurgical method at JSC Almalyk MMC. *Kompleksnoe Ispolzovanie Mineralnogo Syra = Complex Use of Mineral Resources*, *333*(2), 89-96. https://doi.org/10.31643/2025/6445.21

[5] Kositskaya, T.Y., Lapin, A.Y., Varganov, M.S. & Fatkhutdinova O.A. (2024). Studies on the autoclave oxidation leaching technology for a zinc concentrate. *Tsvetnye Metally*, *7*, 37-44. https://doi.org/10.17580/tsm.2024.07.05

[6] Chepushtanova, T.A., Merkibayev, Y.S., Mamyrbayeva, K.K., Sarsenbekov, T. & Mishra, B. (2025). Mechanism and technological results of sulfidation roasting of oxidized lead compounds. *Kompleksnoe Ispolzovanie Mineralnogo Syra= Complex Use of Mineral Resources*, *332*(1), 119-132. https://doi.org/10.31643/2025/6445.11

[7] Chepushtanova, T.A., Merkibayev, Y.S., Baigenzhenov, O.S. & Mishra, B. (2023). Technology of high-temperature sulfidizing roasting of oxidized lead-zinc ore in a fluidized bed furnace. *Non-ferrous Metals*, *54*(1), 3-10. https://doi.org/10.17580/nfm.2023.01.01

[8] Janbatyrov, A.A. (2010). Analysis of Existing Technologies For Processing Polymetallic Ores Of The Zhairem-Atasuysky Ore District. *Bulletin of D. Serikbayev East Kazakhstan State Technical University*, *1*, 14-21.

[9] Semushkina, L., Dulatbek, T., Tusupbaev, N., Nuraly, B. & Mukhanova, A. (2015). The Shalkiya deposit finely disseminated lead-zinc ore processing technology improvement. *Ore Beneficiation*, *2*, 8-14. https://doi.org/10.17580/or.2015.02.02

[10] Haris, R., & Murtaza, H. (2024). A Review on Sustainable Utilisation of Zinc Mine Tailing in Concrete Production. *E3S Web of Conferences*, *596*, 01029. https://doi.org/10.1051/e3sconf/202459601029

[11] Messai, A., Berrekbia, L., Meramria, I., Menéndez-Aguado, J.M., Fernández-Pérez, B., Nikolić, V., Trumić, M., & Boustila, A. (2025). Potential of using zinc processing tailings (ZPTs) in the production of burnt clay bricks. *Proceedings of XVI International Mineral Processing and Recycling Conference*, 171-178. https://doi.org/10.5937/IMPRC25171A

[12] Raimbekova, A., Kapralova, V., Popova, A., Kubekova, S., Dalbanbay, A., Kalenova, A., Mustahimov, B., Yermekbayeva, S. & Myrzabekova, S. (2024). Corrosion behavior of mild steel in sodium sulfate solution in presence of phosphates of different composition. *Journal of Chemical Technology and Metallurgy*, *59*(2), 367-377. https://doi.org/10.59957/jctm.v59.i2.2024.16

[13] Chepushtanova, T.A., Merkibayev, Y.S., Mishra, B. & Kuldeyev Y.I. (2022). Processing of the zinc-lead-bearing flotation middlings by sulfidizing roasting with pyrrhotites production by predicted properties. *Non-ferrous Metals*, *2*, 15-24. https://doi.org/10.17580/nfm.2022.02.03

[14] Vorobkalo, N.R., Baisanov, A.S., Isagulova, D.A., Ibrahimova, Zh.A. & Sharieva, S.S. (2025). Thermodynamic assessment of the possibility of obtaining ferrosilicon from the ore of the Shalkiya deposit. *Bulletin of Aktobe Regional University*, *80*(2), 295-304. https://doi.org/10.70239/arsu.2025.t80.n2.35

[15] Shevko, V., Makhambetova, B., Aitkulov, D. & Badikova, A. (2024). Optimization of joint electric smelting of the Shalkiya sulfide ore and its beneficiation tailings with medium-silicon ferrosilicon production. *Kompleksnoe Ispolzovanie Mineralnogo Syra = Complex Use of Mineral Resources*, *3*(334), 91-98. https://doi.org/10.31643/2025/6445.31

[16] Yushina, T., Yergeshev, A., Dumov, A. & Makavetskas, A. (2022). Study of the material composition of lead-zinc ore of the Shalkiya deposit in order to determine the possibility of its processing. *Non-ferrous Metals*, *53*, 8-14. https://doi.org/10.17580/nfm.2022.02.02

[17] Janbatyrov, A.A. (2010). Analysis of existing reserves of polymetallic raw materials in the Zhairem-Atasui ore region. *Bulletin of D. Serikbayev East Kazakhstan State Technical University*, *1*, 4-13.

[18] Brusnitsyn, A.I., Perova, E.N., Vereshchagin, O.S., Britvin, S.N., Letnikova, E.F., Shkolnik, S.I. & Ivanov, A.V. (2018). Barite-lead-zinc and iron-manganese deposits of the Zhairem ore district: a geological field trip to central Kazakhstan. *Mineralogy*, *3*, 82-92.

[19] Shevko, V., Makhanbetova, B., Aitkulov, D., & Badikova, A. (2024). Smelting a Zn – Pb Sulfide Ore with Magnetite and Carbon for the Production of a Silicon Alloy and Extraction of Zinc and Lead into Sublimates. *Periodica Polytechnica Chemical Engineering*, *68*(1), 124–132. https://doi.org/10.3311/PPch.22114

[20] Shevko, V., Makhanbetova, B., Aitkulov, D., Badikova, A., & Amanov, D. (2024). Thermodynamic and Experimental Substantiation of Comprehensive Processing of Zinc Sulfide Ore and Its Concentration Tailings to Extract Non-Ferrous Metals and Produce a Silicon Ferroalloy. *Minerals*, *14*(8), 819. https://doi.org/10.3390/min14080819

[21] Beisembaev, B.B., Kenzhaliev, B.K., Gorkun, V.I., Govyadovskaya, O.Yu. & Ignatiev, M.M. (2002). Deep processing of lead-zinc ores and industrial products with improved marketability of increased marketability. *Almaty: Gylym.* https://doi.org/10.31643/2002-2019.006

[22] Makhanbetova, B.A., Shevko, V.M. & Lavrov, B.A. (2024) Forecasting of ferroalloy production and extraction of zinc and lead from a mixture of sulfide ores of the Zhairem and Shalkiya

deposits by thermodynamic modeling. *In Proceedings «Auezov Readings - 22: Academician Kanysh Satpayev - the founder of Kazakhstani science»*, *6*, 198-204.
[23] Roine, A. (2021). HSC Chemistry®, [Software] Metso: Outotec, Pori. *Retrieved from*: www.mogroup.com/hsc
[24] Shevko, V.M., Serzhanov, G.M., Karataeva, G.E. & Amanov, D.D. (2019). Calculation equilibrium distribution elements in relation to TO software complex HSC-5.1. Certificate for the object protected by copyright of the Republic of Kazakhstan, No. 1501. *Espoo, Finland: Mesto Finland Oy*
[25] Akhnazarova, S.A. & Kafarov, B.V. (1978). Methods for Optimizing Experiments in the Chemical Industry. Higher School Moscow. *Moscow, Russia*
[26] Inkov, A.M., Tapalov, T., Umbetov, U.U., Hu Wen Tsen, V., Akhmetova, K.T., & Dyakova, E.T. (2003). Optimization Methods. *South Kazakhstan State University, Shymkent, Kazakhstan*
[27] Ochkov, V.F. (2007). Mathcad 14 for Students, Engineers and Designers. BHV-Petersburg. *Saint Petersburg, Russia*
[28] Makhanbetova, B., Shevko, V., Aitkulov, D., Lavrov, B., & Badikova, A. (2024). Optimization of pyroprocessing of zinc sulfide ore to produce ferroalloy and zinc. *E3S Web of Conferences*, *531*, 01025. https://doi.org/10.1051/e3sconf/202453101025
[29] Uteyeva, R., Shevko, V., Aitkulov, D., Badikova, A., & Tleuova, S. (2023). Electric smelting of phosphorites with production of a ferroalloy, calcium carbide and sublimation of phosphorus. *Engineering Journal of Satbayev University*, *145*, 11-17. https://doi.org/10.51301/ejsu.2023.i6.02
[30] State Standard 1415-93. (2011). Ferrosilicon. Technical Requirements and Delivery Conditions. *Moscow, Russia: Standartinform*

Шалхия және Жәйрем сульфидті кендерінің қоспасынан түсті металдарды айдау және кремнийлі ферроқорытпаны алуда темірдің әсері

Д.К. Айткулов[1], В.М. Шевко[2*], А.Д. Бадикова[2], Т.И. Адам[2]

[1]*Қазақстан Республикасының минералдық шикізатты кешенді өңдеу жөніндегі ұлттық орталығы, Алматы, Қазақстан*
[2]*М.Әуезов атындағы Оңтүстік Қазақстан университеті, Шымкент, Қазақстан*

**Корреспонденция үшін автор: shevkovm@mail.ru*

Аңдатпа. Мақалада Шалқия және Жәйрем кен орындарының кендерін кешенді өңдеу бойынша зерттеулердің нәтижелері келтірілген, ондағы флотациялаудың төмен дәрежесінде ғана емес (мырыш пен қорғасын кенінің минералдарының металл емес минералдармен өзара тығыз өсуіне байланысты), сонымен қатар кремнеземнің жоғары мөлшерілігімен (40-50%) айрықша ерекшеленеді.Зерттеулер Шалқия және Жәйрем кен орындарындағы сульфидті кендерді (1:1 қатынасымен) көміртегімен (кокспен) және темірмен (темір жоңқасымен) бір электродты доғалы пеште электрлі балқытумен, екінші ретті жоспарлаумен және Гиббс энергиясының минималды принципіне негізделген HSC-6.0 бағдарламалық кешенін қолдану арқылы термодинамикалық модельдеу әдістерімен жүргізілді. Температура мен темір мөлшерінің кремнийқұрамдас қорытпаның, мырыш пен қорғасыны бар айдаулардың құрамын және кремнийдің, мырыштың, қорғасынның біртекті таралуына әсері анықталды. Құрамында 60-тан 85% кремнийге, кемінде 99% мырыш және 48-89% қорғасын айдауларына өтетін сортты ферросилиций түзілудің тепе-теңдік шарттары анықталды. Шалқия және Жәйрем кендерін электрлібалқытуда қоспа құрамы 26% кокс және 18% болат жоңқасының қатысуымен FeSi45 маркалы ферросилиций, ал 26% кокс және 38% темір жоңқасының қатысуында FeSi25 ферросилиций алынды. Электрлібалқыту айдаулары 25.0-26.1% мырыш пен 10.5-11.8% қорғасыннан тұрады.

Негізгі сөздер: *мырыш пен қорғасын полиметалл кендері, ферросилиций, айдаулар, термодинамикалық модельдеу, электробалқыту.*

Влияние железа на получение кремнистого ферросплава и отгонку цветных металлов из смеси сульфидных руд Шалкия и Жайрем

Д.К. Айткулов[1], В.М. Шевко[2*], А.Д. Бадикова[2], Т.И. Адам[2]

[1]*Национальный центр по комплексной переработки минерального сырья Республики Казахстан, Алматы, Казахстан*
[2]*Южно-Казахстанский университет им. М. Ауэзова, Шымкент, Казахстан*

**Автор для корреспонденции: shevkovm@mail.ru*

Аннотация. В статье приводятся результаты исследований по комплексной переработке руд месторождений Шалкия и Жайрем, отличительной особенностью которых является не только не высокая степень флотируемости (из -за тесного взаимного прорастания рудных минералов цинка и свинца с нерудными минералами), но и высокое содержание в них (40-50%) кремнезема. Исследования проведены методами термодинамического моделирования с использованием программного комплекса HSC-6.0, основанного на принципе минимума энергии Гиббса, планированием второго порядка и электроплавкой в дуговой одноэлектродной печи сульфидных руд месторождений Шалкия и Жайрем

(с отношением 1:1) совместно с углеродом (коксом) и железом (стальной стружкой). Определено влияние температуры и количества железа на равновесное распределение кремния, цинка, свинца состав кремнийсодержащего сплава и возгонов, содержащих цинк и свинец. Определены условия равновесного образования марочного ферросилиция с переходом в них от 60 до 85% кремния, не менее 99% цинка и 48-89% свинца в возгоны. Электроплавкой смеси руд Шалкия и Жайрем в присутствии 26% кокса и 18% стальной стружки получен ферросилиций марки FeSi45, а в присутствии 26% кокса и 38% железа -ферросилиций FeSi25. Возгоны электроплавки содержат 25.0-26.1% цинка и 10.5-11.8% свинца.

Ключевые слова: *свинцово-цинковые полиметаллические руды, ферросилиций, возгоны, термодинамическое моделирование, электроплавка*.

Publisher's note

SATBAYEV UNIVERSITY

Engineering Journal of Satbayev University

Volume 147 (2025), Issue 6, 17-23

https://doi.org/10.51301/ejsu.2025.i6.03

Obtaining manganese pellets from manganese-containing technogenic waste

S.S. Temirova, G.Zh. Abdykirova, A.A. Biryukova, D.Y. Fischer*

Institute of Metallurgy and Ore Beneficiation, Almaty, Kazakhstan

**Corresponding author: fischerdametken@gmail.com*

Abstract. Recycling manganese-rich industrial residues is a significant technological and environmental challenge in mining regions because it lowers long-term waste accumulation and provides a valuable supplementary feedstock for ferroalloy production. This study thoroughly examined fine-grained manganese sludge from the Ushkatyn-3 deposit (JSC «Zhayremsky GOK») using particle size analysis, X-ray fluorescence spectroscopy, X-ray diffraction, ICP-AES, and differential thermal analysis. Nearly all of the original technogenic material, which contained 15.0-18.3% Mn, was composed of barite, quartz, bixbyite, calcite, and braunite. Based on the identified granulometric and mineralogical properties, a gravity-magnetic beneficiation flowsheet was created. Sequential treatment using jigging, concentration tables, and high-intensity magnetic separation produced a finely dispersed manganese concentrate with a Mn content of 34.9-35.2% and a recovery of roughly 61%. Pelletizing mixtures containing calcium oxide, natural iron-bearing diatomite, and, in certain compositions, coke was made using the resultant concentrate. The formation of green pellets during granulation in an Eirich mixer-granulator has been examined in relation to binder content and particle-size distribution. The thermal behavior of the composite mixture was examined using TGA-DTA/DSC and quadrupole mass spectrometry, which revealed dehydration, carbonate breakdown, and polymorphic transformations of manganese phases over the temperature range of 200-1160°C. Because it offers adequate phase consolidation without partial melting, the sintering process proved that 1170°C is the optimal firing temperature. The formation of ferrobustamite ($CaFe_2Si_2O_4$), hausmannite (Mn_3O_4), and jacobsite ($MnFe_2O_4$) was verified by X-ray diffraction analysis of the fired pellets. This is the ferrosilicon calcium binding phase, which strengthens the agglomerates' structural integrity. The sintered pellets' high mechanical strength (up to 33.8 kg per pellet), apparent density of 1.45-1.91 g/cm³, and open porosity of 27-35% attest to their suitability as feedstock for ferromanganese alloy production. The developed beneficiation and agglomeration method represent an effective way to convert low-grade manganese sludge into useful metallurgical raw materials. The proposed technology reduces the environmental impact of tailings ponds and opens a viable path to the sustainable use of manganese-containing industrial waste.

Keywords: *manganese-containing waste, technological scheme, manganese concentrate, manganese pellets, strength.*

Received: 23 June 2025
Accepted: 15 December 2025
Available online: 31 December 2025

1. Introduction

The processing of manganese ores produces significant volumes of finely dispersed manganese-containing raw materials [1]. The use of mineral formations of technogenic origin, including finely dispersed crushing products, residues after enrichment, and slags from metallurgical processes, opens up new opportunities for the effective development of the raw material base and reduction of natural resource use by involving secondary resources in the technological cycle. This approach not only significantly reduces the costs associated with traditional mineral extraction but also contributes to solving pressing environmental issues related to the disposal of industrial waste and reducing the anthropogenic impact on the environment [2-5].

Research is being conducted on the enrichment of low-quality iron-manganese raw materials using flotation and magnetic separation processes [6-9].

Study [6] provides data on the processing of ore material containing 17% pyrolusite, 78% calcite, and 4% quartz. In the first stage, using gravity enrichment on separation equipment, a pyrolusite concentrate was obtained, characterized by a specific manganese oxide content of 20%.

Subsequent application of high-intensity magnetic separation increased the MnO content to 44.3% with a total element recovery of 61.3%. Studies have been conducted on the enrichment of fine-grained manganese ore with a low manganese content [8]. Classification followed by a two-stage process of high-intensity magnetic separation (1.7 and 1.1 T) made it possible to obtain an iron-manganese concentrate with a Mn content of 37% and a recovery rate of 48%.

The possibility of gravitational and magnetic enrichment of aged manganese sludge has been studied [10]. Using a 3.0-0.63 mm class screening process and 0.63-0.071 mm class magnetic separation, a concentrate with a manganese content of 38.25% was obtained.

s.temirova2401@gmail.com; abdgulzh888@gmail.com; biryuk.silikat@mail.ru; fischerdametken@gmail.com
Engineering Journal of Satbayev University. eISSN 2959-2348. Published by Satbayev University

For use in metallurgical processes for smelting finely dispersed concentrates obtained by enriching manganese-containing sludge, they must be agglomerated into pellets and briquettes. The strength characteristics, melting and reducing properties of manganese pellets have been studied depending on the nature of the fluxing materials, carbon content, ratio of acidic and basic oxides, and heat treatment conditions [11-17]. As a rule, substandard concentrate of the fine fraction is used for pellet production. Various types of binders are added to the charge to ensure strength characteristics.

Work [18, 19] presents the results of pellet formation using bentonite as a binder. The resulting pellets were dried and then fired at a temperature of 1300°C. According to the assessment, the physical and mechanical properties of the pellets met the requirements for ferroalloy production.

A method for producing composite pellets for silicomanganese production, consisting of manganese ore, iron ore, fine coke, and ferromanganese slag without additional binders, is described [18]. The physical properties of the pellets obtained, such as cracking and reducibility, were significantly improved compared to the original lump manganese ore.

The results of the study [19] confirmed the effectiveness of the thermohydrotreatment method in autoclave conditions for strengthening fluxed manganese material. It was found that the initial (raw) pellets had a strength of about 3.55 kg/pellet, while after autoclave treatment, this figure increased to 40-60 kg/pellet. The samples obtained demonstrated thermal stability and retained their structural integrity under rapid thermal exposure up to 1000°C, which indicates their suitability for smelting carbon ferromanganese.

Thus, it has been established that autoclave-hardened manganese pellets formed from finely dispersed concentrates are characterized by high strength, uniformity in particle size and chemical composition, and are capable of effective carbon reduction under metallurgical process conditions.

In recent years, researchers have shown growing interest in the use of fine-grained manganese residues that remain after ore beneficiation and metallurgical operations. These materials are difficult to handle because of their small particle size and uneven mineral composition, and for that reason they cannot be directly fed into pyrometallurgical processes. This makes the question of how to agglomerate them into a stable, uniform product an important practical issue.

Another point that requires attention is the choice of additives introduced into the pellet mixture. Fluxes, carbon materials, and various silicate components influence the reactions that occur during firing and determine which binding phases eventually form. Several publications report that natural aluminosilicates, clay-rich residues, and diatomite can promote the formation of calcium–silicate and related phases, which improve the strength of pellets under reducing conditions typical of ferroalloy production [20-23].

At the same time, manganese-bearing waste from specific deposits in Kazakhstan has not been investigated in detail. Differences in mineralogical composition, particle shape, impurity content, and moisture content require adjustments to separation stages and pelletizing methods. Therefore, additional research is needed to determine methods for producing agglomerated materials that meet the requirements of metallurgical processing.

The aim of this work was to develop methods for enriching finely dispersed manganese-containing raw materials and obtaining pellets suitable for smelting into ferromanganese alloys based on manganese concentrate.

2. Materials and methods

A sample manganese sludge with a size of -5+0 mm was taken at the Ushkatyn-3 deposit (JSC «Zhayremsky GOK») with a mass of 200 kg. The manganese content in the average sludge sample was 15.04% (15.96%), and the iron content was 6.03% (5.97%).

The following materials were used in the study: manganese concentrate obtained by enriching manganese-containing sludge, diatomite from the Zhalpak deposit, calcium oxide, and coke.

The chemical composition of the raw materials and processed products was determined by analysis using inductively coupled plasma atomic emission spectrometry (ICP-AES) on an Optima 8000 DV (ICP, PerkinElmer, Norwalk, CT, USA), and X-ray fluorescence data was obtained using a Venus 200 wave dispersion spectrometer from PANalytical (Netherlands).

X-ray phase data were obtained on a D8 Advance diffractometer (Bruker AXS GmbH, Karlsruhe, Germany) with a cobalt anode, radiation, Cu. Differential thermal analysis of the mixture for pellet production was performed on a TG-DTA/DSC synchronous thermal analyzer and a STA 449 F3 Jupiter® quadrupole mass spectrometer (NETZSCH, Germany).

The particle size distribution of manganese-containing technogenic raw materials from the Ushkatyn-3 deposit was studied on a sample with a size of -5.0 + 0 mm.

Sieve analysis was performed by sequentially sieving the test sample through a standard set of laboratory sieves, followed by determination of the mass fraction of material retained on each sieve, calculated based on the mass of the initial sample. To evaluate the size distribution of particles in the slurry sample, sieves with mesh sizes of 2.0, 1.0, 0.5, 0.315, 0.16, and 0.1 mm were used. Sieving was performed using a mechanical vibrating analyzer.

3. Results and discussion

The particle size distribution of the material under study is presented in Table 1. The content of manganese, iron, and silicon was determined in the sieve analysis products.

Table 1. Results of sieve analysis of a sample of sludge fraction (–5.0+0) mm from the Ushkatyn-3 deposit

Class, mm	Yield, %	Element content, %		Element distribution, %	
		Mn	Fe	Mn	Fe
+2.0	22.17	16.10	5.10	22.37	18.91
-2.0+1.0	22.44	15.01	5.21	21.08	19.56
-1.0+0.5	24.32	15.92	6.24	24.26	25.38
-0.5+0.315	9.02	16.12	6.81	9.11	10.27
-0.315+0.16	14.25	16.34	7.02	14.58	16.68
-0.16+0.1	3.95	18.30	8.22	4.53	5.43
-0.1+0.0	3.85	16.88	5.86	4.07	3.77
Total	100.0	15.96	5.97	100.0	100.0

The results of the granulometric analysis of manganese-containing sludge from the Ushkatyn-3 deposit (Figures 2 and 3) show that the largest mass is represented by the +0.5 mm size class and accounts for 68.93%, while the other size classes vary from 3.85% to 14.25%. The content and distribution of manganese and iron in different size classes of manganese-containing sludge are shown in Figures 2 and 3. It is shown that the manganese content in different fractions differs insignificantly and ranges from 15.0 to 18.3%. Most of the manganese is concentrated in fractions larger than 0.5 mm.

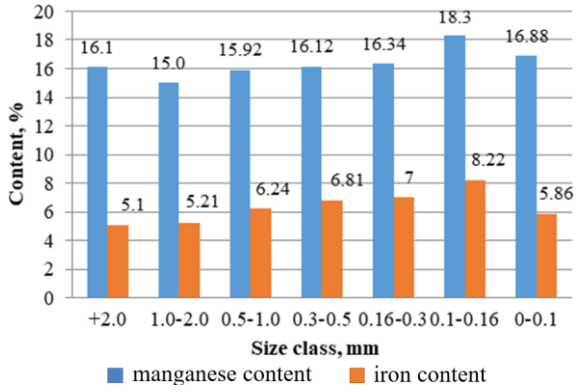

Figure 2. Manganese and iron content in different size classes of manganese-containing sludge

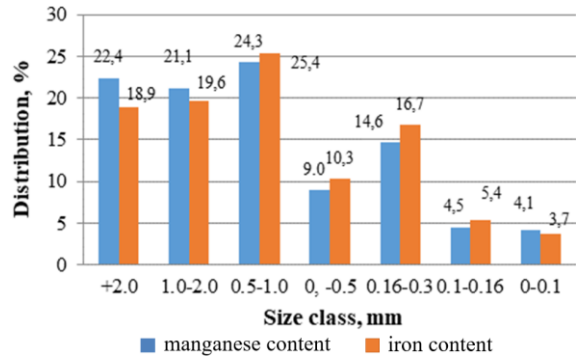

Figure 3. Distribution of manganese and iron in different size classes of manganese-containing sludge

Along with studying the particle size distribution, X-ray fluorescence and X-ray phase analyses of the sample were performed (Table 2 and 3).

Table 2. Results of X-ray fluorescence analysis of a sample of manganese-containing sludge from the Ushkatyn-3 deposit

Components	Component content, %	Components	Component content, %
O	44.12	K	0.273
Mn	16.78	Ca	16.21
Fe	5.52	Ti	0.149
Na	0.301	As	0.036
Mg	0.795	Cu	0.015
Al	1.41	Zn	0.067
Si	6.89	Pb	0.239
P	0.025	Sr	0.127
Cl	0.041	Ba	6.437
S	0.701	Pb	0.002

Table 3. Results of X-ray phase analysis of a sample of manganese- containing sludge

Compound name	Formula	S-Q, %
Calcite	$Ca(_{CO_3})$	41.2
Quartz	SiO_2	13.0
Brownite	$Mn_7\ O_8\ (SiO_4\ )$	10.1
Bixbyite	$FeMnO_3$	9.85
Barite	$BaSO_4$	6.59
Pigeonite	$Mg_{0.69}\ Fe_{0.23}\ Ca_{0.08}\ SiO_3$	6.58
Dikit	$Al_2\ Si_2\ O_5\ (OH)_4$	5.57
Hematite	$Fe_{1.957}\ O_3$	4.59

X-ray phase analysis of manganese-containing sludge showed that the main manganese-containing minerals are braunite $Mn_7O_8(SiO_4)$ and bixbite, while the rock-forming minerals are calcite, quartz, and barite (Table 3).

Manganese ore enrichment is mainly carried out by flotation. To carry out flotation, the difference in density between manganese minerals and waste rock must be at least 400 kg/m^3. Since the density of most manganese minerals is 3200-3800 kg/m^3, and that of waste rock does not exceed 2800 kg/m^3, this operation can be carried out.

A study of the processes of gravitational enrichment of manganese-containing sludge was carried out, resulting in a finely dispersed concentrate with an increased manganese content. A 50.0 kg sample of sludge was screened using sieves of different particle sizes: 2.5, 1.25, and 0.071 mm.

Beneficiation of sludge with particle sizes of -2.5+1.25 and -1.25+0.071 mm was carried out in a jigging machine. The optimal operating parameters are: bed size (manganese grains) – 10-8 mm, bed height – 30-40 mm, pulsation frequency – 350 oscillations/min, oscillation amplitude – 8 mm enrichment of the -0.071+0 mm size class was carried out on concentration tables under the following conditions: table stroke – 14 mm, number of deck oscillations per minute – 240, deck inclination – 35 degrees.

A technological scheme for the gravitational beneficiation of manganese sludge has been developed, allowing the production of a concentrate with a manganese content of 28.5% and iron content of 7.25%. At the same time, the extraction of these components was achieved at a level of 62.01% and 39.85%, respectively (Figure 4).

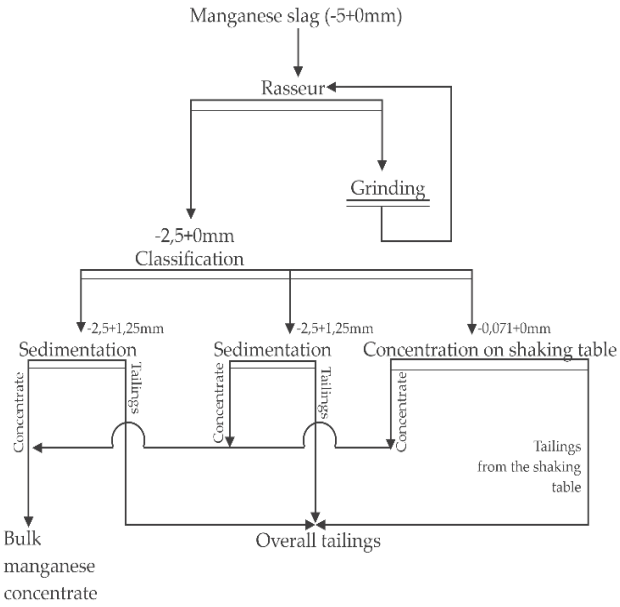

Figure 4. Schematic diagram of gravity enrichment of manganese-containing sludge

The combined manganese concentrate from the tailings and concentration table was separated using a SMP-PR-02 laboratory magnetic separator (manufactured in Ukraine) at a magnetic field strength of 900 mT.

As a result of applying the gravity-magnetic enrichment scheme, a manganese concentrates with a manganese content of 34.9% and iron content of 7.9% was obtained; the extraction rates were 61% and 39%, respectively. The optimal technological parameters for the formation of «raw» pellets from a composite mixture including manganese concentrate, special coke, iron-containing varieties of diatomite, and lime were established. The chemical composition of the starting components is shown in Table 4.

Table 4. Chemical composition of the starting materials

Source material	Oxide content, mass %										
	Mn	SiO_2	Al_2O_3	Fe_2O_3	CaO	MgO	BaO	K_2O	Na_2O	other	ppm
Manganese concentration	34.9	10.31	1.83	14.82	6.86	1.31	7.68	0.17	0.90	5.56	-
Diatomite	-	63.94	8.03	10.30	8.06	9.61	-	-	-	0.6	-
Lime	-	0.23	0.05	0.09	76.32	1.80	-	-	-	0.54	20.97

Manganese concentrate-based pellets were obtained by pelletizing on a laboratory automated mixer-granulator manufactured by Eirich (Figure 5 and 6). Granulation process parameters: steel drum rotation speed – 170 rpm, drum angle – 30(o), drum rotation relative to the swirler – counterclockwise.

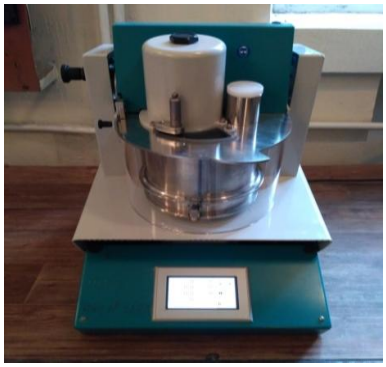

Figure 5. Eirich mixer-granulator

Figure 6. Samples of manganese pellets

Experiments were conducted to obtain pellets based on two compositions with different fractional compositions of manganese concentrate: 1) content of fractions 0.5-0.16 mm – 61.3%; 0.16-0.071 mm – 34.0%; less than 0.071 mm – 4.7%; 2). The particle size distribution of the material under study is as follows:

– the 0.5-0.16 mm fraction accounts for 39.8%;

– fraction 0.16-0.071 mm – 31.2%;

– particles smaller than 0.071 mm account for 29.0%. Kazakh diatomite containing iron oxides (Zhalpak deposit) was used as a binder in the mixture for producing manganese pellets. The chemical composition of diatomite is as follows, in mass %: SiO_2 – 63.94; Al_2O_3 – 8.03; Fe_2O_3 – 10.30; CaO – 8.06; MgO – 9.61; others – 0.6.

Diatomite is a natural material, the main component of which is quartz (69.4%), also containing goethite, barium-manganese, magnesium, calcium-aluminum, and barium silicates (Figure 7).

To obtain pellets, 500 g of the raw material mixture was poured into the mixer-granulator. The mixture was mixed for 30 seconds at a maximum vortex speed of 2000 rpm. When small granules appeared, the vortex speed was reduced to 1000 rpm, followed by powdering of the mixture.

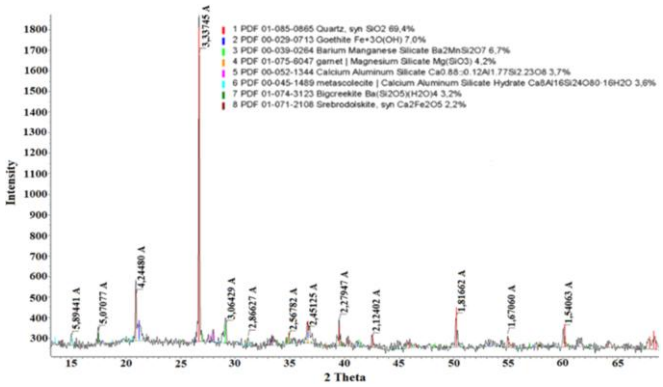

Figure 7. Diffractogram of a diatomite sample

To obtain pellets, 500 g of the raw mixture was poured into the mixer-granulator. The mixture was mixed for 30 seconds at a maximum agitator speed of 2000 rpm. When small granules appeared, the speed of the swirler was reduced to 1000 rpm, followed by powder coating of the mass. After 1 minute, the remaining part of the binder component was added, and the moistened mass was powder coated, reducing the speed of the swirler to 700 rpm. After one minute, the speed of the swirler was reduced to 500 rpm, then to 300 rpm. After continuing granulation at this speed for 3 minutes, the process was completed and the raw pellets were unloaded.

It was found that pellets based on a charge with a high content of fine manganese concentrate (less than 0.071 mm) have high strength characteristics.

To establish the patterns of structural and phase transformations occurring during the heat treatment of manganese pellets, a differential thermal analysis was performed on a mixture with the following composition, in mass %: manganese concentrate – 85, diatomite – 10, calcium oxide – 5 (Figure 8).

In the temperature range of 200-550°C, endothermic effects were observed with extrema at 281.8°C and 495.8°C. They are accompanied by a decrease in the weight of the sample, which indicates the dehydration of iron hydroxides. The combination of an endothermic effect with an extreme at 587.4°C and an inflection point on the DTA curve at 708.2°C may be associated with the decomposition of $(Fe,Mn)CO_{(3)}$ .An intense endothermic effect with an extreme at 836.5ºC reflects the decomposition of calcite. The endothermic effect with maximum development at 1168.9ºC can be attributed to the polymorphic transformation of brownite $3Mn_{(2)}O_{(3)}(Mn,Mg,Ca)SiO_{(3)}$. At 1191ºC, crystallization of the fayalite phase 2FeO·SiO(2) phase. The exothermic effect at 979.8ºC is probably associated with the crystallization of ferroboostite ($CaFe_{(2)}Si_{(2)}O_{(6)}$).

The sintering range of experimental manganese-containing pellets was studied, which was 1160-1200°C, with an optimal pellet firing temperature of 1170°C.

As the firing temperature increases, the strength of the samples increases, but at a temperature of 1200°C, signs of melting are observed.

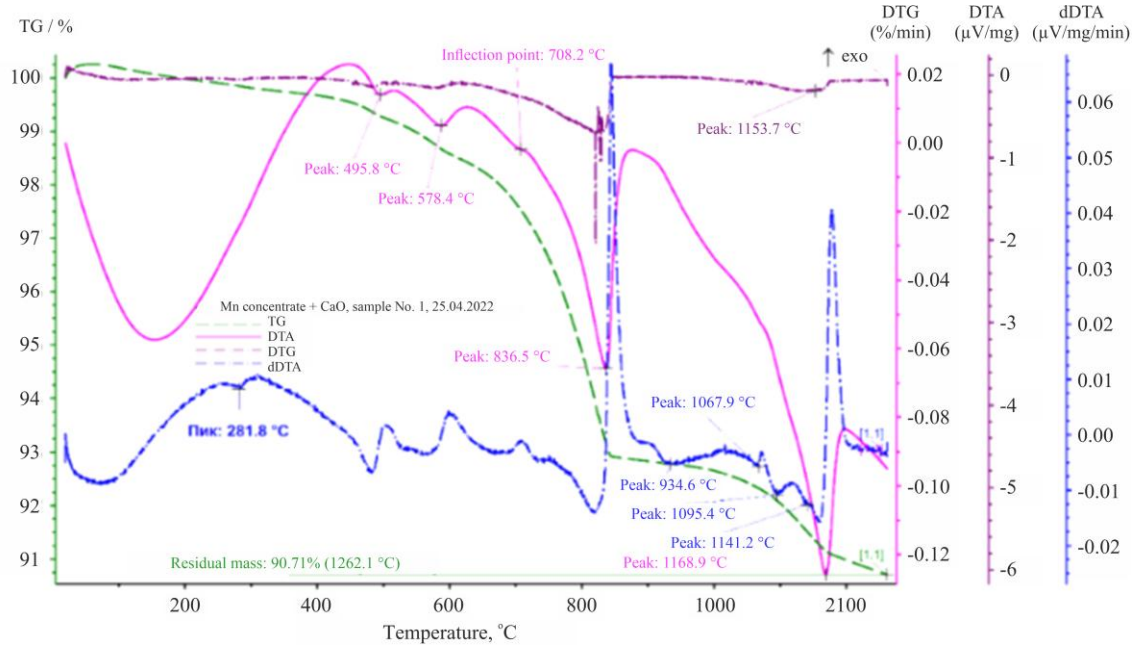

Figure 8. Derivatogram of the charge consisting of manganese concentrate, diatomite, and calcium oxide

X-ray phase analysis of fired compositions based on manganese concentrate with additives revealed that manganese in the pellet structure is present in the form of jacobsite ($MnFe_2O_4$) and hausmannite (Mn_3O_4) phases. The binding part of the structure contains cwalcium and iron silicate – ferrobustamite ($CaFe_2Si_2O_6$), which contributes to the strengthening of pellets and increases their mechanical strength.

The physical and mechanical properties of manganese pellets were determined. For the optimal particle size distribution, pellets were produced using two compositions. In the first composition, the pellet mixture consisted of manganese concentrate (85 wt.%), diatomite (10 wt.%), and calcium oxide (5 wt.%). In the second composition, the charge consisted of manganese concentrate (78 wt.%), diatomite (11 wt.%), calcium oxide (6 wt.%), and coke (5 wt.%).

The pellets exhibited the following properties: open porosity of 27.3% and 34.5%, apparent density of 1.91 and 1.45 g/cm³, and water absorption of 12.5% and 19.2%, respectively. The compressive strength of pellets based on the manganese concentrate–diatomite–CaO mixture was 33.80 kg/pellet, while the addition of coke reduced the strength to 23.28 kg/pellet.

4. Conclusions

A technological scheme has been developed for the beneficiation of finely dispersed manganese-containing raw materials with obtaining a concentrate with a Mn content of 35.2%. The optimal technological parameters for forming pellets from a mixture including manganese concentrate, special coke, diatomite, and lime have been established. By firing at a temperature of 1170°C, it was found that manganese in the obtained pellets is present mainly in the form of jacobsite ($MnFe_2O_4$) and hausmannite (Mn_3O_4), and a phase of ferrobustamite phase, which contributes to the increased strength of the products.

The compressive strength of the formed pellets was 33.8 kg/pellet, which indicates their sufficient mechanical strength. The obtained pellets meet the requirements for raw materials for smelting ferromanganese alloys and can be effectively used in ferroalloy production.

Author contributions

Conceptualization: SST, GZA; Data curation: SST, GZA; Formal analysis: SST, GZA, AAB; Funding acquisition: SST; Investigation: SST; Methodology: SST, AAB; Project administration: SST, AAB; Resources: SST, GZA; Software: DYF, SST; Supervision: SST, GZA; Validation: SST; Visualization: DYF; Writing – original draft: SST, DYF; Writing – review & editing: SST, DYF. All authors have read and agreed to the published version of the manuscript.

Funding

This research was funded by the Science Committee of the Ministry of Science and Higher Education of the Republic of Kazakhstan (Grant No. AP09258880).

Acknowledgements

The authors express their sincere gratitude to the editor and anonymous reviewers for their constructive comments and valuable suggestions, which have significantly improved the quality of this manuscript.

Conflicts of interests

The authors declare no conflict of interest.

Data availability statement

The original contributions presented in this study are included in the article. Further inquiries can be directed to the corresponding author.

References

[1] International Manganese Institute. |Mn| Annual Review. (2019). *Retrieved from*: https://www.manganese.org/wp-content/uploads/2021/04/IMnI-2019-Annual-Review_ENG.pdf

[2] Shekhar, S., Sinha, S., Mishra, D., Agrawal, A. & Sahu, K.K. (2021). Extraction of manganese through baking-leaching technique from high iron containing manganese sludge. *Materials Today: Proceedings, 46(3),* 1499-1504. https://doi.org/10.1016/j.matpr.2020.12.637

[3] Kenzhaliyev, B.K. (2019). Innovative technologies providing enhancement of nonferrous, precious, rare earth metals extraction. *Kompleksnoe Ispol'zovanie Mineral'nogo Syr'a = Complex Use of Mineral Resources*, *3*, 64-75. https://doi.org/10.31643/2019/6445.22

[4] Yessengaliyev, D.A., Baisanov, A.S., Dossekenov, M.S., Kelamanov, B.S. & Almabekov, D.M. (2022). Thermophysical properties of synthetic slags of the FeO - MnO - CaO - Al_2O_3 – SiO_2 system. *Kompleksnoe Ispol'zovanie Mineral'nogo Syr'a = Complex Use of Mineral Resources*, *4*(328), 38-45. https://doi.org/10.31643/2022/6445.38

[5] Shevko, V.M., Aitkulov, D.K., Badikova, A.D. & Tuleyev, M.A. (2021). Ferroalloy production from ferrosilicon manganese dusts. *Kompleksnoe Ispol'zovanie Mineral'nogo Syr'a. = Complex Use of Mineral Resources*, *3*(318), 43-50. https://doi.org/10.31643/2021/6445.27

[6] Mehdilo, A., Irannajad, M. & Hojjati-Rad, M.R. (2013). Characterization and beneficiation of Iranian low-grade manganese ore. *Physicochemical Problems of Mineral Processing*, *49*(2), 725-741. https://doi.org/10.5277/ppmp130230

[7] Dyussenova, S., Lukhmenov, A., Imekeshova, M. & Akimzhanov, Z. (2023). Investigation of the beneficiation of refractory ferromanganese ores «Zhomart» deposits. *Kompleksnoe Ispolzovanie Mineralnogo Syra = Complex Use of Mineral Resources*, *329(2)*, 34-42. https://doi.org/10.31643/2024/6445.14

[8] Cheraghi, A., Becker, H., Eftekhari, H., Yoozbashizadeh, H. & Safarian, J. (2020). Characterization and calcination behavior of a low-grade manganese ore, *Materials Today Communications*, *25*, 101382. https://doi.org/10.1016/j.mtcomm.2020.101382.

[9] Singh, V., Ghosh, T.K., Ramamurthy, Y. & Tathavadkar, V. (2011). Beneficiation and agglomeration process to utilize low-grade ferruginous manganese ore fines. *International Journal of Mineral Processing*, *99*(1-4), 84-86. https://doi.org/10.1016/j.minpro.2011.03.003

[10] Liu, B., Zhang, Y., Lu, M., Su, Z., Li, G. & Jiang, T. (2019). Extraction and separation of manganese and iron from ferruginous manganese ores. A review. *Minerals Engineering*, *131*, 286-303. https://doi.org/10.1016/j.mineng. 2018.11.016

[11] Telkov, Sh.A., Motovilov, I.U., Daruesh, G.S., Kadyrsyzov, D.S. & Taubashev, S.R. (2018). Research of gravitational and magnetic enrichment of aged manganese sludges. *Proceedings Satpayev's readings «Innovative solutions to traditional problems: Engineering and technology»*, *2*, 527-531. Retrieved from: https://official.satbayev.university/ru/materialy-satpaevskikh-chteniy

[12] Brynjulfsen, T., Tangstad, M. (2013). Melting and reduction of manganese sinter and pellets. *Proceedings of the Thirteenth International Ferroalloys Congress «Efficient technologies in ferroalloy industry»*, 137-147. Retrieved from: https://www.pyrometallurgy.co.za/InfaconXIII/0137-Brynjulfsen.pdf

[13] Faria, G.L., Tenório, J.A.S., Jannotti, N. Jr., da S. & Araújo, F.G. (2015). A geometallurgical comparison between lump ore and pellets of manganese ore. *International Journal of Mineral Processing*, *137*, 59-63. https://doi.org/10.1016/j.minpro.2015.03.003

[14] Zhang, Y., Zhang, B., Liu, B., Huang, J., Ye, J. & Li, Y. (2022). Physicochemical Aspects of Oxidative Consolidation Behavior of Manganese Ore Powders with Various Mn/Fe Mass Ratios for Pellet Preparation. *Materials*, *15*(5), 1722. https://doi.org/10.3390/ma15051722

[15] Zhang, Y., Liu, B., You, Zh., Su, Z., Luo, W., Li, G. & Jiang, T. (2016). Consolidation Behavior of High-Fe Manganese Ore Sinters with Natural Basicity. Mineral Processing and Extractive Metallurgy Review. *An International Journal*, *37*(5), 333-341. https://doi.org/10.1080/08827508.2016.1218870

[16] Zhunusov, A., Tolymbekova, L., Abdulabekov, Ye., Zholdubayeva, Zh. & Bykov, P. (2021). Agglomeration of manganese ores and manganese containing wastes of Kazakhstan. *Metalurgija*, *60*(1-2), 101-103. https://hrcak.srce.hr/file/357485

[17] Zhu, D., Chun, T., Pan, J. & Zhang, J. (2013). Influence of basicity and MgO content on metallurgical performances of Brazilian specularite pellets. *International Journal of Mineral Processing*, *125*, 51-60. https://doi.org/10.1016/j.minpro.2013.09.008

[18] Yoshikoshi, H., Takeuchi, O., Miyashita, Ts., Kuwana, T. & Kishikawa, K. (1984). Development of composite cold pellet for silico-manganese production. *Transactions of the Iron and Steel Institute of Japan*, *24*(6), 492-497. https://doi.org/10.2355/isijinternational1966.24.492

[19] Shchedrovitsky, V.Ya., Eliseev, S.B. & Kopyrin, I.A. (1990). Study of technology for producing manganese-fluxed autoclave pellets and smelting high-carbon ferromanganese using them. *Collection of conference materials «Theory and Practice of Manganese Metallurgy»*, 20-22.

[20] Navaei, Sh., Ghorbani, M., Sheibani, S., Hosseini, L. & Zare, M. (2025). A review on hematite concentrate pelletization: effect of process parameters on iron ore pellet quality. *Journal of Materials Research and Technology*, *38*, 4849-4859. https://doi.org/10.1016/j.jmrt.2025.08.295

[21] Gonidanga, B.S., Njoya, D., Lecomte-Nana, G. & Njopwouo, D. (2019). Phase Transformation, Technological Properties and Microstructure of Fired Products Based on Clay-Dolomite Mixtures. *Journal of Materials Science and Chemical Engineering*, *7*(11), 1-14. https://doi.org/10.4236/msce.2019.711001

[22] Cultrone, G., Rodriguez-Navarro, C., Sebastian, E., Cazalla, O. & De la Torre, M.J. (2001). Carbonate and silicate phase reactions during ceramic firing. *European Journal of Mineralogy*, *13*, 621-634. https://doi.org/10.1127/0935-1221/2001/0013-0621.

[23] Shtepenko, O., Hills, C., Brough, A. & Thomas, M. (2006). The effect of carbon dioxide on β-dicalcium silicate and Portland cement. *Chemical Engineering Journal*, *118*(1–2), 107-118. https://doi.org/10.1016/j.cej.2006.02.005

Марганец бар техногендік қалдықтардан марганец түйіршіктерін алу

С.С. Темирова, Г.Ж. Абдыкирова, А.А. Бирюкова, Д.Е. Фишер*

Металлургия және кен байыту институты, Алматы, Қазақстан

**Корреспонденция үшін автор: fischerdametken@gmail.com*

Аңдатпа. Марганецке бай өнеркәсіптік қалдықтарды қайта өңдеу таукен өндірісі аймақтарында маңызды технологиялық және экологиялық қиындық тудырады, себебі ол ұзақ мерзімді қалдықтардың жиналуын азайтады және ферроқорытпа өндірісі үшін құнды қосымша шикізат болып табылады. Бұл зерттеуде Үшқатын-3 кен орнынан («Жайрем ГОК» АҚ) алынған ұсақ түйіршікті марганец шламы бөлшектердің мөлшерін талдау, рентгендік флуоресценциялық спектроскопия, рентгендік дифракция, ICP-AES және дифференциалды термиялық талдау әдістерін қолдана отырып мұқият зерттелді. 15.0-18.3% Mn құрайтын бастапқы техногендік материалдың барлығы дерлік барит, кварц, биксбиит, кальцит және брауниттен тұрды. Анықталған гранулометриялық және минералогиялық

қасиеттерге сүйене отырып, гравитациялық-магниттік байыту ағындық схемасы жасалды. Джиггинг, концентрация кестелері және жоғары қарқынды магниттік бөлуді қолдана отырып, тізбекті өңдеу нәтижесінде Mn мөлшері 34.9-35.2% және қалпына келтіруі шамамен 61% болатын ұсақ дисперсті марганец концентраты алынды. Алынған концентратты пайдаланып, кальций оксиді, табиғи темірі бар диатомит және кейбір құрамдарда кокс бар түйіршіктеу қоспалары жасалды. Эйрих араластырғыш-грануляторында түйіршіктеу кезінде жасыл түйіршіктердің пайда болуы байланыстырушы заттың құрамы мен бөлшектердің мөлшерінің таралуына байланысты зерттелді. Композиттік қоспаның термиялық мінез-құлқы TGA-DTA/DSC және квадрупольді масс-спектрометрияны қолдану арқылы зерттелді, бұл 200-1160°C температура диапазонында марганец фазаларының дегидратациясын, карбонаттың ыдырауын және полиморфты түрленулерін анықтады. Жартылай балқымай, жеткілікті фазалық конденсацияны қамтамасыз ететіндіктен, күйдіру процесі 1170°C оңтайлы күйдіру температурасы екенін дәлелдеді. Ферробустамиттің ($CaFe_2Si_2O_4$), гаусманниттің (Mn_3O_4) және якобситтің ($MnFe_2O_4$) пайда болуы күйдірілген түйіршіктердің рентгендік дифракциялық талдауы арқылы расталды. Бұл агломераттардың құрылымдық тұтастығын нығайтатын ферросилиций кальцийін байланыстыру фазасы. Бітелген түйіршіктердің жоғары механикалық беріктігі (бір түйіршікте 33.8 кг-ға дейін), көрінетін тығыздығы 1.45-1.91 г/см³ және ашық кеуектілігі 27-35% олардың ферромарганец қорытпасын өндіруге арналған шикізат ретінде жарамдылығын растайды. Әзірленген байыту және агломерация әдісі төмен сұрыпты марганец шламын пайдалы металлургиялық шикізатқа айналдырудың тиімді тәсілін білдіреді. Ұсынылған технология қалдық қоймаларының қоршаған ортаға әсерін азайтады және марганец бар өнеркәсіптік қалдықтарды тұрақты пайдалануға жол ашады.

Негізгі сөздер: *құрамында марганец бар қалдықтар, технологиялық сұлба, марганец концентраты, марганец түйіршіктері, беріктігі.*

Получение марганцевых окатышей из марганецсодержащих техногенных отходов

С.С. Темирова, Г.Ж. Абдыкирова, А.А. Бирюкова, Д.Е. Фишер*

Институт металлургии и обогащения, Алматы, Казахстан

**Автор для корреспонденции: fischerdametken@gmail.com*

Аннотация. Переработка богатых марганцем промышленных отходов представляет собой серьезную технологическую и экологическую проблему в горнодобывающих регионах, поскольку она снижает долгосрочное накопление отходов и обеспечивает ценное дополнительное сырье для производства ферросплавов. В данном исследовании был проведен тщательный анализ мелкозернистого марганцевого шлама с месторождения Ушкатын-3 (АО «Жайремский ГОК») с использованием гранулометрического анализа, рентгенофлуоресцентной спектроскопии, рентгеновской дифракции, ИСП-АЭС и дифференциального термического анализа. Практически весь исходный техногенный материал, содержащий 15.0-18.3% Mn, состоял из барита, кварца, биксбиита, кальцита и браунита. На основе выявленных гранулометрических и минералогических свойств была разработана технологическая схема гравитационно-магнитного обогащения. Последовательная обработка с использованием отсадочных машин, концентрационных столов и высокоинтенсивной магнитной сепарации позволила получить мелкодисперсный марганцевый концентрат с содержанием Mn 34.9-35.2% и выходом примерно 61%. Из полученного концентрата были изготовлены гранулированные смеси, содержащие оксид кальция, природный железосодержащий диатомит и, в некоторых составах, кокс. Исследовано образование зеленых гранул в процессе гранулирования в смесителе-грануляторе Eirich в зависимости от содержания связующего и гранулометрического состава. Термическое поведение композитной смеси было изучено с помощью ТГА-ДТА/ДСК и квадрупольной масс-спектрометрии, которые выявили дегидратацию, разрушение карбонатов и полиморфные превращения марганцевых фаз в диапазоне температур 200-1160°C. Поскольку процесс спекания обеспечивает адекватную консолидацию фаз без частичного плавления, было доказано, что оптимальной температурой обжига является 1170°C. Рентгенодифракционный анализ обожженных гранул подтвердил образование ферробустамита ($CaFe_2Si_2O_4$), гаусманнита (Mn_3O_4) и якобсита ($MnFe_2O_4$). Это фаза, связывающая ферросилиций и кальций, которая укрепляет структурную целостность агломератов. Высокая механическая прочность спеченных гранул (до 33.8 кг на гранулу), кажущаяся плотность 1.45-1.91 г/см³ и открытая пористость 27-35% свидетельствуют об их пригодности в качестве сырья для производства ферромарганцевых сплавов. Разработанный метод обогащения и агломерации представляет собой эффективный способ преобразования низкосортного марганцевого шлама в полезное металлургическое сырье. Предлагаемая технология снижает воздействие хвостохранилищ на окружающую среду и открывает перспективный путь к устойчивому использованию промышленных отходов, содержащих марганец.

Ключевые слова: *марганецсодержащие отходы, технологическая схема, марганцевый концентрат, марганцевые окатыши, прочность*.

Publisher's note

All claims expressed in this manuscript are solely those of the authors and do not necessarily represent those of their affiliated organizations, or those of the publisher, the editors and the reviewers.

SATBAYEV UNIVERSITY

Engineering Journal of Satbayev University

Volume 147 (2025), Issue 6, 24-39

https://doi.org/10.51301/ejsu.2025.i6.04

Structural controls on rare-metal mineralization: Depth-specific mapping of economic deposits in Nigeria Basement Complex

E. Abraham[1*], M. Abdulfarraj[2], M. Emetere[3], A. Usman[1], I. Ikeazota[1]

[1]*Alex Ekwueme Federal University, Ikwo, Nigeria*
[2]*Abdulaziz University, Jeddah, Saudi Arabia*
[3]*Bowen University, Iwo, Nigeria*

**Corresponding author: ema.abraham@funai.edu.ng*

Abstract. This study aims to identify prospective zones for mineral exploration and enhance understanding of mineralization processes within Precambrian terrains. High-resolution aeromagnetic data were analyzed using integrated geophysical techniques such as Analytic Signal, Tilt Derivative, Phase Symmetry, Source Parameter Imaging, Butterworth bandpass filtering, 3D magnetic anomaly inversion, and Euler Deconvolution to delineate subsurface structures and determine their spatial distribution, depths, and relationships to mineral occurrences. The results revealed NE-SW and NW-SE trending lineaments corresponding to major shear zones and fault systems that govern mineral emplacement. Shallow sources (250-500 m) are associated with industrial minerals such as clay, intermediate depths (500-720 m) relate to rare-metal pegmatites hosting columbite-tantalite and wolframite, while deep-seated structures (>1200 m) indicate potential source regions for mineralizing fluids. High-amplitude analytic signal anomalies (0.04-0.05 nT/m) coincide with geological contacts and structural boundaries marking zones of potential mineralization. This represents the first comprehensive investigation of subsurface mineralized structures in the region, and by applying multiple geophysical processing techniques, previously unmapped structural features were exposed and the vertical continuity of mineralized zones confirmed. The findings provide depth-specific mapping of economic mineral deposits, offering valuable insights for targeted exploration efforts and enabling more precise, cost-effective strategies for locating columbite-tantalite, wolframite, kaolin, and other economically significant minerals in the Basement Complex.

Keywords: *magnetic data, minerals exploration, depths, structural controls, mining, basement complex.*

Received: 20 March 2025
Accepted: 7 November 2025
Available online: 30 December 2025

1. Introduction

Variations in magnetic field of the earth at some regions can indicate the presence of certain mineral deposits or geological structures. Exploration and discovery of mineral resources play a crucial role in the economic development of nations [1], particularly in regions with untapped geological potential. In recent years, advanced geophysical techniques has revolutionized the field of mineral exploration, offering more precise and cost-effective methods for identifying promising deposits [2-7]. Among these techniques, the analysis of magnetic anomaly signatures has emerged as a powerful tool for unraveling the hidden subsurface mineralized structures of economic value [5].

Nigeria, with its diverse geological landscape, is recognized for its mineral resource potential [7]. However, large areas of the country, particularly within the Precambrian Shield regions, remain underexplored. The Kaduna-Nasarawa region, situated within the Nigerian Precambrian Basement Complex, represents one such promising yet understudied region [7]. This area, characterized by its ancient rock formations and complex tectonic history is itself a segment of the West African Craton and holds significant potential for various mineral deposits, including clay, columbite, garnet kaolin/kaolinitic clay, mica, talc, tantalite, tourmaline, wolframite, iron ore, gold, and rare earth elements [8, 9]. Recent advancements in magnetic survey technologies and data interpretation methods have opened new avenues for understanding the subsurface geology of such complex terrains [2-4]. By detecting subtle variations in the magnetic field anomalies caused by differences in rock magnetization, these techniques have revealed valuable information about underlying geological structures and potential mineralization zones [5].

Over the past few decades, several studies [10, 11] have been conducted to explore the mineral potentials and geological characteristics of this region. These studies have utilized various geological and geophysical techniques to understand the structural framework and mineralization processes within the basement complex. The ability to detect magnetic field variations in the Earth, caused by subsurface magnetic minerals such as magnetite and ilmenite presents magnetic surveys as essential tools for exploring basement complex terrains [12]. These variations of magnetic anomalies, are key

ema.abraham@funai.edu.ng; mmrajab@kau.edu.sa; emetere@yahoo.com; ayatuusman@gmail.com; iheanyi.ikeazota@gmail.com
Engineering Journal of Satbayev University. eISSN 2959-2348. Published by Satbayev University

indicators of geological structures, such as faults, fractures, intrusions and shear zones, which often serve as conduits for mineralizing fluids. In the Kaduna-Nasarawa Precambrian Shield (KNPS), interpreting these magnetic anomalies can reveal hidden mineral deposits and provide insights into the structural controls governing mineralization. However, despite the recognized mineral potential of this region, detailed geophysical studies to delineate these subsurface structures, depth extents and trends are relatively limited, necessitating the need for this study. This study will shed light on the enclosed geological features of the Kaduna-Nasarawa region, paving the way for a more targeted and efficient mineral exploration efforts in the region. The area under investigation is basically parts of four states, Kaduna, Nasarawa, Plateau and Bauchi States of northern Nigeria and covers an area of 18150 km^2. It is bounded by Longitudes 8°00'-9°30' E and Latitudes 9°00'-10°00' N (Figure 1).

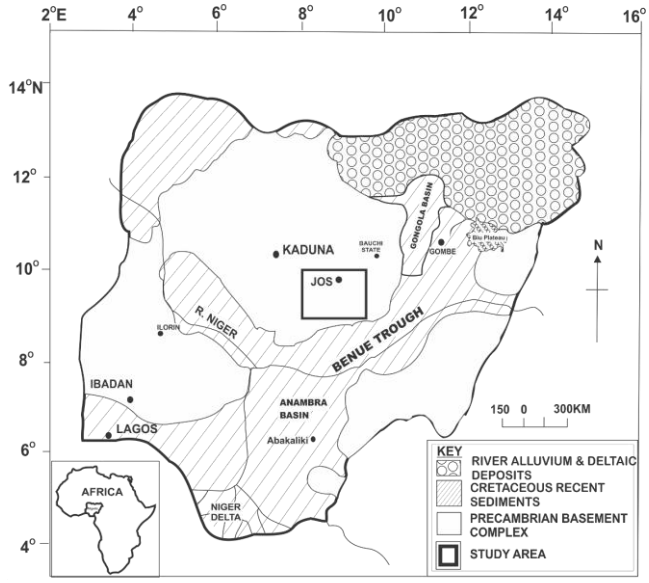

Figure 1. Map of Nigeria. The map also displays an overview geological setup within the region (modified from [2])

Early geological mapping efforts, such as those by McCurry [11] and Rahaman [10], provided a foundational understanding of the lithological composition and structural features of the region. These studies highlighted the presence of various rock types, including syenite, quartz, gabbro, migmatites, gneisses, schists, and granitoids, and emphasized the importance of fault systems in controlling mineralization. Subsequent geochemical surveys, conducted by Ogezi [9] and other researchers, identified significant concentrations of tin, columbite, gold, and other minerals, particularly in association with the Younger Granites of the Jos Plateau and quartz veins within the schist belts. Woakes et al. [13] demonstrated the utility of aeromagnetic data in revealing the structural framework of the Crystalline Basement Complex of Nigeria and its influence on mineralization. These studies showed that major fault systems, trending NE-SW, NW-SE, and E-W, are key structural features that control the emplacement of mineral-rich fluids, thereby influencing the distribution of mineral deposits [7]. Although these studies have provided insights into the region's geology, they have often been limited by reach and resolution of the data leaving significant gaps in the understanding of the subsurface geology and mineralization processes of the basement complex. Other previous investigations relied on surface mapping, which may not fully capture the complexity of the subsurface structures and their role in mineralization. Moreover, the region's challenging terrain and dense vegetation often make traditional geological mapping difficult, further complicating efforts to accurately delineate mineral deposits. There is a pressing need for a more comprehensive geophysical approach that can provide higher resolution data and better constrain the subsurface structures and mineralization zones [2, 4, 5, 12].

Despite the mineral potential of the study area, comprehensive geophysical exploration remains limited. However, some insights have been provided by Ugwu et al. [14], who analyzed aeromagnetic data in the Jos Plateau region, which encompasses a smaller part of our study area. Their analysis revealed distinct structural lineaments oriented in multiple directions: northeast-southwest (NE-SW), northwest-southeast (NW-SE), east-west (E-W), and north-south (N-S). These structural trends were interpreted as potential fault and fracture systems, suggesting a complex tectonic history that may have influenced mineralization patterns in the region. The correlation between these structural trends and mineral occurrences, warrants further investigation through integrated geophysical approaches. Our study aims to investigate the magnetic anomaly signatures within the KNPS and their implications for mineral exploration. We seek to identify and characterize promising areas for further exploration efforts through the integration of high-resolution aeromagnetic data with geological information. The increasing demand for sustainable mining practices and the need to optimize exploration strategies to minimize environmental impact and maximize economic benefits in the mining and exploration industry makes this study very timely.

1.1. Geological setting

The Kaduna-Nasarawa region is situated within the Nigerian Precambrian Basement Complex, a crucial component of the Trans-Saharan Belt (TSB) of West Africa [15]). This belt, extending from Algeria through Niger and Nigeria to Benin, represents a major Pan-African orogeny that occurred during the late Neoproterozoic to early Cambrian period (ca. 600-540 Ma) [16]. The Nigerian Basement Complex, covering approximately half of Nigeria's landmass, plays a pivotal role in understanding the region's tectonic evolution and mineralization potential [7]. This complex is characterized by a diverse assemblage of metamorphic and igneous rocks, primarily of Precambrian age and is broadly divided into three major lithological units (Figure 2):

1. Migmatite-Gneiss Complex; which forms the basement sensu stricto and is considered to be Archean to Early Proterozoic in age (>2000 Ma). It also consists of high-grade gneisses, migmatites, and local occurrences of meta-supracrustal rocks [17].

2. Schist Belts; which are predominantly metasedimentary and metavolcanic rocks of Late Proterozoic age (900-600 Ma). They occur as N-S trending belts within the Migmatite-Gneiss Complex and are interpreted as ancient sedimentary basins that were deformed and metamorphosed during the Pan-African orogeny [18].

3. Older Granites; which are Pan-African intrusive suites emplaced during the late Neoproterozoic to early Cambrian (750-450 Ma). They range in composition from tonalite to granite and are typically unfoliated to weakly foliated [19].

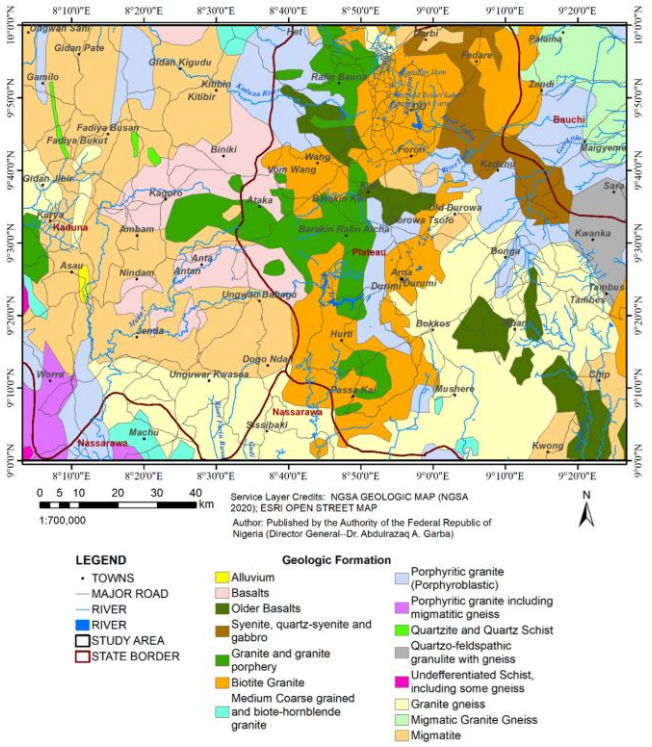

Figure 2. Geologic map of the study area (Map was extracted from the Nigerian Geological Survey Agency [8])

The Kaduna-Nasarawa area specifically straddles the boundary between the Migmatite-Gneiss Complex and the Schist Belts, providing a unique geological setting with potential for various mineralization styles. The dominant lithologies in the Kaduna-Nasarawa region are the Migmatitic gneisses that forms the basement rocks and are composed of quartzo-feldspathic minerals with variable amounts of biotite and hornblende (Figure 2). Complex folding and banding patterns, with leucosomes of granitic composition and melanosomes rich in mafic minerals are noticeable [10]. Predominant quartz-mica schists, with occasional occurrences of graphitic and calc-silicate schists has also been recorded and they typically contain quartz, muscovite, and biotite as major minerals, with garnet, staurolite, and kyanite as common metamorphic index minerals indicating amphibolite facies metamorphism [20]. Amphibolites occur as concordant bands within the gneisses and schists, and often associated with meta-ultramafic bodies. They are composed mainly of hornblende and plagioclase, with minor amounts of quartz, biotite, and epidote. Some amphibolites may represent metamorphosed mafic volcanic rocks or intrusions [21]. Occurring as resistant ridges, are quartzites which are often ferruginous and may host significant iron mineralization. They are composed predominantly of quartz with minor amounts of muscovite, biotite, and magnetite. The ferruginous quartzites, also known as banded iron formations (BIFs), consist of alternating bands of iron-rich (mainly hematite and magnetite) and silica-rich layers [22]. The granitoids include both the Older Granites (Pan-African) and younger intrusive bodies and they range in composition from granodiorite to syenite. The Older Granites are typically porphyritic, with large K-feldspar phenocrysts in a matrix of quartz, plagioclase, biotite, and hornblende. Younger intrusions include pegmatites, which are often associated with rare metal mineralization [23]. Meta-ultramafic rocks (although less common), occur as small bodies within the schist belts and are composed mainly of serpentinized peridotites and pyroxenites. They may represent remnants of oceanic crust and could be associated with nickel and chromium mineralization [24].

The KNPS region has undergone multiple phases of deformation, resulting in a complex structural framework. Some of the key structural features are the NNE-SSW trending foliation, which is the dominant structural grain in the area. This foliation is associated with the main phase of the Pan-African orogeny and is particularly well-developed in the schists and gneisses [25]. The tight to isoclinal folds, often with axial planar cleavage and typically associated with the deformation phase having axes that plunge gently to moderately towards the NNE or SSW [26]. The shear zones and faults, some of which may control mineralization. Major shear zones in the region trend NE-SW and NW-SE, and often show evidence of multiple reactivation events. These structures have been noted to host significant gold mineralization, particularly where they intersect favorable lithologies [27]. Late-stage brittle fractures and joints, which often trend E-W and may be related to Mesozoic rifting events associated with the break-up of Gondwana [28]. Mylonitic zones, particularly along the margins of granitic intrusions, indicating high-strain deformation during the emplacement of the Older Granites [23]. Okonkwo and Folorunso [30] showed that the Migmatite-Gneiss Complex typically shows evidence of high-grade metamorphism, reaching upper amphibolite to granulite facies conditions (T = 650-800°C; P = 6-10 kbar) and the Schist Belts generally exhibit lower to middle amphibolite facies metamorphism (T = 500-650°C; P = 4-7 kbar), with local variations depending on proximity to intrusive bodies.

Therefore, the geological setting of the KNPS region provides favorable conditions for various types of mineralization (Figure 3) to include: Gold, which usually associated with quartz veins in shear zones within the schist belts and may be related to hydrothermal activity during the late stages of the Pan-African orogeny [18].

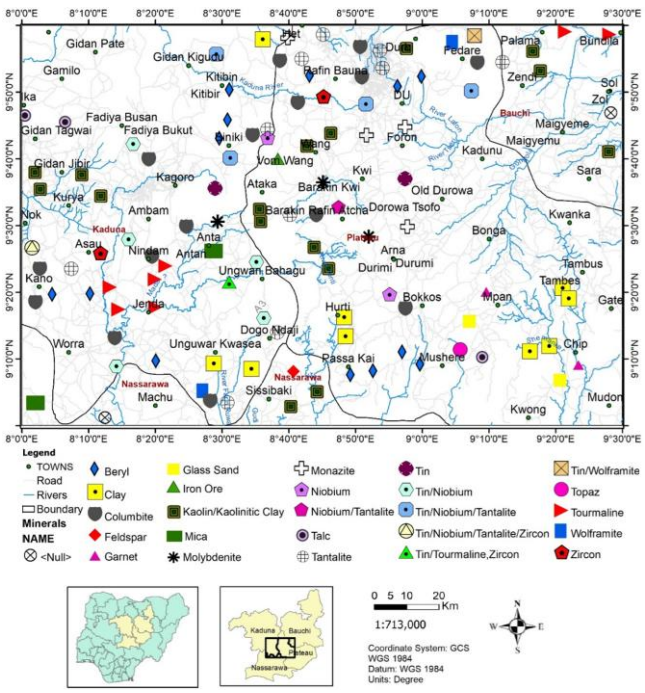

Figure 3. Mineral resources map of the study area (extracted from Mineral map of Nigerian Geological Survey Agency [8])

Iron ore hosted in banded iron formations and ferruginous quartzites known to contain significant reserves of hematite and magnetite [22]. Rare Earth Elements (REE) which are potentially concentrated in pegmatites and alkaline granites. The pegmatites also host significant tantalum and niobium mineralization (Figure 3) [29]. Gemstones including beryl (aquamarine, emerald) and tourmaline in pegmatitic bodies, particularly those associated with the younger granitic intrusions. Nickel and Chromium, potentially associated with the meta-ultramafic bodies. Although economic deposits of nickel and chromium have not yet been ascertained in the region, we believe this study would provide ample information of the structures within the suspected regions for further assessments and action.

Other mineral occurrences have been documented in the region. Some of them includes Clay and Kaolinitic Clay (Figure 3), which are widely distributed throughout the region, and are primarily derived from the weathering of feldspar-rich rocks such as granites and gneisses. The quality and quantity of these clay deposits make them potential resources for the ceramics and paper industries. Columbite and Tantalite also recorded in the N, NW and southern regions are often referred to collectively as coltan and are found in the pegmatites associated with the Older Granite suite. They typically occur as accessory minerals in pegmatites, often in association with cassiterite (tin ore).

1.2. Mineral setting

The Nasarawa area, in particular, has been noted for its columbite-tantalite mineralization, which is part of the larger Jos Plateau tin field (Figure 3). Garnets are common in the metamorphic rocks of the region (Kwi location), particularly in the higher-grade gneisses and schists. Almandine garnet is the most common variety, often found in garnet-mica schists and as porphyroblasts in gneisses [21]. While most occurrences are of mineralogical interest, some deposits may be of gem quality. Various types of mica, including muscovite and biotite, are abundant in the region's Older Granitoid rocks (SE region). Large mica books, of potential economic interest, are primarily associated with pegmatites [18]. The Older Granite pegmatites in particular have been known to host significant mica deposits. Talc deposits in the region are typically associated with ultramafic bodies that have undergone hydrothermal alteration. These deposits often occur as talc-schists or steatite bodies within the metavolcanic sequences of the schist belts [20]. The quality and extent of these deposits vary, with some potentially suitable for industrial applications. Tourmaline mineral is commonly found in the pegmatites of the region, often in association with other rare-metal mineralization. Tourmaline in the Kaduna-Nasarawa area ranges from common schorl to gem-quality elbaite varieties [30].

Some pegmatites in the region have yielded gem-quality tourmalines of various colors. While Wolframite is less common than some of the other minerals documented in the region, it has been reported at the NE region of the study are (Palama location) (Figure 3) and typically associated with quartz veins in granitic and metamorphic terrains [18]. We belive the distribution of these minerals is closely tied to the regional geology as the pegmatites, particularly those associated with the Older Granites, are the primary hosts for columbite, tantalite, beryl, tourmaline, and some high-quality mica deposits. The metamorphic rocks, especially the schists and gneisses, host the garnet and some of the mica occurrences (Figure 3). Clay and kaolinitic clay deposits are found in the weathered profiles developed over feldspar-rich basement rocks in the Central region of the study area. Talc deposits are associated with ultramafic bodies within the schist belts found in the NW and SE regions.

2. Methods

For this investigation, we analyzed magnetic field data collected during an extensive aerial survey of Nigeria. Fugro Airborne Surveys conducted the fieldwork from 2005-2009 under the direction of the Nigerian Geological Survey Agency (NGSA). The aircraft maintained 500 m spacing between flight lines while traveling northwest to southeast at 80 meters above ground level. After collection, the data was organized into gridded maps, with each grid covering a half-degree square area.

To ensure high data quality, the team accounted for both regional magnetic field variations and daily fluctuations. The magnetic measurements underwent Reduction to Equator (RTE) processing following established methodologies [2], [31]-[36]. This mathematical transformation, performed using fast Fourier transform algorithms, incorporated the local magnetic parameters: -2.15° declination and -13.91° inclination. The final processed aeromagnetic data appears in Figure 4.

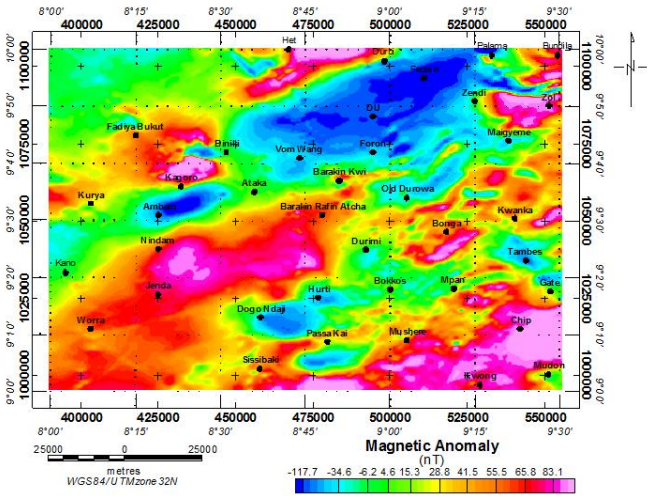

Figure 4. Residual aeromagnetic anomaly map

The map displayed notable variations in magnetic intensity, reflecting a range of distinct magnetic properties. High positive magnetic anomalies (>84.1 nT) are spotted around Chip, Zol, Het and Jenda locations. These regions are traced to the granites and older basalts of the Precambrian basement complex and indicates the presence of high magnetic mineral at these locations. Significant lower magnetic anomalies (<-115 nT) are noticeable in the northern and NE regions of the study area and is traced to the highly fractured and porphyritic granite formation in the locations.

2.1. Source parameter imaging (SPI)

Magnetic source depth estimation has been enhanced by the SPI method, which automatically analyzes gridded magnetic data. Unlike traditional approaches, SPI functions effectively regardless of magnetic inclination and declination values, making pole reduction unnecessary during analysis [2]. Recent field testing with drill-confirmed data sources

shows that SPI consistently achieves depth predictions within ±20% accuracy, matching the precision of established methods like Euler deconvolution. Nevertheless, SPI surpasses Euler deconvolution by producing more extensive and internally consistent solution sets, enabling a better visualization of underground formations.

The theoretical foundation of SPI rests on a step-source model [37]. This model is governed by the following mathematical relationship:

$$Depth = 1/K_{\max}\,, \tag{1}$$

where: $K_{\max}$ is the peak value of the local wavenumber K over the step source.

$$K = \sqrt{\left(\frac{dA}{dx}\right)^2 + \left(\frac{dA}{dy}\right)^2}\,, \tag{2}$$

where:

$$Title\ derivative\ A = \tan^{-1}\left\{\frac{\left[\frac{dM}{dz}\right]}{\left(\frac{dA}{dx}\right)^2 + \left(\frac{dA}{dy}\right)^2}\right\}, \tag{3}$$

where: M is the total magnetic field anomaly grid.

The outcome of SPI computations is presented in Figure 5.

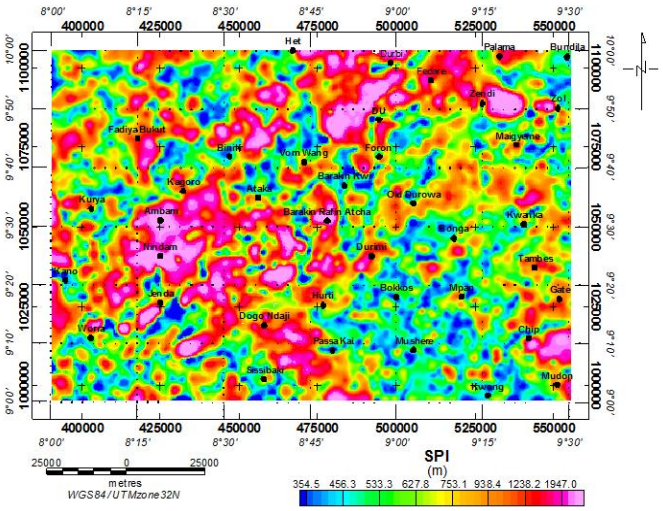

Figure 5. SPI results for the study region

2.2. Butterworth bandpass filter

The application of frequency-selective signal processing was achieved through a Butterworth bandpass filter, chosen for its maximally flat response in the bandpass region. This filtering approach effectively isolates specified frequency ranges while suppressing others, offering precise control over the filter's roll-off characteristics without altering the central wavenumber. The filter order can be adjusted to mitigate potential Gibbs phenomena, ensuring optimal signal preservation within the frequency band of interest. Unlike alternative filtering methods that may introduce bandpass ripples, the Butterworth filter's smooth response makes it particularly suitable for geophysical data processing where signal integrity is paramount. The Butterworth bandpass filter's transfer function, $H(s)$, is formulated based on its low-pass prototype and can be expressed as follows [2], [38], [39]:

$$H(s) = \frac{K}{\sqrt{1+\left(\frac{S}{\omega_c}\right)^{2N}}}\,, \tag{4}$$

where: $s = j\omega$ is the complex frequency variable; ω_c is the cutoff frequency; N is the order of the filter; K is the gain at $\omega = 0$.

For a bandpass filter, the transfer function can be expressed as:

$$H(s) = \frac{Ks^{2N}}{\prod_{k=1}^{N}\left(s^2 + 2s\cos\left(\frac{(2k-1)\pi}{2N}\right)\omega_0 + \omega_0^2\right)}\,. \tag{5}$$

The parameter ω_0 represents the central frequency of the bandpass filter. This filter was implemented using the Geosoft Oasis software, and the resulting output is shown in Figure 6. The filter order was carefully chosen to achieve an optimal trade-off between achieving sharp frequency cut-offs and minimizing ringing effects.

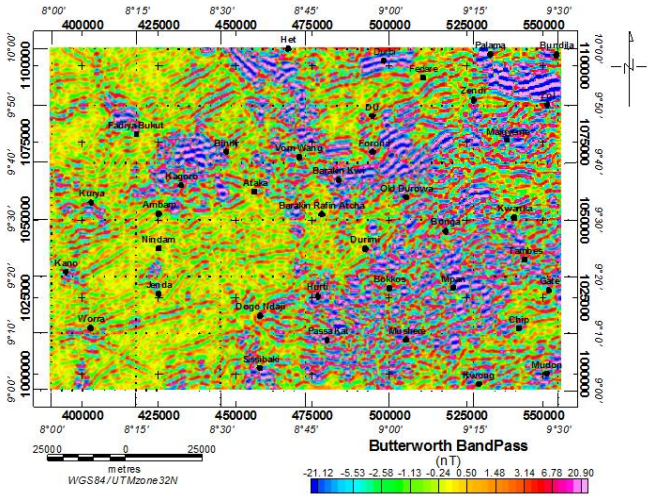

Figure 6. Butterworth bandpass map for the study area

Figure 6 was achieved by implementing a long wavelength cutoff of 4450 cyc/m and short wavelength cutoff of 1520 cyc/m. The map has successfully identified anomalous subsurface structures and emphasized their locations within the region.

2.3. Analytic signal (AS)

The analytic signal (AS) processing technique was employed as it combines both amplitude and phase information from magnetic anomalies, facilitating the identification of subtle magnetic signatures associated with lithological variations and geological boundaries [34], [40]. The AS technique has proven especially valuable in complex geological terrains where traditional magnetic interpretation methods may be limited by interference effects and varying magnetization directions [2], [33]. The interpretation of magnetic anomalies presents significant challenges due to the complex relationship between observed signals and their geological sources. Magnetic data interpretation is particularly complicated by horizontal displacements of anomalies relative to their sources (skewness), which occurs because geomagnetic field vectors and induced magnetization directions typically deviate from vertical orientations [33], [41].

The AS function, although not a directly measurable physical property, plays a crucial role in geophysical interpretation due to its independence from both the inducing field orientation and the magnetization direction. This unique characteristic ensures that bodies of similar geometry produce identical analytic signal responses. Additionally, the AS peaks are symmetric and are positioned directly above the edges of broader bodies or over the centres of narrower ones, providing valuable spatial information about subsurface structures [42]. AS is given by Equation (6):

$$A(x,y)=\sqrt{\left(\frac{\partial T}{\partial x}\right)^2+\left(\frac{\partial T}{\partial y}\right)^2+\left(\frac{\partial T}{\partial z}\right)^2}\,, \tag{6}$$

where: T is the observed field at x and y.

AS technique serves as a reliable tool for estimating the depth of magnetic sources, especially under the assumption of vertical contacts. Utilizing a straightforward amplitude half-width approach, this method achieves depth estimations with a typical accuracy of around 70%. A notable strength of the AS technique is its capacity to by-pass the challenges often associated with conventional reduction-to-pole methods, which are hindered by uncertainties arising from the influence of natural remanent magnetization on the overall magnetization of the source. This capability makes the AS method a robust alternative for magnetic data interpretation, even in complex geological settings [2], [43]. Figure 7 illustrates the outcomes of the Analytic Signal (AS) computations, confirming its utility in scenarios where the magnetic properties of subsurface structures are either complex or insufficiently characterized.

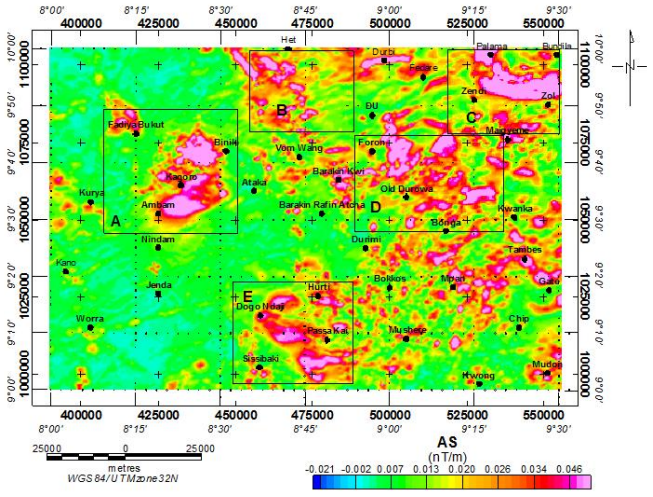

Figure 7. AS map of the study area, highlighting five strategic windows (A, B, C, D, E) selected at locations of suspected subsurface anomalies with potential mineralization

Rather than relying on absolute magnetic intensities, the AS technique emphasizes the anomaly's geometry, making it a robust and adaptable method for interpreting magnetic data. The ability of the AS method to effectively delineate potential mineralized subsurface geological structures, as further corroborated by Phase Symmetry (PS) analysis results, guided the selection of specific data windows (A, B, C, D, E) at key locations for additional processing. Subsequently, Euler Deconvolution (ED) and 3D magnetic data inversion were applied to these windows, enhancing the resolution and clarity of the final interpretations.

2.4. Phase symmetry (PS) analysis

Phase symmetry is closely associated with the principle of phase congruency (PC), which quantifies the alignment of phase across multiple frequency components. Phase congruency occurs when various frequency components within a signal exhibit similar phase values, indicating a state of phase alignment. In regions of symmetry within an image or signal, the local phase remains consistent across different scales, resulting in elevated phase congruency levels.

The fundamental concept underlying phase symmetry analysis is mathematically defined by a series of key equations [44], starting with signal representation.

A signal $I(x)$ can be broken down in terms of its local amplitude $A(x)$ and local phase $\phi(x)$ using the analytic signal:

$$I(x)=A(x)\cos\left(\phi(x)\right). \tag{7}$$

Phase congruency $PC(x)$ at a point x can be calculated using:

$$PC(x)=\frac{\left|\sum_n W_n\sin\left(\phi_n(x)-\phi_0(x)\right)\right|}{\left(\sum_n W_n\left(\phi_n(x)-\phi_0(x)\right)\right)-\sum_n W_n} \tag{8}$$

where: $\phi_n(x)$ is represents the phase at scale n; W_n is a weighing function based on the amplitude; $\phi_0(x)$ is the reference phase.

Phase symmetry $PS(x)$ is calculated as a normalized measure of phase congruency, incorporating contributions from both positive and negative symmetries. It is defined as:

$$PS(x)=\frac{PC_+(x)+PC_-(x)}{2} \tag{9}$$

where: $PC_+(x)$ and $PC_-(x)$ correspond to the phase congruency values for positive and negative symmetries, respectively.

In summary, the phase congruency and phase symmetry measures describe how local phase information can be used to identify structural features within a signal. These parameters provide illumination- and contrast-invariant representations, making them highly effective for feature detection and image analysis.

The computed PS results are presented in Figure 8, while Figure 9 illustrates the outcomes for phase congruency.

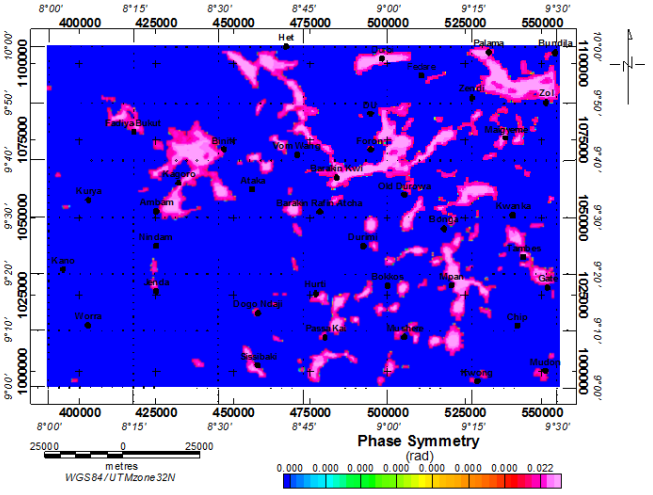

Figure 8. PS analysis of magnetic anomalies in the study area

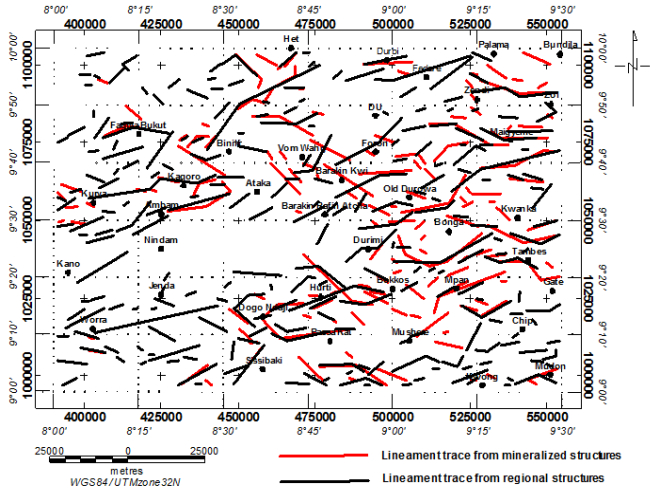

Figure 9. Lineament map from Phase Congruency showing the various subsurface trends within the region

2.5. Tilt derivative (TDR)

The TDR technique is instrumental in accentuating shallow features within geophysical datasets and mapping the boundaries of subsurface structures. This approach excels at identifying subtle anomalies and defining the edges of geological bodies. TDR is mathematically defined as the arctangent of the ratio of the vertical gradient to the horizontal gradient of a potential field. This dimensionless parameter reflects the angle formed between the total gradient vector and the horizontal plane, providing a robust tool for structural delineation [2], [45], [46]. TDR result is displayed in Figure 10.

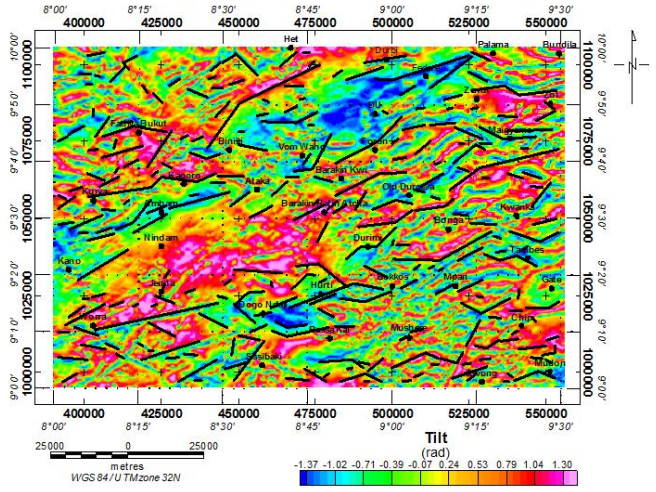

Figure 10. TDR map of the study area

2.6. Euler deconvolution (ED)

ED was utilized to analyze the residual magnetic data, providing insights into the depths and spatial positions of magnetic sources responsible for the observed anomalies. This approach, based on the second vertical derivative of the magnetic field, enabled the precise characterization and mapping of distinct magnetic sources such as faults, dykes, and mineralized zones.

The generalized 3D form of Euler's equation is expressed as Equation (10) [47], [48], [49]:

$$x\frac{\partial T}{\partial x}+y\frac{\partial T}{\partial y}+z\frac{\partial T}{\partial z}+\eta T=x_0\frac{\partial T}{\partial x}+y_0\frac{\partial T}{\partial y}+z_0\frac{\partial T}{\partial z}+\eta b\,, \quad (10)$$

where: x, y, z are coordinates of a measuring point; x_0, y_0, z_0 are coordinates of the source location whose total field is detected at x, y, and z; b is a base level; η is a structural index (SI).

The SI represents an exponential factor that correlates with the rate of field decay over distance for a source with a specific geometry. The value of the SI is contingent upon the type of source body under investigation [48]. For instance, $\eta = 0$ denotes a contact, $\eta = 1$ signifies the top of a vertical dyke or the edge of a sill, $\eta = 2$ corresponds to the center of a horizontal or vertical cylinder, and $\eta = 3$ represents the center of a magnetic sphere or dipole [37], [47]. The implementation of Euler deconvolution is depicted in Figure 11 for a structural index of 1. Geosoft Oasis Montaj software [50] was used in the implementation of these concepts.

2.7. Euler deconvolution (ED)

The processed magnetic data were utilized to develop three-dimensional (3D) geological models, enabling the visualization and interpretation of subsurface structures associated with mineralization. Incorporating magnetic susceptibility contrasts facilitated the characterization of geological features and the delineation of potential mineralized zones, providing insights into the structural extent and spatial distribution of anomalies. The 3D modeling results are presented in Figure 12.

Pilkington [51] employed the Cauchy norm, as outlined by Sacchi and Ulrych [52], to tackle the 3D magnetic inversion problem. This method emphasizes the generation of sparse models by minimizing the number of non-zero parameters required to fit the observed data. Unlike constrained inversion techniques, which integrate explicit geological information such as drill hole data to guide the modeling process, Pilkington's approach is classified as geologically unconstrained [2]. This unconstrained method relies exclusively on magnetic data and mathematical algorithms, making it especially useful in scenarios where geological constraints are unavailable or when an unbiased interpretation of the magnetic anomalies is necessary. However, the lack of geological constraints may result in solutions that, while mathematically sound, might not fully align with known geological structures or properties in some cases.

3. Results and discussion

A direct correlation exists between geological complexities of a region and increased potential for mineral deposits within the region. The varied rock types, from magnetic-rich amphibolite and BIFs to relatively non-magnetic quartzite and schist, coupled with the structural complexity of the region, produced a diverse range of magnetic signatures that we utilized to delineate potential mineralization structures and zones in the study area. The structural geology of northern Nigeria's basement complex has been significantly shaped by extensive crustal deformation (Figure 2). This tectonic activity created numerous conduits and channels, facilitating the migration of mineralized solutions and magmatic intrusions throughout the rock formations.

As a consequence of these intricate geological events, the region has become a repository for diverse mineral deposits. The area boasts an impressive array of economically valuable resources, as illustrated in the mineral distribution map (Figure 3). These include metallic minerals (tin, iron ore, columbite, tantalite, wolframite, and beryl), industrial minerals

(clay, kaolin/kaolinitic clay, mica, and talc), and gemstones (garnet and tourmaline). This remarkable mineral endowment has been well-documented in geological studies [53], [54] highlighting the region's significance as a mineral-rich terrain with substantial economic potential. Significant concentrations of columbite and tantalite minerals are noticed within the study area. At the northern locations of Rafin Bawa, Fedare, Zendi and Wang, these minerals are traced to the younger granite complex of the region. Similar existence is noticed at the central (Dorowa Tsofo) and southern (Sissibaki) locations of the younger granite formation. The Precambrian basement with migmatite gneiss complex at the western regions of Kurya, Antan and Unguwar Kwasea locations, also hold significant record of these minerals.

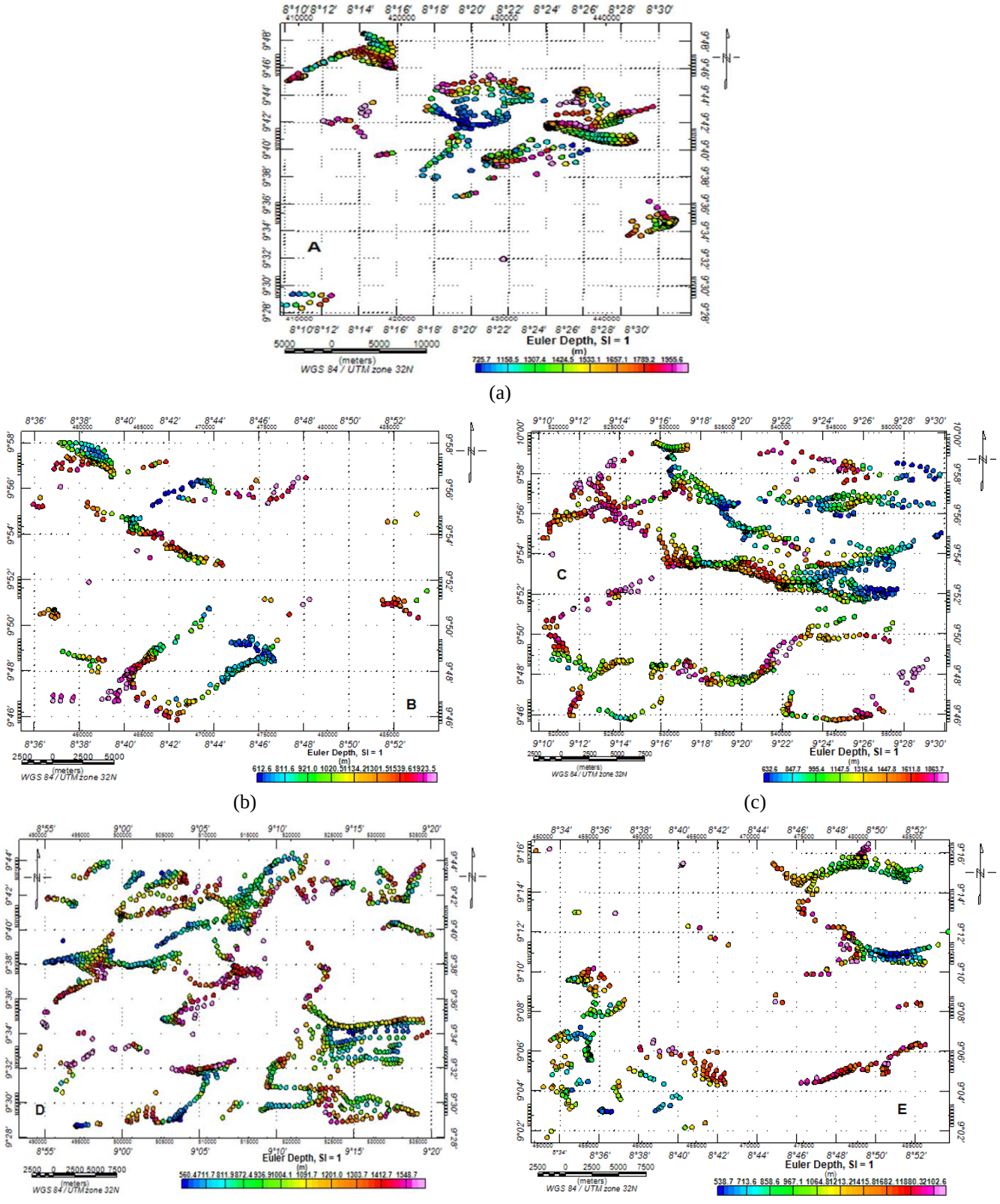

(a)

(b)

(c)

(d)

(e)

Figure 11. Euler depths solution for Windows A, B, C, D and E

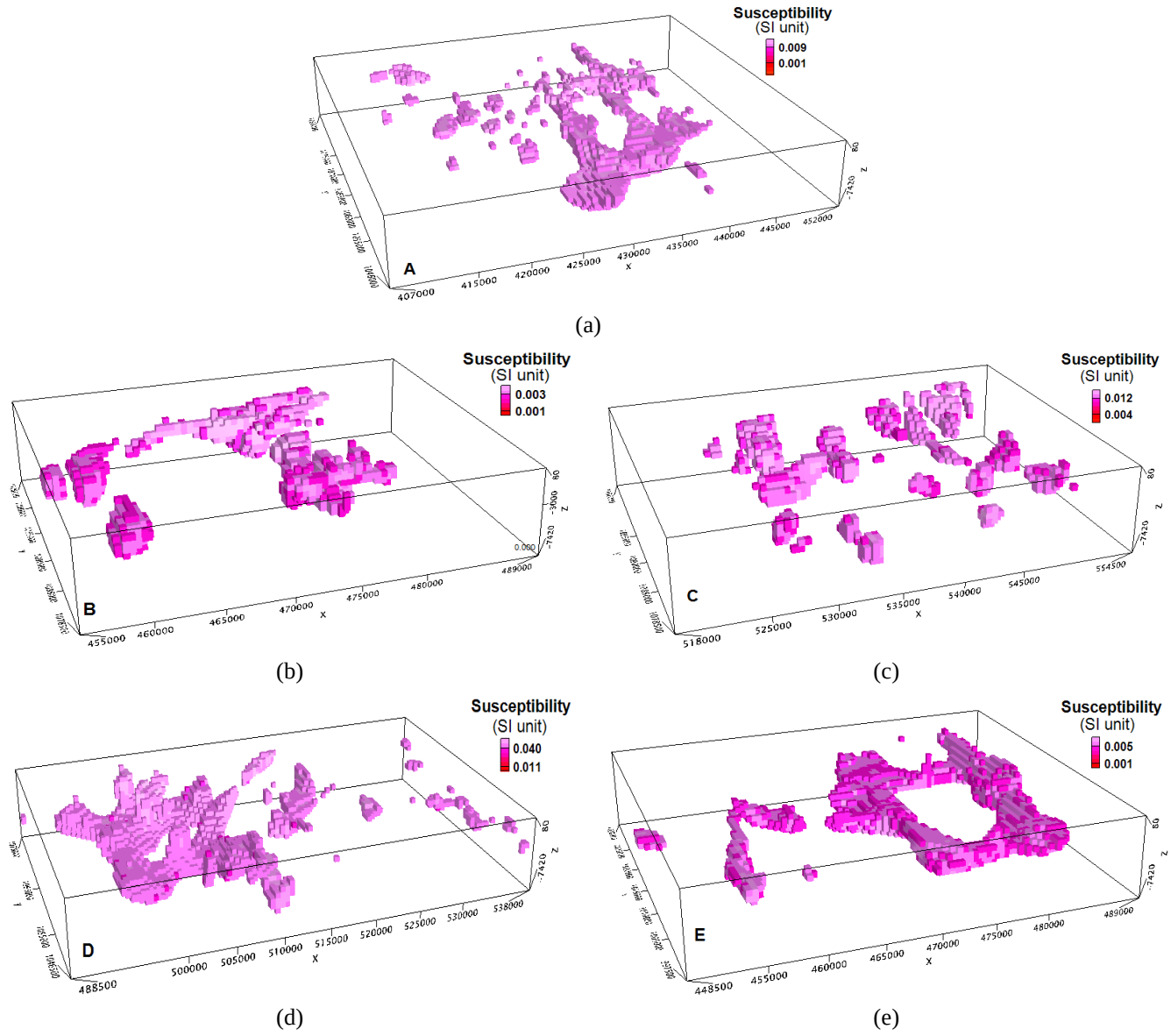

Figure 12. 3D magnetic inversion result for Windows A, B, C, D and E with r.m.s. error of 0.0001 nT

While tourmaline dominace is noted at the SW location of Ungwan Bahagn and Jenda towns, kaolin and kaolinitic clay dominates the northern and central towns of Foron, Ama, Barakin Rafin, and Fedare. These locations are on the granite and granite porphyry, and biotite granite of the Precambrian basement (Figure 2). Porphyritic granite complexes played vital roles in hosting the mineralized structures in the study area. Other minerals with significant presence (example, talc), are traced to the basalt's formation.

The residual magnetic anomaly map of the Kaduna-Nasarawa region (Figure 4) exhibits a significant range of magnetic intensities, varying from -115 to 91 nT. This broad range of values reflects the complex geology of the area and suggests the presence of diverse lithological units with varying magnetic susceptibilities. Observed magnetic contrasts are attributed to several geological factors that indicate potential zones of mineralization. The strongly positive magnetic anomalies (50-91 nT) correspond to the mafic rock body of basalt (Nindam location) and the felsic to intermediate Migmatite rocks of the Jenda, Chip, Zol and Kagoro locations. They potentially represent metamorphosed volcanic rocks or intrusive complexes with particular significance to host the mineralization in the region. The elevated magnetic responses in these areas suggest the presence of deep-seated structures that may have facilitated mineral emplacement during the Pan-African orogeny.

Magnetite-rich banded iron formations (BIFs), which are common in the Precambrian terrain suggests potential for high-grade iron ore deposits in the study area. Moderate positive anomalies (0-50 nT) as seen at Ataka, Bokkos and Kano areas likely reflect amphibolite units within the migmatite-gneiss complex and also ferruginous quartzite, which may host stratabound iron deposits. Low-amplitude negative anomalies (-50 to 0 nT) may indicate granitic intrusions of the Older Granite suite, typically characterized by lower magnetic susceptibilities. Significant occurrences of ancient granite intrusions are observed within the crystalline basement complex of Nigeria, exhibiting diverse directional trends [3]. The Fedare, Du, Vom Wang, Ambam and Dogo Ndaji areas exhibits lower magnetic intensities (-110 to -10 nT), and locates mostly on the biotite granite. These zones are associated with the mica-rich biotite schists, kaolinitic clay deposits, and tourmaline-bearing pegmatites of the region. The moderate – lower magnetic signatures at these locations may indicate

zones of hydrothermal alterations, where primary magnetic minerals have been partially altered to less magnetic phases. These zones show correlation with kaolin deposits, talc occurrences (possibly indicating ultramafic protoliths), columbite and clay-rich weathering profiles.

The SPI result (Figure 5) further confirms the locations of identified subsurface sources and provides depth information to the sources. Our initial observation confirms the locations with suspected mineralized structures at the N, north-central, E and SE regions (Vom Wang, Barkin Rafin, Barakin Kwi, Mpan, Bokkos and Mushere locations) with shallow depths (350-470 m). Intermediate depths (500-720 m) are also confirmed for intermediate sources identified from the other techniques at Zendi, Zol, Du, Barakin Rafin Atcha, Durimi Passa Kai and Chip locations. These are regions with identified mineralized structures with hosting potentials for kaolin, clay, niobium, columbite, beryl, tantalite minerals and Tin ores. Near-surface metamorphic rocks often associates with clay and kaolin deposits and the shallow sources could represent weathered zones containing secondary mineralization. Shallow intrusive bodies, particularly pegmatite, could host rare-metal mineralization [18].

The application of the frequency domain filter that effectively isolates magnetic anomalies within specified wavelength ranges enabled the separation of geological features at varying depths and scale (Figure 6). Cut-off wavelengths were chosen based on the estimated depths of key geological features [58]. The high frequency components of the filtered data reveal near-surface geological features representing weathered zones potentially hosting kaolin in the central, western and southern regions (Ambam, Kagoro, Arna, Barakin Rafin, FOron and Fedare locations), and clay deposits at the Het, Mushere and Nasarawa locations. The near-surface geological features represent surficial expressions of mineralized structures [59]. Some linear features are also observed at the SW, W and NW regions. These are likely representative of shallow shear zones or weathered fault traces as earlier revealed by other techniques. They also show strong correlations with weathered zones which are typically enriched in secondary minerals. The deep sources (low-pass band) or low-frequency components hints on deep-seated intrusive bodies and large-scale features (basement configuration and deep magmatic centers). We recommend the regions where anomalies are mapped across multiple frequency bands as high priority targets for further mineral exploration. We also note that the coincidence of shallow and deep features may also indicate significant mineralization as observed in the SE and N regions.

The analytic signal results (Figure 7) also delineates the edges of magnetic sources, regardless of the ambient magnetic field direction and source magnetization [56]. Several distinctive features are observed in the AS map which points at possible mineralization structures in the KNPS. High amplitude anomalies ranging from 0.04 to 0.05 nT/m are noticeable mostly at the NE, NW, S, and SE regions. These anomalies are traced to the Basalt formation in the NE, Biotite granites in the N and NE, granite gneiss and migmatite formations in the S. They appear concentrated along geological contacts and structural boundaries as could be seen on the geologic and lineament maps, and could be associated with the mineralization in the region. The background values (generally below 0.13 nT/m) observed at the SW, parts of NW and in-between the high amplitude anomalies in the eastern region represent areas of relatively homogeneous lithology which may mask deeper sources due to the AS sensitivity to shallow features. The high amplitude zones (>0.03 nT/m) correlates strongly with magnetite-rich metamorphic rocks hosting garnet deposits (Mineral map – Kwi location). A strong correlation is also observed with the mafic intrusions at the NE and SW regions and they may be related to the columbite – tantalite mineralization at these locations. The moderate amplitude zones (0.015-0.03 nT/m) represents migmatitic gneiss with variable magnetic mineral content and are also of the metasedimentary units hosting mica and kaolin deposits. The low amplitude zones (<0.014 nT/m) holds potential for rare-metal pegmatites and also indicates weathered zones favorable for clay mineral formation (observed at Het location in the north). Similar observations were documented by Omotunde et al. [57] at a location of similar geological setup. The columbite – tantalite deposits at the NE and SW regions are associated within the moderate AS amplitudes (0.014-0.03 nT/m) whereas the rare-metal pegmatites are characterized by low AS amplitudes (<0.01 nT/m). The clay and kaolin deposits (central and southern regions) are found in weathered profiles over moderate amplitude sources and also associates with broad, low-amplitude AS zones in the NW and SE regions of the study area.

The pattern of anomalies observed in the phase symmetry (PS) results (Figure 8) suggest major subsurface intrusions. Strong continuous PS highs (northern region) represent major shear zones or faults as confirmed in the geologic map and earlier analysis. These features are significant as they often control the emplacement of rare-metal pegmatite containing columbite, tantalite and wolframite [60]. The complex, mottled textures of the PS output at the northern (Vom Wang, Foron, Fedare) and SE (Hurti, Bokkos, Bonca) indicate intense deformation or alteration in the region. These textural variations are crucial for identifying potential hosts for pegmatite mineralization [61]. Columbite, tantalite and wolframite occurences at the S (Sissibaki) and NE (Fedare) regions show strong correlation with the edges of the rounded PS anomalies. Areas of low PS response at Kurya and Chip locations corresponds to the clay and kaolin deposits at the locations. These locations are traced to the migmatite formation. Low PS response at the SW region also corresponds to the tourmaline mineral presence at the location. These associations reflect the pegmatite and metamorphic origins of these minerals [18]. We suggest zones where the PS features are pronounced and with notable intersections, as priority targets, especially areas with complex PS textures.

Deeper depths (750-2000 m) have been obtained mostly at regions unsuspecting of mineralized subsurface intruded structures or suspected deep sources. This assertion is supported by results from the analytic signal, Butterworth bandpass and the PS evaluations. We believe these regions could host significant mineralize structures but at deeper depths, hence the weak anomaly signals from the near-surface evaluations. The deep sources are indications of basement structures, major shear zones and deep-seated granitic intrusions at the locations. The shallow depths (250-500 m) solutions show strong association with clay and kaolinitic deposits in the SE and north-central regions. These industrial minerals are typically found in weathered zones of the basement complex.

There are also some correlation of the shallow depths (300-600 m) with surficial columbite – tantalite placer deposits at parts of the N, W, and S regions. In some instance, the deeper depth solutions (>1200 m) may indicate potential source regions for mineralizing fluids. We advise focus on areas with shallow SPI solutions for industrial minerals, weathered zones and above intermediate-depth magnetic sources for high-quality kaolin deposits [62], and areas where intermediate-depth solutions (700-1200 m) intersecting with known structural controls, for rare-metal mineralization.

There are also some secondary NW-SE trending structures (Fadiya Bukut, Hurti and Malgyme regions) and E-W trending discontinuities scattered all over the study area. The complex overlapping patterns in the features suggest multiple intrusive events and the sharp transition contact zones observed in the various amplitudes indicates lithological boundaries [45]. These trends have been corroborated by results from the phase congruency (PC) evaluations, superimposed on the tilt derivative map. Consequently, areas of high PC density at the NE, NW, SE, and southern regions of the study area indicates intense deformation. This is also evident in the geology map of the region. Zones of low PC density suggest more homogeneous lithology as observed at the SW region of the study area.

Integration of the tilt derivative with the PC analysis (Figure 9) show PC edges coinciding with the sharp tilt gradients (0.5-1.5 rad) evident at Kurya, Nindam, Passa Kai, Foron, Barakin Rafin and other locations. These interactions confirms some mapped structures on the geology map and also reveals subtle structures not apparent in the magnetic anomaly data. The high frequency, short-wavelength anomalies in the tilt derivative result (parts of NE, N, and SE regions) corresponds to near-surface metamorphic rocks in the KNPS and may indicate zones of hydrothermal alteration. These are potential areas for clay and kaolin deposits. This deduction is also observed on the mineral map of the area. The low frequency, long-wavelength features (parts of SW and NE regions) points to deeper and more extensive geological bodies (also observed on the geology map), and may represent basement structures or major intrusive complexes within the KNPS. Columbite – tantalite deposits are associated with sharp PC edges in the moderate magnetic anomaly zones, preferentially occurring along NE-SW trending PC features.

The intersections of the PC trends in Figure 9, indicates favorable structural settings for columbite-tantalite deposits. We interpret the broad, diffuse PC features at regions with concentrated PC and magnetic lows (S and NE regions) as been associated with the clay and kaolin deposits. Sharp tilt derivative gradients (southern Jenda, Mushere and Kwi) also indicates lithological contacts [55] and could be responsible for the mica mineralization along the pegmatite margins, clay deposits in the weathered contact zone as well as the garnet presence in the metamorphic aureoles.

We present results from the Tilt derivative (Figure 10) with superimposed trends from phase congruency (PC) computations. The superpositioning was performed for ease of direct comparisons. The patterns are consistently highlighted in both analyses, despite being derived through independent methods. Figure 10 presents the lineament map of the study area, exclusively illustrating the diverse subsurface trends across the region. Two unique trending were identified. While the general trends were captured from the magnetic anomalies in the region, trending of the mineralized structures have also been captured with some interacting with the general trends of the study area. The tilt derivative map reveals several significant features in the study area. Primary NE-SW lineaments represent major shear zones related to the Pan-African orogeny and are associated with columbite-tantalite mineralization. Predominant linear features are observed at Jenda, Ambam, Dogo Ndaji – Hurti, and Foron regions.

Euler depth solutions from magnetic anomalies windows (A, B, C, D, and E) are shown in Figure 11. The Euler solutions reveal a multi-level distribution of magnetic sources. With our primary focus on delineating possible presence of dykes or sill structures (SI = 1) in the study area, we interpret the clustering of solutions in the windows as indicative of dyke or sill structures or edges of these structures hosting minerals within the considered windows. The shallow sources (<500 m) corresponds to the weathered zones hosting clay, niobium, beryl, kaolin deposits (Windows B, C, D, and E) and shallow pegmatite bodies containing tourmaline and mica (Window C and E). These findings align with the work of Oruc and Salim [65], who noted similar depth distributions in the Precambrian terrains. We interpret the deeper sources (>500 m) as deep-seated intrusive bodies and possible ultramafic sources of mineralization (example, talc – NW region of Gidan Tagwai) and SE region (Mushere). Analysis of the spatial distribution of Euler solutions reveals several key patterns with linear clusters predominantly trending NE-SW (Windows A, B, D, and E). These are interpreted as dyke swarms or shear zones. The circular and rounded clusters characterized by concentric arrangements of solutions with elongations in the E-W, NE-SW trending (Windows A, C, D, and E) represents multiple structural indices and suggest complex geometry in the study area. This assertion is confirmed in the geology map and the 3D magnetic inversion results. These clusters may likely represent granitic intrusions hosting rare-metal pegmatite and metamorphic domes with potential for garnet and mica.

Insights into the structural framework has also been provided by the lineation of the Euler solutions. Linear alignments of solutions may represent fault systems and multiple depth ranges suggest deep rooted structures. These are key controls on mineralization particularly for the wolframite and tourmaline bearing pegmatite (Windows E and C), kaolin, and tin ore (Window B, D, and E). Similar structural controls were identified by Amigun et al. [66] and Abraham et al. [67]. Intrusive complexes characterized by clustered solutions with depths >600 m (Windows A, B, C, D, E), are also potential source regions for rare-metal pegmatite and hydrothermal mineralization. The Euler solutions realized have provided depth constraints to the magnetic lineaments identified in the tilt derivative map as some clusters of the solutions correlate with zones of high magnetic gradients and intersections of major structural features.

The 3D inversion results (Figure 12) reveal a complex distribution of magnetic susceptibility within the study area. The final representative structures realized in the 3D windows (Figure 12) were achieved by clipping susceptibilities of various units to leave-out the anomalous units. The models provide insights into the vertical distribution of potential mineralization. Suspected structures at Fadiya Bukut (Win-

dow A) at depths (350-1220 m) traces to possible subsurface structures hosting niobium, columbite, and tantalite minerals at the location. A major subsurface structure is mapped SE in Window A (eastern regions of Ambam – Anta – Ataka). This structure is significant in size and depths (1000-2500 m). This could represent deep-seated mineralized structure hosting the columbite, molybdenite and tin ores at the locations. Window B reveals intruded subsurface structures (200-1600 m) with possible mineralization of columbite, monazite, tantalite and clay. At the Palama – Zendi – Zol locations (Window C), significant intrusives have been noticed (170-200 m). These could represent possible kaolin/kaolinitic clay and tourmaline mineral hosts within the subsurface. Clay, kaolin and mica-rich pegmatites recorded at shallow mineralization in the windows are consistent with weathering – controlled deposits described by Salawu et al. [63].

A significant interconnected structure (400-3200 m) is captured in Window D and traces largely to the older basalts, porphyritic granite, biotite granite and the migmatite complexes. This is indicative of a significant subsurface mineralized structure at this location yet discovered, notwithstanding traces of tin ores noted at the Old Durowa location. Deep features (>1200 m) are characteristic of large, cohesive bodies of elevated susceptibility. With susceptibility values ranging from 0.02 to 0.08 SI, a greater percentage of these features are interpreted as major basement structures. Intermediate to deeper depth targets in Window E (150-3000 m) may be responsible for the columbite – tantalite, wolframite, garnet, feldspar, kaolin/kaolinitic clay, beryl, tin/niobium and clay minerals recorded at the location. These are analogous to deep mineral systems described by Denith et al. [64].

4. Conclusions

The integrated analysis of high-resolution aeromagnetic data over the Kaduna-Nasarawa Precambrian Shield (KNPS) has provided significant insights into the region's mineral potential and structural framework. Through the application of multiple magnetic data enhancement techniques, our study has successfully delineated a complex network of mineralized structures at various depths, offering a comprehensive understanding of the region's mineral resources. The correlation between magnetic signatures and known mineral occurrences has validated our methodological approach while simultaneously revealing new prospective zones for exploration.

The residual magnetic anomaly patterns, ranging from -115 to 91 nT, reflect the diverse lithological units within the study area, with strongly positive anomalies corresponding to mafic rock bodies and intermediate values indicating potential rare-metal pegmatite. The integration of tilt derivatives with phase congruency analysis has proven particularly effective in identifying subtle structural features not apparent in the magnetic data, especially along the predominant NE-SW trending lineaments that control mineral emplacement in the region. These structural controls, further confirmed by analytic signal computations and 3D magnetic inversion modeling, demonstrate the critical relationship between tectonic activity and mineralization processes in the Nigerian Basement Complex.

Our depth analysis, combining source parameter imaging and Euler deconvolution, has established a clear vertical zonation of mineral deposits. Shallow sources (250-500 m) consistently correlate with industrial minerals, particularly clay and kaolinitic deposits, while intermediate depths (500-720 m) host significant rare-metal pegmatite containing columbite, tantalite, and wolframite. The identification of deeper structures (>1200 m) suggests the presence of potential source regions for mineralizing fluids, offering new targets for deep exploration. The coincidence of anomalies across multiple frequency bands has highlighted priority exploration targets, particularly in areas where shallow and deep magnetic features intersect. The success of this integrated approach in mapping both known mineral occurrences and identifying new prospective zones demonstrates its efficacy for mineral exploration in complex Precambrian terrains. However, we recommend ground-truthing of the identified targets through detailed geological mapping and geochemical sampling to validate our interpretations.

Our study has contributes to the geological understanding of the Kaduna-Nasarawa Precambrian Shield and also provides a methodological framework for systematic mineral exploration in similar geological settings. The economic implications of our findings are significant, offering valuable guidance for targeted exploration efforts in the region. As Nigeria seeks to diversify its economy through the development of its solid mineral resources, the approach and results presented here represent a valuable contribution to achieving this national objective.

Author contributions

Conceptualization: EA, MA; Data curation: EA, ME; Formal analysis: AU, EA, II; Investigation: EA, AU; Methodology: EA, AU, MA, ME; Project administration: EA; Resources: EA, II, ME; Software: EA, II; Supervision: EA, ME; Validation: EA, AU; Visualization: EA; Writing – original draft: EA, MA, AU; Writing – review & editing: EA, ME, AU, II; All authors have read and agreed to the published version of the manuscript.

Funding

This research did not receive any specific grant from funding agencies in the public, commercial, or not-for-profit sectors.

Acknowledgements

To all the anonymous reviewers and the editor, we say thank you for your comments and contributions which improved the quality of our submission.

Conflicts of interests

The authors declare no conflict of interest.

Data availability statement

The original contributions presented in the study are included in the article, further inquiries can be directed to the corresponding author.

References

[1] Subari, Erlangga, B.D., Maryani, E., & Arifin, D.N. (2021). Potential utilization of quartz sand and kaolin from tin mine tailings for whiteware. *Mining of Mineral Deposits*, *15*(3), 1-6. https://doi.org/10.33271/mining15.03.001

[2] Abraham, E.M., Uwaezuoke, A.E., & Usman, A.O. (2024). Geophysical investigation of subsurface mineral potentials in North-Central Nigeria: Implications for sustainable mining and development. *Geomechanics and Geophysics for Geo-Energy and Geo-Resources*, *10*(1), 192. https://doi.org/10.1007/s40948-024-00913-3

[3] Abraham, E., Usman, A., Chima, K., Azuoko, G., & Ikeazota, I. (2024). Magnetic inversion modeling of subsurface geologic structures for mineral deposits mapping in southeastern Nigeria. *Bulletin of the Mineral Research and Exploration*, *173*(173), 85-105 https://doi.org/10.19111/bulletinofmre.1267876

[4] Usman, A.O., Abraham, E.M., Ezeh, C.C., Azuoko, G., Augustine, I.C., Chima, J.C., & Obinna, C.A. (2024). Structural modelling of subsurface geologic structures in Anambra and adjoining Bida Basins using aeromagnetic data: Implications for mineral explorations. *Kuwait Journal of Science*, *52*, 100307. https://doi.org/10.1016/j.kjs.2024.100307

[5] Abraham, E.M., Onwe, M.R., Usman, A.O., Gwazah, C.A., & Uchenna, M.E. (2022). Mapping of mineral deposits within granitic rocks by aeromagnetic data-a case study from Northern Nigeria. *Arabian Journal of Geosciences*, *15*, 1656 https://doi.org/10.1007/s12517-022-10947-0

[6] Leão-Santos, M., Li, Y., & Moraes, R. (2015). Application of 3D-magnetic amplitude inversion, to iron oxidecopper-gold deposits, at low magnetic latitudes: A case-study from Carajas Mineral Province, Brazil. *Geophysics*, *80*(2), B13-B22. https://doi.org/10.1190/geo2014-0082.1

[7] Obaje, N.G. (2009). The Benue Trough. Geology and Mineral Resources of Nigeria. Springer. 57. SBN 3-540-92684-4. https://doi.org/10.1007/978-3-540-92685-6

[8] NGSA (2022). Nigeria Geological Survey Agency - Geological Map of Nigeria.

[9] Ogezi, A.E. (1977). Geochemistry and Mineralization Potential of the Basement Complex Rocks of the Jos-Bukuru Complex, Nigeria. *Nigerian Mining Journal*, *4*(2), 45-53.

[10] Rahaman, M.A. (1988). Recent advances in the study of the Basement Complex of Nigeria. *Precambrian Geology of Nigeria, Geological Survey of Nigeria*, 11-43.

[11] McCurry, P. (1976). The Geology of the Precambrian to Lower Paleozoic Rocks of Northern Nigeria: A Review. In C. A. Kogbe (Ed.), Geology of Nigeria (pp. 15-39). Elizabethan Publishing Company.

[12] Telford, W.M., Geldart, L.P., & Sheriff, R.E. (1990). Applied Geophysics (2nd ed.). Cambridge University Press. https://doi.org/10.1017/CBO9781139167932

[13] Woakes, M., Ajibade, A.C., & Rahaman, M.A. (1987). Some metallogenic features of the Nigerian basement. *Journal of African Earth Sciences*, *6*(5), 655-664. https://doi.org/10.1016/0899-5362(87)90004-2

[14] Ugwu, S.A., Nwankwoala, H.O., & Agada, E.A. (2017). Structural Analysis and Aeromagnetic Interpretation of Spot Image for Mineral Potentials in the Jos-Plateau Area, North Central Nigeria. *African Journal of Basic & Applied Sciences*, *9*(5), 303-310, https://doi.org/10.5829/idosi.ajbas.2017.303.310

[15] Ennih, N., & Liégeois, J. (2008). The boundaries of the West African craton, with special reference to the basement of the Moroccan metacratonic Anti-Atlas belt. *Geological Society, London, Special Publications*, *297*, 1-17. https://doi.org/10.1144/SP297.1

[16] Caby, R. (2003). Terrane assembly and geodynamic evolution of central-western Hoggar: a synthesis. *Journal of African Earth Sciences*, *37*(3-4), 133-159. https://doi.org/10.1016/j.jafrearsci.2003.05.003

[17] Dada, S.S. (2006). Proterozoic evolution of Nigeria. The Basement Complex of Nigeria and its mineral resources (A Tribute to Prof. M. A. O. Rahaman). Akin Jinad & Co. Ibadan, 29-44. https://www.scirp.org/reference/referencespapers?referenceid=1425168

[18] Garba, I. (2003). Geochemical discrimination of newly discovered rare-metal bearing and barren pegmatites in the Pan-African (600 ± 150 Ma) basement of northern Nigeria. *Applied Earth Science*, *112*(3), 287-292. https://doi.org/10.1179/037174503225011270

[19] Adepoju, M. (2022). Structural control of ore mineralization in the southeastern margin of western Nigeria basement. *International Journal of Geosciences*, *13*, 547-556. https://doi.org/10.4236/ijg.2022.137029

[20] Elueze, A.A. (1982). Geochemistry of the Ilesha granite-gneiss in the basement complex of southwestern Nigeria. *Precambrian Research*, *19*(2), 167-177. https://doi.org/10.1016/0301-9268(82)90057-2

[21] Ekwueme, B.N., & Kroner, A. (2006). Single zircon ages of migmatites in the Obudu Plateau, Cross River State, SE Nigeria. *Journal of African Earth Sciences*, *44*(4-5), 403-407. https://doi.org/10.1016/j.jafrearsci.2005.11.013

[22] Adekoya, J.A. (1998). The geology and geochemistry of the Maru Banded Iron-Formation, northwestern Nigeria. *Journal of African Earth Sciences*, *27*(2), 241-257. https://doi.org/10.1016/S0899-5362(98)00059-1

[23] Oyinloye, A.O. (2011). Geology and geotectonic setting of the basement complex rocks in south western Nigeria: Implications on provenance and evolution. *Earth and Environmental Sciences*, 98-117. https://doi.org/10.5772/26990

[24] Okonkwo, C.T., & Folorunso, I.O. (2013). Petrochemistry and geotectonic setting of granitic rocks in Aderan area, SW Nigeria. *Journal of Geography and Geology*, *5*(1), 30. https://doi.org/10.5539/jgg.v5n1p30

[25] Ajibade, A.C., Woakes, M., & Rahaman, M.A. (1987). Proterozoic Crustal Development in the Pan-African Regime of Nigeria. In Kroner, A., (Ed.), Proterozoic Lithospheric Evolution (pp. 259-271). Washington DC, USA: American Geophysical Union.

[26] Odeyemi, I. (1993). A comparative study of remote sensing images of the structure of the Okemesi fold belt, Nigeria. *ITC Journal*, *1993*(1), 77-81.

[27] Oluyide, P.O. (1988). Structural trends in the Nigerian basement complex. In: Oluyide, P.O., et al. (Eds.), Precambrian Geology of Nigeria. *Geological Survey of Nigeria*, 93-98.

[28] Anifowose, A.Y.B., & Borode, A.M. (2007). Photogeological study of the fold structure in Okemesi area, southwestern Nigeria. *Journal of Mining and Geology*, *43*(2), 125-130. https://doi.org/10.4314/jmg.v43i2.18872

[29] Kinnaird, J.A. (1984). Contrasting styles of Sn-Nb-Ta-Zn mineralization in Nigeria. *Journal of African Earth Sciences*, *2*(2), 81-90. https://doi.org/10.1016/S0731-7247(84)80001-4

[30] Okunlola, O.A., & Ocan, O.O. (2009). Rare Metal (Ta-Sn-Li-Be) Distribution in Precambrian Pegmatites of Keffi Area, Central Nigeria. *Nature and Science*, *7*, 90-99.

[31] Ganguli, S.S., Pal, S.K., & Kumar, S.K.P. (2021). Insights into the crustal architecture from the analysis of gravity and magnetic data across Salem-Attur Shear Zone (SASZ), Southern Granulite Terrane (SGT), India: an evidence of accretional tectonics. *Episodes*, *44*(4), 419 - 422. https://doi.org/10.18814/epiiugs/2020/020095

[32] Abraham E., Itumoh O., Chukwu C., & Onwe R. (2018). Geothermal Energy Reconnaissance of Southeastern Nigeria from Analysis of Aeromagnetic and Gravity Data. *Pure and Applied Geophysics*, *176*: 22-36. https://doi.org/10.1007/s00024-018-2028-1

[33] Nabighian, M.N., Grauch, V.J.S., Hansen, R.O., LaFehr, T.R., Li, Y., Peirce, J.W., & Ruder, M.E. (2005). The historical development of the magnetic method in exploration. *Geophysics*, *za* (6), 33ND-61ND. https://doi.org/10.1190/1.2133784

[34] Rajagopalan, S. (2003). Analytic Signal vs. Reduction to Pole: solutions for low magnetic latitudes. *Exploration Geophysics*, *34*(4), 257-262. https://doi.org/10.1071/EG03257

[35] Jain, S. (1988). Total magnetic field reduction-The pole or equator? a model study. *Canadian Journal of Exploration Geophysics*, *24*(2), 185-192. Retrieved from https://cseg.ca/wp-content/uploads/1988_12_Sudhir_J_magnetic_field_reduction.pdf

[36] Leu, L.K. (1981). Use of reduction-to-the-equator process for magnetic data interpretation. *Geophysics*, *47*, 445.
[37] Thurston, J.B., & Smith, R.S. (1997). Automatic conversion of magnetic data to depth, dip and susceptibility contrast using the SPITM method. *Geophysics*, *62*, 807-813. https://doi.org/10.1190/1.1444190
[38] Proakis, J.G., & Manolakis, D.G. (2007). Digital Signal Processing: Principles, Algorithms, and Applications. Prentice Hall. Pearson.
[39] Oppenheim, A.V., & Schafer, R.W. (2009). Discrete-Time Signal Processing. Pearson Education.
[40] Usman, A.O., Nomeh, J.S., & Abraham, E.M. (2025). Subsurface structural mapping a tool in understanding the Geodynamics of Mineralization within the North?Central Precambrian Basement of Nigeria, using aeromagnetic dataset. *Earth Science Informatics*, *18*, 169. https://doi.org/10.1007/s12145-024-01492-3
[41] Roest, W.R., Verhoef, J., & Pilkington, M. (1992). Magnetic interpretation using the 3D analytic signal. *Geophysics*, *57*(1), 116-125. https://doi.org/10.1190/1.1443174
[42] Cooper, G. & Cowan, D.. (2006). Enhancing potential field data using filters based on the local phase. *Computers and Geosciences*, *32*(10), 1585-1591. https://doi.org/10.1016/j.cageo.2006.02.016
[43] Adebisi, W.A., Folorunso, I.O., Abubakar, H.O., Olatunji, S., & Olaojo, M.O. (2024). Delineating structural features related to hydrothermal alterations for possible mineralization in share area, Kwara State Nigeria using aeromagnetic data. *Indonesian Journal of Earth Sciences*, *4*(2), A1265. https://doi.org/10.52562/injoes.2024.1265
[44] Kovesi, P. (1999). Image Features from Phase Congruency. *Videre: Journal of Computer Vision Research*, *1*(3), 1-26. Retrieved from https://www.cs.rochester.edu/u/brown/Videre/001/articles/v1n3001.pdf
[45] Miller, H.G., & Singh, V. (1994). Potential field tilt-a new concept for location of potential field sources. *Journal of Applied Geophysics*, *32*(2-3), 213-217. https://doi.org/10.1016/0926-9851(94)90022-1
[46] Verduzco, B., Fairhead, J.D., Green, C.M., & Mackenzie, C. (2004). New insights into magnetic derivatives for structural mapping. *The Leading Edge*, *23*(2), 116-119. https://doi.org/10.1190/1.1651454
[47] Reid, A.B., Allsop, J.M., Grauser, H., Millet, A.J., Somerton, I.N. (1990). Magnetic interpretation in 3D using Euler-Deconvolution. *Geophysics*, *55*, 80-91. https://doi.org/10.1190/1.1442774
[48] Whitehead, N., & Musselman, C. (2005). Montaj Gravity/Magnetic interpretation: Processing, analysis, and visualization system, for 3-D inversion of potential field data, for Oasis montaj v6.1. Geosoft Inc. ON, Canada
[49] Thompson, D.T. (1982). Euldph: A new technique, for making computer-assisted, depth- estimates, from magnetic data, *Geophysics*, *47*. pp. 31-37. https://doi.org/10.1190/1.1441278
[50] GEOSOFT (2007). Geosoft Oasis Montaj softeware. Version 8.3
[51] Pilkington, M. (2009). 3D magnetic data-space inversion with sparseness constraints. *Geophysics*, *74*(1) P.L7-L15. https://doi.org/10.1190/1.3026538
[52] Sacchi, M.D., & Ulrych, T.J. (1995). High-resolution velocity gathers and offset space reconstruction: *Geophysics*, *60*, 1169-1177. https://doi.org/10.1190/1.1443845
[53] Megwara, J.U., & Udensi, E.E. (2014). Structural analysis using aeromagnetic data: case study of parts of Southern Bida Basin, Nigeria and the surrounding basement rocks. *Earth science research*, *3*(2), 27. https://doi.org/10.5539/esr.v3n2p27
[54] Dzukogi, A.N.A., & Bello, M.M. (2022). Aeromagnetic Data Analysis and Interpretations to Investigate Solid Mineral Potential in Part of Northwest Nigeria. *African Journal of Advances in Science and Technology Research*, *4*(1), 125-138. Retrieved from https://publications.afropolitanjournals.com/index.php/ajastr/article/view/171
[55] Ajana, O., Udensi, E.E., Momoh, M., Rai, J.K., & Muhammad, S.B., (2014). Spectral Depths Estimate of Subsurface Structures in Parts of Borno Basin, Northeastern Nigeria, using Aeromagnetic Data. *IOSR Journal of Applied Geology and Geophysics*, *2*, 55-60.
[56] Mekonnen, T.K. (2004). Interpretation and Geodatabase of Dykes Using Aeromagnetic Data of Zimbabwe and Mozambique. M.Sc. Thesis, ITC, Delft, 80 p.
[57] Salem, A., Ravat, D., Gamey, T.J., & Ushijima, K. (2002). Analytic signal approach and its applicability in environmental magnetic investigations. *Journal of Applied Geophysics*, *49*(4), 231-244. https://doi.org/10.1016/S0926-9851(02)00125-8
[58] Omotunde, V.B., Olatunji, A.S., & Abdus-Salam, M.O. (2020). Rare Earth Elements Assessment in the Granitoids of Part of Southwestern Nigeria. *European Journal of Environment and Earth Sciences*, *1*(5). http://doi.org/10.24018/ejgeo.2020.1.5.79
[59] Goodenough, K.M., Schilling, J., Jonsson, E., Kalvig, P., Charles, N., Tuduri, J., Deady, E.A., Sadeghi, M., Schiellerup, H., Müller, A., Bertrand, G., Arvanitidis, N., Eliopoulos, D.G., Shaw, R.A., & Thrane, K., Keulen, N. (2016). Europe's Rare Earth Element Resource Potential: An Overview of REE Metallogenetic Provinces and Their Geodynamic Setting. *Ore Geology Reviews*, *72*, 838-856. https://doi.org/10.1016/j.oregeorev.2015.09.019
[60] Aliyu, A., Lawal, K.M., Abubakar, L.Y., Dada, I., & Olayinka, A. (2020). Geomagnetic Studies of Pegmatite Mineralization at Lema and Ndeji North-Central, Nigeria. *Journal of Mining and Geology*, *56*(1), 81-89.
[61] Yunusa, A., Hong, H., Salim, A., Amam, T., Liu, C., Xu, Y., Zuo, X., & Li, Z. (2024). Mineralogical Characterization and Geochemical Signatures of Supergene Kaolinitic Clay Deposits: Insight of Ropp Complex Kaolins, Northcentral Nigeria. *Minerals*, *14*(9), 869. https://doi.org/10.3390/min14090869
[62] Nasuti, Y., & Nasuti, A. (2018). NTilt as an improved enhanced tilt derivative filter for edge detection of potential field anomalies, *Geophysical J. International*, *214*(1), 36-45, https://doi.org/10.1093/gji/ggy117
[63] Oruc, B., & Selim, H.H. (2011). Interpretation of Magnetic Data in the Sinop Area of Mid Black Sea, Turkey, Using Tilt Derivative, Euler Deconvolution and Discrete Wavelet Transform. *Journal of Applied Geophysics*, *74*, 194-204. https://doi.org/10.1016/j.jappgeo.2011.05.007
[64] Amigun, J.O., Sanusi, S.O., & Audu, L. (2022). Geophysical characterisation of rare earth element and gemstone mineralisation in the Ijero-Aramoko pegmatite field, southwestern Nigeria. *Journal of African Earth Sciences*, 104494. https://doi.org/10.1016/j.jafrearsci.2022.104494
[65] Abraham, E.M., Nkitnam, E.E., & Itumoh, O.E. (2020). Integrated geophysical investigation of recent earth tremors in Nigeria using aeromagnetic and gravity data. *Environ Monit Assess*, 192:352 https://doi.org/10.1007/s10661-020-08339-6
[66] Salawu, N.B., Omosanya, K.O.L., Eluwole, A.B., Saleh, A., & Adebiyi, L.S. (2023). Structurally-controlled Gold Mineralization in the Southern Zuru Schist Belt NW Nigeria: Application of Remote Sensing and Geophysical Methods. *Journal of Applied Geophysics*, *211*, 104969. https://doi.org/10.1016/j.jappgeo.2023.104969
[67] Dentith, M., Yuan, H., Johnson, S., Murdie, R., & Piña-Varas, P. (2018). Application of deep-penetrating geophysical methods to mineral exploration: Examples from Western Australia. *Geophysics*, *83*(3), https://doi.org/10.1190/geo2017-0482.1

Сирек металды минералданудың құрылымдық бақылауы: Нигерияның кристалды іргетасындағы экономикалық кен орындарының терең картасын жасау

Э. Абрахам[1*], М. Абду́льфарадж[2], М. Эметере[1], А. Усман[1], И. Икеазота[1]

[1]*Алекс Эквуэме федералды университеті, Икво, Нигерия*
[2]*Абдулазиз университеті, Джидда, Сауд Арабиясы*
[2]*Боуэн университеті, Иво, Нигерия*

**Корреспонденция үшін автор: ema.abraham@funai.edu.ng*

Аңдатпа. Бұл зерттеудің мақсаты минералдық-барлау жұмыстары үшін перспективалы аймақтарды анықтау және Кембрий алдындағы террандар шегінде минералдану процестерін түсінуді тереңдету болып табылады. Жоғары дәлдіктегі аэромагниттік деректер аналитикалық сигналды, көлбеу туынды өрісті, фазалық симметрияны, көз параметрлерін бейнелеуді, Баттеруорттың жолақты сүзуін, магниттік ауытқулардың үш өлшемді инверсиясын және Эйлердің деконволюциясын қоса алғанда, біріктірілген геофизикалық әдістер кешенін қолдану арқылы талданды. Бұл әдістер жер асты құрылымдарын бөліп көрсетуге, олардың кеңістіктік таралуын, пайда болу тереңдігін және пайдалы қазбалардың көріністерімен байланысын анықтауға мүмкіндік берді. Нәтижелер минералды заттардың енгізілуін бақылайтын негізгі сдысу аймақтары мен ақаулы жүйелерге сәйкес келетін солтүстік-шығыс және солтүстік-батыс кеңеюінің сызықтық аймақтарының болуын көрсетті. Таяз бұлақтар (250-500 м) саз сияқты өнеркәсіптік минералдармен байланысты; құрамында сирек кездесетін металл пегматиттері бар аралық тереңдіктер (500-720 м) колумбит-танталит және вольфрамит; ал терең құрылымдар (>1200 м) минералданатын сұйықтықтардың пайда болуының ықтимал аймақтарын көрсетеді. Аналитикалық сигналдың жоғары амплитудалық ауытқулары (0.04-0.05 нТ/м) геологиялық контактілермен және құрылымдық шекаралармен сәйкес келеді, мүмкін минералдану аймақтарын белгілейді. Бұл зерттеу аймақтың жер асты минералданған құрылымдарын зерттеуге бағытталған алғашқы кешенді жұмыс болып табылады. Геофизикалық әдістер кешенін қолдану бұрын көрсетілмеген құрылымдық ерекшеліктерді анықтауға және минералданған аймақтардың тік үздіксіздігін растауға мүмкіндік берді. Жартылай алынған нәтижелер мақсатты геологиялық барлау жұмыстары үшін құнды түсініктер бере отырып және кристалдық іргетас шегінде колумбит-танталит, вольфрамит, каолин және басқа да ойластырылған минералдарды іздеудің дәлірек және үнемді стратегияларын әзірлеуге ықпал ете отырып, экономикалық маңызы бар кен орындарын терең бағдарланған картаға түсіруді қамтамасыз етеді.

Негізгі сөздер: *магниттік деректер, пайдалы қазбаларды барлау, тереңдік, құрылымдық бақылау, тау-кен, кристалдық іргетас.*

Структурный контроль редкометалльной минерализации: глубинное картирование экономических месторождений в кристаллическом фундаменте Нигерии

Э. Абрахам[1*], М. Абду́льфарадж[2], М. Эметере[1], А. Усман[1], И. Икеазота[1]

[1]*Федеральный университет Алекса Эквуэме, Икво, Нигерия*
[2]*Университет Абдулазиза, Джидда, Саудовская Аравия*
[2]*Университет Боуэн, Иво, Нигерия*

**Автор для корреспонденции: ema.abraham@funai.edu.ng*

Аннотация. Цель данного исследования заключается в выявлении перспективных зон для минералого-разведочных работ и углублении понимания процессов минерализации в пределах докембрийских террейнов. Высокоточные аэромагнитные данные были проанализированы с использованием комплекса интегрированных геофизических методов, включая аналитический сигнал, наклонное производное поле, фазовую симметрию, изображение параметров источников, полосовую фильтрацию Баттерворта, трёхмерную инверсию магнитных аномалий и деконволюцию Эйлера. Эти методы позволили выделить подповерхностные структуры, определить их пространственное распределение, глубины залегания и взаимосвязь с проявлениями полезных ископаемых. Результаты показали наличие линейных зон северо-восточного и северо-западного простираний, соответствующих главным зонам сдвига и разломным системам, контролирующим внедрение минерального вещества. Неглубокие источники (250-500 м) связаны с промышленными минералами, такими как глина; промежуточные глубины (500-720 м) с редкометалльными пегматитами, содержащими колумбит-танталит и вольфрамит; тогда как глубинные структуры (>1200 м) указывают на потенциальные области зарождения

минерализующих флюидов. Высокоамплитудные аномалии аналитического сигнала (0.04-0.05 нТ/м) совпадают с геологическими контактами и структурными границами, обозначая зоны возможной минерализации. Данное исследование представляет собой первую комплексную работу, направленную на изучение подповерхностных минерализованных структур региона. Применение комплекса геофизических методов позволило выявить ранее неотражённые структурные особенности и подтвердить вертикальную непрерывность минерализованных зон. Полученные результаты обеспечивают глубинно-ориентированное картирование экономически значимых месторождений, предоставляя ценные сведения для целенаправленных геологоразведочных работ и способствуя разработке более точных и экономически эффективных стратегий поисков колумбит-танталита, вольфрамита, каолина и других промышленных минералов в пределах кристаллического фундамента.

Ключевые слова: *магнитные данные, разведка полезных ископаемых, глубины, структурный контроль, горное дело, кристаллический фундамент.*

Publisher's note

All claims expressed in this manuscript are solely those of the authors and do not necessarily represent those of their affiliated organizations, or those of the publisher, the editors and the reviewers.

SATBAYEV UNIVERSITY

Engineering Journal of Satbayev University

Volume 147 (2025), Issue 6, 40-47

https://doi.org/10.51301/ejsu.2025.i6.05

Prospects for utilizing natural gas from the Anabai gas field for synthesis gas production via dry reforming of methane

B.B. Zhaparov*, B.B. Bissenov, Zh.S. Tulemissova

Kazakh-British Technical University, Almaty, Kazakhstan

**Corresponding author: bo.zh@mail.ru*

Abstract. Dry reforming of methane (DRM) is a promising approach for producing synthesis gas, a mixture of hydrogen and carbon monoxide, which serves as a valuable intermediate for energy and chemical applications. In the context of the global energy transition, hydrogen is considered a potential low-carbon energy carrier, while DRM enables the simultaneous utilization of methane and carbon dioxide. This study aimed to assess the prospects of the Anabai gas field for converting produced natural gas into synthesis gas via the DRM reaction and to demonstrate the practical feasibility of methane conversion based on laboratory-scale experiments. To evaluate the potential of methane utilization, data on the methane content of natural gas from the Anabai field under surface and subsurface conditions were analyzed. Surface gas characteristics were determined using 56 wellhead samples from Famennian, Lower, Middle, and Upper Visean, as well as Serpukhovian deposits. Subsurface gas composition was assessed based on 102 samples from the Famennian, Tournaisian, and Visean–Serpukhovian stages. The results indicate a consistently high methane content across the studied stratigraphic horizons. Experimental DRM studies were carried out using a 20Co-10Mg-20Al catalyst synthesized by the self-propagating high-temperature synthesis (SHS) method. The catalytic performance was evaluated in terms of methane and carbon dioxide conversion, synthesis gas composition, and temperature dependence. Based on the experimental results, practical recommendations for implementing DRM at the Anabai gas field are proposed, and the prospects for integrating this technology into environmentally oriented energy production schemes are discussed.

Keywords: *gas field, dry methane reforming, syngas, methane, hydrogen*.

Received: 16 June 2025
Accepted: 15 December 2025
Available online: 31 December 2025

1. Introduction

Currently, humanity is facing increasingly urgent challenges related to the planet's future development. Intensive human activity and extensive industrial growth over recent decades have led to significant environmental degradation on a global scale. Anthropogenic factors play a significant role in climate change and the large-scale transformation of natural ecosystems. Issues such as greenhouse gas emissions, global warming, environmental pollution, biodiversity loss, soil degradation, and desertification have become widely recognized and discussed worldwide. These challenges are inherently global, as their consequences extend beyond national borders and impact societies and ecosystems worldwide.

In response to the growing environmental risks and their potential long-term impacts, governments and international organizations have undertaken a range of mitigation and sustainability-oriented initiatives. Environmental protection and sustainable development occupy a central position on the United Nations' agenda. In particular, in 2015, the UN General Assembly adopted the Sustainable Development Goals (SDGs), formulated as a comprehensive framework aimed at achieving balanced economic growth, social well-being, and environmental sustainability. Within this framework, the transition toward a more sustainable and resilient global energy system, commonly referred to as the energy transition, has been identified as one of the key pathways for reducing environmental pressures and ensuring long-term development. The concept of the energy transition refers to a profound structural transformation of the global energy sector as an integrated system. This transformation is driven by changes in the energy mix, including the increasing deployment of new and renewable energy sources, as well as a gradual reduction in the share of conventional fossil fuels in total global energy production.

From a historical perspective, the development of the global energy system can be divided into four primary stages of energy transition. The first stage is associated with the shift from the use of relatively inefficient but readily available biomass, primarily wood, to a more energy-dense fossil fuel – coal. This transition began in the second half of the nineteenth century, driven by rapid industrialization and the widespread adoption of steam engines, and is generally considered to have been completed by the beginning of the twentieth century. During this period, the share of coal in the global energy balance increased significantly, from marginal levels to approximately 50%.

bo.zh@mail.ru; baubek.bissenov@gmail.com; z.tulemissova@kbtu.kz
Engineering Journal of Satbayev University. eISSN 2959-2348. Published by Satbayev University

The second stage of the energy transition is characterized by the growing dominance of oil as a primary energy source. Its role increased substantially throughout the twentieth century, with oil accounting for approximately 3% of the global fuel balance in 1915 and rising to about 45% by 1975. The third stage corresponds to the widespread introduction of natural gas in both energy production and industrial applications. Unlike previous stages, this period is characterized by the absence of a single dominant energy resource and a more diversified energy structure.

The fourth stage of the energy transition has been underway since the early 2000s. It is characterized by the large-scale deployment of renewable energy sources and a gradual shift away from fossil fuels, specifically hydrocarbons. According to the International Energy Agency, this transition is expected to extend through the middle of the twenty-second century, with a projected completion around 2150. Thus, the present period can be regarded as an active phase of the fourth energy transition. In this context, the investigation of hydrogen production pathways derived from natural gas and methane, in particular, has become increasingly relevant as a potential component of a more sustainable and low-carbon energy system.

Dry reforming of methane (DRM) has been widely investigated as a sustainable pathway for the simultaneous conversion of two primary greenhouse gases, CH_4 and CO_2, into synthesis gas, which serves as a key intermediate for the production of fuels and value-added chemicals [1, 2]. Among the various catalytic systems explored, Ni- and Co-based catalysts have received considerable attention due to their high intrinsic activity and economic advantages over noble-metal catalysts [3, 4]. However, the practical deployment of these materials is still hindered by catalyst deactivation under severe DRM conditions, primarily caused by carbon deposition, metal sintering, and insufficient thermal stability.

To address these limitations, significant research efforts have focused on developing advanced catalyst preparation techniques and compositional modifications. In particular, solution combustion synthesis (SCS) and self-propagating high-temperature synthesis (SHS) have emerged as efficient and versatile methods for producing catalysts with highly dispersed active phases, strong metal-support interactions, and improved resistance to deactivation [5-7]. Catalysts prepared via these methods often exhibit enhanced redox properties and structural stability compared to conventionally synthesized materials, making them especially attractive for high-temperature DRM applications.

Further enhancement of catalytic performance has been achieved through the incorporation of promoter oxides and secondary metals. Rare-earth oxides, such as CeO_2 and La_2O_3, have been reported to improve oxygen mobility and facilitate the gasification of surface carbon species, thereby suppressing coke formation on Ni-based catalysts [8]. In addition, the introduction of transition metal promoters, including Mn, Mg, and Fe, has been shown to modify the acid–base characteristics and redox behavior of the catalyst surface, leading to improved catalytic activity, stability, and syngas selectivity in DRM reactions [9-11].

In parallel with Ni-based systems, increasing attention has been devoted to Co-based catalysts, which generally exhibit a lower tendency toward carbon formation. Recent studies have demonstrated that lanthanide-doped Co-Al catalysts prepared by SCS exhibit promising catalytic activity and stability in DRM, highlighting the potential of Co-Ce-Al and Co-La-Al formulations as viable alternatives to conventional Ni-containing catalysts [12, 13]. Overall, the existing body of literature confirms the high potential of Ni- and Co-based catalysts synthesized via combustion-based methods for DRM. Nevertheless, a comprehensive understanding of the interplay between catalyst composition, promoter selection, and synthesis parameters remains incomplete, emphasizing the need for further systematic and comparative investigations [1-13].

The purpose of this research work was to demonstrate the potential of the Anabai gas field in utilizing the extracted natural gas to convert it into synthesis gas through the DRM reaction, and to investigate and illustrate, using laboratory scientific experiments on DRM, the practical feasibility of obtaining synthesis gas from methane.

2. Materials and methods

2.1. Object of study and characteristics of the Anabai gas field

The object of this study is the Anabai gas field, which is currently under industrial exploitation and is characterized by a high methane content in the produced natural gas. This feature allows the field to be considered a promising source of methane for synthesis gas production via dry reforming of methane (DRM). The Anabai gas field is situated in the Moiynkum district of the Zhambyl region in the Republic of Kazakhstan, approximately 210 kilometers north of the city of Taraz.

According to the Anabai Deposit Development Project [14], the component composition of natural gas from the Anabai field was investigated under both surface and reservoir (deep) conditions. Under surface conditions, 56 wellhead gas samples were analyzed from Famennian, Lower, Middle, and Upper Visean, as well as Serpukhovian deposits. Several samples exhibiting anomalously low or high methane contents were excluded from the dataset. The methane concentration under surface conditions was found to range from approximately 88% to 91%, depending on the stratigraphic horizon.

The reservoir gas composition was evaluated based on 102 deep gas samples collected from Famennian, Tournaisian, Lower, Middle, and Upper Visean, and Serpukhovian formations. After excluding anomalous samples, the methane content in the reservoir gas generally ranged from 80% to 83% for Visean and Serpukhovian deposits. In comparison, significantly higher methane concentrations (up to 95-98%) were observed for Tournaisian reservoirs. The Famennian reservoir gas exhibited an average methane content of approximately 90%. Overall, the consistently high methane content across different stratigraphic horizons confirms the suitability of natural gas from the Anabai field as a feedstock for producing synthesis gas.

2.2. Catalyst preparation

Overall, the consistently high methane content across different stratigraphic horizons confirms the suitability of natural gas from the Anabai field as a feedstock for producing synthesis gas.

The SHS process is based on the ability of powder mixtures containing fuels and oxidizers to ignite upon local heating, followed by the propagation of a combustion wave throughout the reacting system. This process leads to the formation of solid products with high porosity and developed surface morphology.

For catalyst synthesis, 20 g of precursor materials were used, including 10 g of urea (CH_4N_2O) as a fuel, 4 g of cobalt(II) nitrate hexahydrate ($Co(NO_3)_2{\cdot}6H_2O$), 2 g of magnesium nitrate hexahydrate ($Mg(NO_3)_2{\cdot}6H_2O$), and 4 g of aluminum nitrate nonahydrate ($Al(NO_3)_3{\cdot}9H_2O$). The precursors were dissolved in 15 mL of deionized water in a heat-resistant chemical beaker. Urea was employed to ensure stable combustion, with the fuel-to-oxidizer ratio maintained at unity.

The resulting solution was preheated to 80°C under continuous stirring to ensure complete dissolution of the components. The homogeneous solution was then placed into a muffle furnace preheated to 500°C, where combustion occurred over a period of 10-15 minutes. As a result, a solid foam-like material was formed. After synthesis, the obtained material was cooled to room temperature (approximately 20°C) for 30 minutes, crushed into a fine powder, and stored for further use.

2.3. Experimental setup and DRM procedure

The DRM experiments were conducted using the laboratory facilities of the JSC Institute of Fuel, Catalysis, and Electrochemistry, named after D.V. Sokolsky. The experimental setup included an automated laboratory unit equipped with a CHROMOS GC-1000 gas chromatograph, a muffle furnace, and analytical laboratory balances.

The reaction was carried out in a quartz tubular reactor, which was installed inside a furnace. The reactor was packed sequentially with glass wool, 2 mL of quartz, 2 mL of the catalyst, followed by another 2 mL of quartz and glass wool to ensure uniform gas flow and temperature distribution. The reactor was positioned such that its central zone coincided with the furnace temperature sensor, allowing accurate control and monitoring of the reaction temperature.

The DRM reaction was conducted at atmospheric pressure using a gas mixture of CH_4 and CO_2 diluted with argon, with a volumetric ratio of CH_4:CO_2:Ar = 1:1:1. The total gas flow rate through the reactor was maintained at 100 $mL{\cdot}min^{-1}$. The dry reforming of methane proceeds according to the following reaction:

$$CH_4 + CO_2 \rightarrow 2H_2 + 2CO, \quad (1)$$

The reactor temperature was increased stepwise from 500°C to 900°C in increments of 100°C. At each temperature, the composition of the reaction products was analyzed every 30 minutes using the CHROMOS GC-1000 gas chromatograph equipped with Chromos software.

3. Results and discussion

To assess the reliability of the experimental results, all measurements were performed in duplicate under identical conditions. The reproducibility of the obtained data was satisfactory, indicating a high level of measurement reliability and experimental consistency.

Table 1 summarizes the inlet and outlet concentrations of methane and carbon dioxide obtained during the evaluation of the catalytic activity of the 20Co-10Mg-20Al catalyst in the dry reforming of methane (DRM) reaction over the temperature range of 500-900°C.

At temperatures of 500 and 600°C, the outlet concentrations of methane and carbon dioxide remain close to their inlet values, indicating limited catalytic activity in this temperature range.

Table 1. Inlet and outlet concentrations of methane and carbon dioxide during DRM over the 20Co-10Mg-20Al catalyst

Temperature, °C	CH_4 in., %	CO_2 in., %	CH_4 out., %	CO_2 out., %
500	33	33	29.62	33
600	33	33	29.09	33
700	33	33	11.88	16.36
800	33	33	0.33	6.29
900	33	33	0	4.91

This behavior is typical for DRM, a highly endothermic reaction that requires elevated temperatures to achieve significant reactant conversion.

A pronounced increase in catalytic activity is observed at 700°C, where a substantial decrease in both CH_4 and CO_2 outlet concentrations is detected. The methane concentration decreases from 33% at the reactor inlet to 11.88% at the outlet, while the CO_2 concentration decreases to 16.36%. This temperature marks the onset of effective DRM over the 20Co-10Mg-20Al catalyst.

A pronounced increase in catalytic activity is observed at 700°C, where a substantial decrease in both CH_4 and CO_2 outlet concentrations is detected. The methane concentration decreases from 33% at the reactor inlet to 11.88% at the outlet, while the CO_2 concentration decreases to 16.36%. This temperature marks the onset of effective DRM over the 20Co-10Mg-20Al catalyst.

The observed temperature-dependent behavior can be attributed to the endothermic nature of the DRM reaction and the increased availability of active sites at higher temperatures. The presence of cobalt as the primary active metal contributes to high methane activation efficiency, while magnesium and aluminum oxides likely enhance catalyst stability and modify surface basicity, facilitating CO_2 activation and carbon gasification.

Overall, the results demonstrate that the 20Co-10Mg-20Al catalyst exhibits high catalytic activity in DRM at temperatures above 700°C, with near-complete methane conversion achieved at 800-900°C. These findings confirm the suitability of the investigated catalyst composition for high-temperature DRM applications. They are consistent with trends reported in the literature for Co-based catalysts synthesized via combustion-based methods.

The experimental data obtained in this study are presented graphically in Figures 1-4. The reproducibility of the measurements supports the reliability of the results, as all experiments were performed in duplicate under identical conditions, yielding consistent trends in gas conversion and product composition.

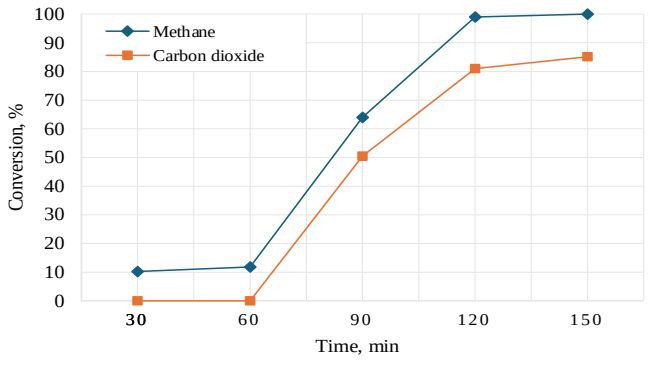

Figure 1. Dependence of methane and carbon dioxide conversion on reaction time during DRM over the 20Co-10Mg-20Al catalyst

Figure 1 illustrates the dependence of methane and carbon dioxide conversion on reaction time during DRM over the 20Co-10Mg-20Al catalyst. At short reaction times (30-60 min), the conversion of both reactants remains low, indicating that the catalytic system requires a specific stabilization period under reaction conditions. With increasing reaction time, a pronounced increase in methane conversion is observed, reaching nearly complete conversion after 120-150 min. A similar trend is evident for carbon dioxide, although its conversion remains slightly lower than that of methane throughout the experiment. This behavior suggests progressive activation of the catalyst surface and the establishment of steady-state reaction conditions.

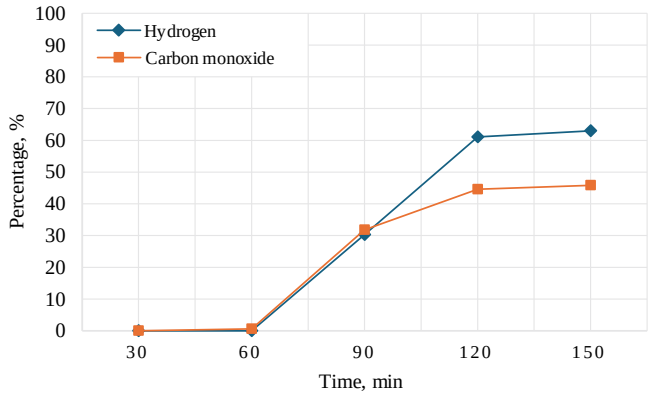

Figure 2. Dependence of hydrogen and carbon monoxide formation on reaction time during DRM over the 20Co-10Mg-20Al catalyst

A corresponding increase in the formation of reaction products is evident in Figure 2, which illustrates the evolution of hydrogen and carbon monoxide concentrations over time. The gradual rise in H_2 and CO content correlates well with the increasing conversions of CH_4 and CO_2, confirming that the observed reactant consumption is predominantly associated with the DRM reaction. After approximately 120 min, the product composition approaches a quasi-steady state, indicating stable catalyst performance under the investigated conditions.

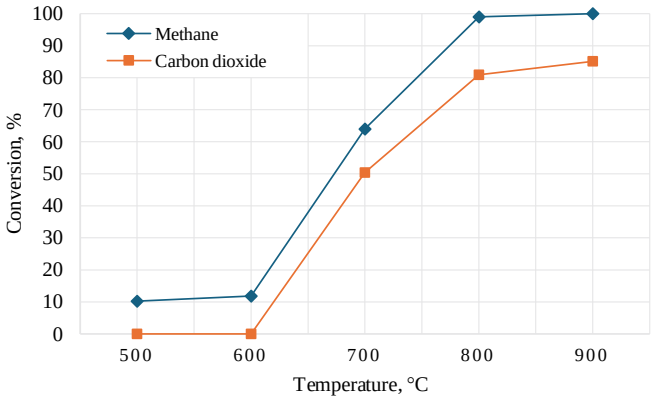

Figure 3. Effect of reaction temperature on methane and carbon dioxide conversion during DRM over the 20Co-10Mg-20Al catalyst

The influence of reaction temperature on DRM performance is depicted in Figure 3. Both methane and carbon dioxide conversions exhibit a strong positive dependence on temperature. At 500-600°C, the conversions remain relatively low, reflecting the endothermic nature of DRM and the limited activation of reactant molecules at lower temperatures. A sharp increase in conversion is observed at 700°C, marking the onset of effective DRM over the 20Co-10Mg-20Al catalyst. At 800-900°C, methane conversion reaches nearly 100%, while carbon dioxide conversion exceeds 80%, demonstrating high catalytic activity at elevated temperatures.

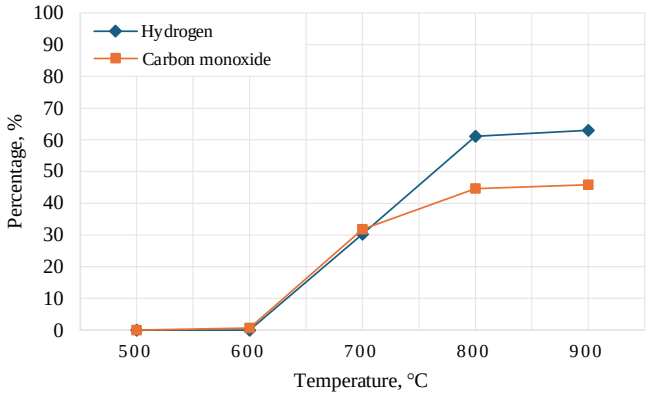

Figure 4. Effect of reaction temperature on hydrogen and carbon monoxide formation during DRM over the 20Co-10Mg-20Al catalyst

Figure 4 shows the corresponding effect of temperature on the composition of the gaseous products. The concentrations of hydrogen and carbon monoxide increase significantly with increasing temperature, which is consistent with the enhanced DRM reaction rate. At temperatures above 700°C, the H_2 and CO contents rise markedly, approaching values characteristic of synthesis gas suitable for downstream applications. The higher hydrogen yield compared to carbon monoxide can be attributed to the combined contribution of DRM and possible side reactions, such as methane cracking and the reverse water-gas shift reaction.

The catalytic performance of the 20Co-10Mg-20Al system is strongly dependent on both reaction time and temperature. Efficient methane and carbon dioxide conversion, accompanied by high synthesis gas yields, is achieved at temperatures above 700°C and after sufficient reaction time to reach steady-state conditions. These findings confirm the suitability of the investigated catalyst composition for high-temperature DRM. They are in good agreement with general trends reported for Co-based catalysts prepared by combustion-based synthesis methods.

This paper presents a comparative assessment of the behavior of the 20Co-10Mg-20Al catalyst in the DRM reaction at five temperatures: 500°C, 600°C, 700°C, 800°C, and 900°C. The analysis focuses on the calculated conversions of CH_4 and CO_2, as well as on the composition of the gaseous products, namely CO and H_2.

The outlet concentrations of CH_4, CO_2, CO, and H_2 were experimentally measured, and the corresponding conversion values were calculated using the following relationships:

$$X_{CH_4} = \frac{CH_4^{in} - CH_4^{out}}{CH_4^{in}} \cdot 100\,, \qquad (2)$$

$$X_{CO_2} = \frac{CO_2^{in} - CO_2^{out}}{CO_4^{in}} \cdot 100 \qquad (3)$$

The 20Co-10Mg-20Al catalytic system exhibits low activity at the lower temperatures of 500°C and 600°C. Under these conditions, methane conversions reach only 10.2% and 11.8%, respectively, while the formation of syngas components (CO and H_2) is negligible. At such temperatures, methane molecules, characterized by strong C–H bonds with a bond dissociation energy of approximately 435 kJ·mol^{-1}, cannot be efficiently activated on the surface of the cobalt-based catalyst. As a result, the DRM pathway ($CH_4 + CO_2 \rightarrow 2CO + 2H_2$) is kinetically suppressed.

In contrast, CO_2, although thermodynamically stable, can participate in secondary reactions when trace amounts of oxygen or water are present in the system. One possible route for CO_2 formation involves the partial oxidation of methane ($CH_4 + 2O_2 \rightarrow CO_2 + 2H_2O$), notably if the catalyst has not been fully reduced or if residual oxidized species remain on the support surface. Another pathway is associated with the oxidation of carbon deposits formed during the cracking of methane ($CH_4 \rightarrow C + 2H_2$). These deposits can subsequently react with CO_2 via the Boudouard reaction or gasification, leading to additional formation of CO and CO_2:

$$C + CO_2 \rightarrow 2CO \quad (4)$$

In both cases, the net effect is an increased concentration of CO_2 at the reactor outlet, even though no excess CO_2 is introduced into the feed. Such parasitic reactions reduce the overall carbon efficiency of the process, indicating insufficient catalyst activation or limited dispersion of metallic cobalt species at low temperatures.

A significant enhancement in catalytic performance is observed as the temperature increases to 700°C. Under these conditions, methane conversion rises sharply to 64%, while CO_2 conversion reaches 50.4%. This increase is accompanied by substantial production of H_2 (30.28 mmol) and CO (31.79 mmol), indicating effective activation of the DRM reaction pathway. The pronounced jump in activity is consistent with the known kinetic barriers associated with CH_4 dissociation. It suggests that the threshold temperature for efficient C–H bond cleavage on metallic Co^0 active sites has been reached. In this context, cobalt plays a crucial role by enabling the dissociative adsorption of methane, resulting in surface-bound carbon (C^*) and hydrogen (H^*) species, which subsequently react with adsorbed CO_2-derived intermediates.

The high methane conversions of 99% and 100%, together with carbon dioxide conversions of 80.9% and 85.1% at elevated temperatures of 800°C and 900°C, respectively, further demonstrate the strong temperature dependence of DRM performance over the investigated catalyst. Such temperatures correspond to conditions close to the thermodynamic equilibrium region for highly endothermic reactions such as DRM. The increased yields of CO and H_2 observed at these temperatures indicate enhanced reaction kinetics, higher surface mobility of the reactants, and an increased availability of active metallic Co^0 surface sites.

In addition to the intrinsic catalytic activity of cobalt, the role of Mg and Al as support components should also be emphasized. Magnesium oxide introduces basic surface sites that promote the adsorption and activation of CO_2. This basicity compensates for the acidic character of Al_2O_3, resulting in a balanced support environment that can stabilize CO2 in the form of carbonate or bicarbonate intermediates before their decomposition into reactive CO_2 species. Such dual functionality enhances CO_2 uptake and contributes to the suppression of carbon deposition by facilitating gas-solid interactions. Moreover, MgO may promote a more uniform dispersion of cobalt species within the support matrix, thereby minimizing sintering at elevated temperatures and improving catalyst durability.

The consistency in the formation of both H_2 and CO further suggests that the reverse water-gas shift reaction (RWGS) does not play a dominant role under the investigated conditions. In systems where RWGS becomes significant ($CO_2 + H_2 \rightarrow CO + H_2O$), the H_2/CO ratio typically decreases below unity. In contrast, the present results indicate an H_2/CO ratio close to unity across the entire temperature range, implying that the DRM pathway proceeds selectively with limited interference from side reactions.

The DRM mechanism over Co-based catalysts is commonly described using a bifunctional model. Methane activation predominantly occurs on metallic cobalt sites, which provide the necessary electronic structure and geometry for the cleavage of C-H bonds. In contrast, CO_2 preferentially interacts with oxide supports or oxygen-containing surface species. The coexistence of MgO and Al_2O_3 in the catalyst creates a heterogeneous surface with multiple types of active sites. Surface carbon species (C^*) formed during methane cracking can readily react with oxygen-containing intermediates derived from adsorbed CO_2 (such as O^* or CO_3^{2-}), leading to CO formation and completion of the catalytic cycle.

From a performance perspective, the 20Co-10Mg-20Al catalyst exhibits promising characteristics. The sharp increase in conversion between 600°C and 700°C indicates effective thermal activation, while the near-complete methane conversion at 800-900°C reflects high intrinsic catalytic activity. The high yields of H_2 and CO, together with a stable H_2/CO ratio, further confirm both the efficiency and selectivity of the catalyst under high-temperature DRM conditions.

Nevertheless, certain limitations should be noted. The absence of significant activity at temperatures around 650°C may restrict the applicability of the catalyst in processes designed to operate under milder conditions for improved energy efficiency. Additionally, the present study does not address long-term stability or regeneration behavior, which are crucial parameters for industrial implementation. Coke formation, although not directly reflected in the observed conversion values, remains a persistent challenge in DRM, particularly at elevated temperatures and under conditions where carbon gasification pathways are limited.

In summary, the 20Co-10Mg-20Al catalyst exhibits a distinct activation threshold in the range of 650-700°C, above which it demonstrates high efficiency in the DRM reaction. The synergistic interaction between metallic cobalt, basic MgO, and structurally stable Al_2O_3 provides a solid foundation for achieving high CH_4 and CO_2 conversions, elevated synthesis gas yields, and consistent reaction selectivity.

To evaluate the structural and elemental stability of the 20Co-10Mg-20Al catalyst under DRM conditions, a comparative analysis was performed using scanning electron microscopy (SEM) coupled with energy-dispersive X-ray spectroscopy (EDS). Both fresh and spent catalyst samples were examined to assess their morphological features, elemental composition, and surface changes induced by the reaction.

Representative SEM images and corresponding EDS spectra of the fresh and spent catalysts are presented in Figure 5a and Figure 5b, respectively.

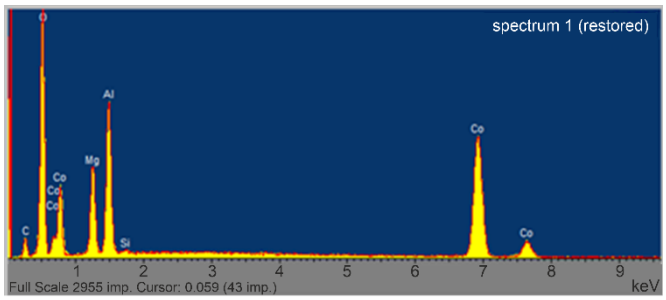

Fresh 20Co-10Mg-20Al

(a)

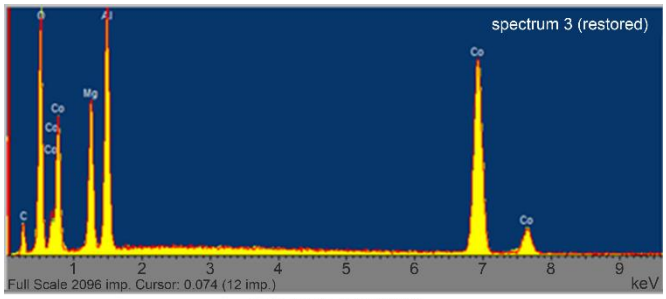

Spent 20Co-10Mg-20Al

(b)

Figure 5. EDS spectra of the 20Co-10Mg-20Al catalyst: (a) – fresh sample; (b) – spent sample after DRM reaction

The fresh catalyst sample (Figure 5a) exhibits a porous and well-developed surface morphology, as observed by SEM. Uniformly distributed surface features characterize the structure, with no visible signs of particle agglomeration or sintering. Such morphology is advantageous for DRM, as it provides a high accessible surface area and facilitates the exposure of active catalytic sites. The corresponding EDS analysis confirms the presence of all expected elements, including cobalt (Co), magnesium (Mg), aluminum (Al), and oxygen (O), as well as trace amounts of silicon (Si), which are most likely associated with the substrate or external contamination. The average elemental composition (wt.%) of the fresh catalyst was determined as follows: Co – 47.31%, O – 29.35%, Al – 13.83%, Mg – 9.44%, and Si – 0.07%. These results confirm the successful incorporation of all catalyst components in the intended proportions. The high cobalt content reflects its role as the primary active phase, while MgO and Al_2O_3 act as structural and textural stabilizers.

The spent catalyst sample (Figure 5b) also demonstrates favorable structural characteristics after DRM operation. SEM analysis reveals that the overall porous morphology is largely preserved, with no evidence of severe support degradation or cobalt sintering. Although slight surface smoothing and limited particle growth are observed, these changes remain within acceptable limits and do not indicate significant structural deterioration. Filamentous carbon species, typically associated with DRM, are detected on the catalyst surface, confirming catalytic activity during operation. Importantly, no encapsulation of the active phase or extensive aggregation is observed, suggesting that the active cobalt sites remain accessible after reaction.

EDS analysis of the spent catalyst confirms the presence of all key elements across different surface regions. The average elemental composition (wt.%) was determined as: Co – 48.48%, O – 23.29%, Al – 16.57%, and Mg – 11.66%. Compared to the fresh catalyst, the cobalt content increased by approximately 1.17%, which can be attributed to surface enrichment resulting from the reduction of cobalt oxide species to metallic cobalt during the DRM process. Simultaneously, the oxygen content decreased by about 6.06%, consistent with partial lattice oxygen removal under high-temperature and reducing reaction conditions. The relative increase in Al and Mg contents is primarily associated with the decrease in oxygen concentration, which enhances the relative contribution of metallic elements in the EDS signal.

The EDS spectra of the spent catalyst show well-defined cobalt peaks, particularly at approximately 6.9 and 7.6 keV, corresponding to Co Kα and Kβ lines, respectively. This observation confirms the presence and stability of metallic Co^0 as the active phase after reaction. The preservation of peak intensity and sharpness indicates the absence of significant cobalt sintering or particle migration during the DRM process. Magnesium and aluminum signals remain stable, confirming the chemical robustness of the MgO-Al_2O_3 support matrix under reaction conditions. Trace silicon detected in isolated spectra is considered extrinsic and not intrinsic to the catalyst formulation.

Overall, the SEM-EDS results demonstrate that the 20Co-10Mg-20Al catalyst maintains both structural integrity and elemental stability during DRM operation. The preservation of a porous morphology, stable dispersion of metallic cobalt, and the supportive role of MgO and Al_2O_3 collectively contribute to sustained catalytic activity and resistance to severe deactivation mechanisms.

4. Conclusions

During the experiments, it was found that the conversion of methane into synthesis gas via DRM using the 20Co-10Mg-20Al catalyst begins at a reaction temperature of 700°C. At a reaction temperature of 800°C, the conversion is nearly complete. Specifically, at a reaction temperature of 600°C, the methane conversion rate is only 11.85%, showing minimal changes. However, at 700°C, the conversion rate increases sharply to 64%, and at 800°C, it reaches 99%. Thus, it can be concluded that for this catalyst and under the given conditions, the optimal temperature for the DRM reaction lies within the range of 700°C to 800°C.

The synthesized gas produced in this reaction has promising potential as a renewable energy source, especially for fuel energy. Considering the high methane content in the Anabai gas field, this technology offers a valuable method for converting methane into hydrogen. Therefore, it is recommended to implement this process at the Anabai gas field, given its promising energy generation capabilities.

The forecasts for implementing this technology are optimistic. In the future, it may lead to a more environmentally friendly energy production process, contributing to the Republic of Kazakhstan's achievement of sustainable development goals, particularly in the energy sector.

This paper demonstrates the prospects of converting natural gas produced at the Anabai gas field into hydrogen, a cleaner fuel. While the technology is still in the early stages and requires further comprehensive scientific research, it holds significant potential. Future studies should focus on discovering new, more effective catalysts for the DRM process. Despite the challenges, this area of research shows great promise and offers opportunities for further advancements in sustainable energy production.

Author contributions

Conceptualization: BBZ; Data curation: BBZ, BBB; Formal analysis: BBZ, BBB; Funding acquisition: BBZ; Investigation: BBZ, BBB; Methodology: BBZ, BBB; Project administration: BBZ; Resources: BBZ, BBB; Software: BBZ, BBB; Supervision: BBZ, BBB, Zh.S.T; Validation: BBZ, BBB; Visualization: BBZ, BBB; Writing – original draft: BBZ, BBB; Writing – review & editing: BBZ, BBB. All authors have read and agreed to the published version of the manuscript.

Funding

This research received no external funding.

Acknowledgements

The authors would like to express their sincere gratitude to the editor and the two anonymous reviewers for their constructive comments and valuable suggestions, which significantly contributed to the improvement of the manuscript. Additionally, the authors extend their heartfelt thanks to the staff of the Oxidative Catalysis Laboratory at JSC «Institute of Fuel, Catalysis and Electrochemistry named after D.V. Sokolsky», Almaty, for providing the laboratory equipment, as well as for their methodological assistance and ongoing information support.

Conflicts of interests

The authors declare no conflict of interest.

Data availability statement

The original contributions presented in this study are included in the article. Further inquiries can be directed to the corresponding author.

References

[1] Talasbayeva, N.S., Kazhdenbek, B.D., Zhang, X.L., Kaumenova, G.N., Xanthopoulou, G., Tungatarova, S.A. & Baizhumanova, T.S. (2019). Catalytic conversion of methane into syngas and ethylene. *Series chemistry and technology*, *3*(435), 6-12. https://doi.org/10.32014/2019.2518-1491.22

[2] Zhang, X., Maki-Arvela, P., Palonen, H., Murzin, D.Y., Aubakirov, Y.A., Tungatarova, S.A. & Baizhumanova, T.S. (2020). Catalytic reforming of methane into synthesis-gas. *Materials Today: Proceedings*, *31*, 595-597. https://doi.org/10.1016/j.matpr.2020.07.406

[3] Zhumabek, M., Kaumenova, G., Augaliev, D., Alaidar, Y., Murzin, D., Tungatarova, S., Xanthopoulou, G., Kotov, S. & Baizhumanova, T. (2021). Selective Catalytic Reforming of Methane into Synthesis Gas. *Chemical Engineering & Technology*, *44*(11), 2026-2033. https://doi.org/10.1002/ceat.202100247

[4] Zhang, X., Vajglova, Z., Mäki-Arvela, P., Peurla, M., Palonen, H., Murzin, D.Yu., Tungatarova, S.A., Baizhumanova, T.S. & Aubakirov, Y.A. (2021). Mono- and Bimetallic Ni−Co Catalysts in Dry Reforming of Methane. *ChemistrySelect*, *6*(14), 3424-3434. Portico. https://doi.org/10.1002/slct.202100686

[5] Tungatarova, S., Xanthopoulou, G., Vekinis, G., Karanasios, K., Baizhumanova, T., Zhumabek, M. & Sadenova, M. (2022). Ni-Al Self-Propagating High-Temperature Synthesis Catalysts in Dry Reforming of Methane to Hydrogen-Enriched Fuel Mixtures. *Catalysts*, *12*(10), 1270. https://doi.org/10.3390/catal12101270

[6] Xanthopoulou, G., Varitis, S., Zhumabek, M., Karanasios, K., Vekinis, G., Tungatarova, S.A. & Baizhumanova, T.S. (2021). Direct Reduction in Greenhouse Gases by Continuous Dry (CO2) Reforming of Methane over Ni-Containing SHS Catalysts. *Energies*, *14*(19), 6078. https://doi.org/10.3390/en14196078

[7] Zhumabek, M., Xanthopoulou, G., Tungatarova, S.A., Baizhumanova, T.S., Vekinis, G. & Murzin, D.Yu. (2021). Biogas Reforming over Al-Co Catalyst Prepared by Solution Combustion Synthesis Method. *Catalysts*, *11*(2), 274. https://doi.org/10.3390/catal11020274

[8] Manabayeva, A., Mäki-Arvela, P., Vajglová, Z., Martinez-Klimov, M., Yevdokimova, O., Peuronen, A., Lastusaari, M., Tirri, T., Kassymkan, K., Baizhumanova, T. S., Zhumabek, M., Sarsenova, R.O., Zheksenbaeva, Z.T., Kaumenova, G.N., Russo, V., Murzin, D.Yu. & Tungatarova, S.A. (2023). Dry Reforming of Methane over Rare-Earth Metal Oxide Ni–M–Al (M = Ce, La) Catalysts. *Industrial&Engineering Chemistry Research*, *62*(48), 20588-20607. https://doi.org/10.1021/acs.iecr.3c02341

[9] Manabayeva, A. M., Mäki-Arvela, P., Vajglová, Z., Martinéz-Klimov, M., Yevdokimova, O., Peuronen, A., Lastusaari, M., Tirri, T., Tungatarova, S.A., Baizhumanova, T. S., Kassymkan, K., Kaumenova, G.N., Zhumabek, M., Zhumadullaev, D.A., Shoganbek, D. & Murzin, D.Yu. (2025). Mg-modified Ni-based catalysts prepared by the solution combustion synthesis for dry reforming of methane. *Catalysis Today*, *453*, 115261. https://doi.org/10.1016/j.cattod.2025.115261

[10] Manabayeva, A. M., Mäki-Arvela, P., Vajglová, Z., Martinez-Klimov, M., Yevdokimova, O., Peuronen, A., Lastusaari, M., Tirri, T., Baizhumanova, T S., Kassymkan, K., Kaumenova, G.N., Brodskiy, A.R., Sarsenova, R.O., Shorayeva, K.A., Murzin, D. Yu. & Tungatarova, S.A. (2024). Dry Reforming of Methane over Mn-modified Ni-based Catalysts. *Catalysis Letters*, *154*(8), 4780-4794. https://doi.org/10.1007/s10562-024-04676-0

[11] Manabayeva, A.M., Mäki-Arvela, P., Vajglová, Z., Martinéz-Klimov, M., Tirri, T., Baizhumanova, T.S., Grigor'eva, V.P., Zhumabek, M., Aubakirov, Y.A., Simakova, I.L., Murzin, D. Yu., & Tungatarova, S.A. (2023). Dry Reforming of Methane over Ni–Fe–Al Catalysts Prepared by Solution Combustion Synthesis. *Industrial & Engineering Chemistry Research*, *62*(29), 11439-11455. https://doi.org/10.1021/acs.iecr.3c00272

[12] Shoganbek, D., Martinez-Klimov, M., Yevdokimova, O., Peuronen, A., Lastusaari, M., Aho, A., Tungatarova, S.A., Baizhumanova, T.S., Zhumadullaev, D.A., Zhumabek, M., Aubakirov, Y.A., Manabayeva, A., Mäki-Arvela, P. & Murzin, D. Yu. (2025). Dry methane reforming over lanthanide-doped Co–Al catalysts prepared via a solution combustion method. *Materials Advances*, *6*(3), 1173-1190. https://doi.org/10.1039/d4ma00991f

[13] Shoganbek, D., Tungatarova, S., Murzin, D.Y., Baizhumanova, T.S. & Zhumabek, M. (2025). Dry reforming of methane on Co-La-Al and Co-Ce-Al catalysts prepared by the SCS method. Series chemistry and technology. *Series Chemistry and Technology*, (1), 195-205. https://doi.org/10.32014/2025.2518-1491.277

[14] LLC «Optimum design institute». (2021). Anabai deposit development project as of 01.07.2021

Анабай газ кен орнының өндірілген табиғи газды метанды құрғақ риформинг реакциясы арқылы синтездік газға айналдыру үшін пайдаланудағы перспективалары

Б.Б. Жапаров*, Б.Б. Бисенов, Ж.С. Тулемисова

Қазақстан-Британ техникалық университеті, Алматы, Қазақстан

**Корреспонденция үшін автор: bo.zh@mail.ru*

Аңдатпа. Құрғақ метан риформингі (ҚМР) синтез газын өндірудің перспективалы тәсілі болып табылады. Белгілі болғандай, синтез газы биоотынның газ тәрізді түрі болып табылады және көміртегі тотығы мен сутегінің қоспасы болып табылады. Сутегі болашақта таза отын ретінде қолданылуы мүмкін. Бұл ғылыми-зерттеу жұмысының мақсаты Анабай газ кен орнының өндірілген табиғи газды ҚМР реакциясы арқылы синтездік газға айналдыру үшін пайдалану перспективаларын көрсету, сонымен қатар ҚМР бойынша зертханалық ғылыми тәжірибелер мысалында метаннан синтез газын алудың тәжірибелік мүмкіндіктерін зерттеу және көрсету болды. Метанды пайдалану және конверсиялау әлеуетін зерделеу үшін жер бетіндегі де, жер қойнауындағы да Анабай кен орнында өндірілген газдың метан құрамдас бөлігі туралы деректер пайдаланылды. Жер үсті газының сипаттамалары Фамен, Төменгі Визей, Орта Визей, Жоғарғы Визей және Серпухов кен орындарынан жиналған 56 ұңғыма сағасының сынамасы арқылы талданды. Жер қойнауының сынамалары Фамен, Турней, Төменгі, Орта және Жоғарғы Визей және Серпухов кезеңіндегі газдардың 102 үлгісінен алынды. Бұл деректер Анабай кен орнындағы метанның орташа мөлшері айтарлықтай жоғары екенін көрсетеді. Бұл мақалада 20Co-10Mg-20Al негізіндегі катализаторды пайдаланып эксперименттер кезінде алынған нәтижелер берілген. Бұл катализатор өздігінен таралатын жоғары температуралық синтез (ӨТЖТС) әдісі арқылы алынды. Алынған нәтижелердің практикалық маңыздылығын ескере отырып, іске асыру бойынша ұсынымдар беріліп, осы Анабай газ кен орнындағы метанның осындай түрленуінің болжамдары мен перспективалары да жасалды.

Негізгі сөздер: *газ кен орны, құрғақ метан риформингі, синтез газы, метан, сутегі.*

Перспективы использования природного газа газового месторождения Анабай для получения синтез-газа методом сухого риформинга метана

Б.Б. Жапаров*, Б.Б. Бисенов, Ж.С. Тулемисова

Казахстанско-Британский технический университет, Алматы, Казахстан

**Автор для корреспонденции: bo.zh@mail.ru*

Аннотация. Реакция сухого риформинга метана (СРМ) является перспективным подходом к получению синтез-газа – смеси водорода и оксида углерода, которая может использоваться в энергетических и химико-технологических процессах. В условиях глобального энергетического перехода водород рассматривается как потенциальный низкоуглеродный энергоноситель, при этом СРМ позволяет одновременно утилизировать метан и диоксид углерода. Целью данной работы является оценка перспектив газового месторождения Анабай для преобразования добываемого природного газа в синтез-газ с использованием реакции сухого риформинга метана, а также демонстрация практической реализуемости данного процесса на основе лабораторных экспериментов. Для оценки потенциала использования метана были проанализированы данные по его компонентному содержанию в природном газе месторождения Анабай в поверхностных и глубинных условиях. Характеристика газа в поверхностных условиях выполнена на основе 56 устьевых проб, отобранных из фаменских, нижневизейских, средневизейских, верхневизейских и серпуховских отложений. Глубинные пробы представлены 102 образцами газа из фаменского, турнейского и визейско-серпуховского ярусов. Полученные данные свидетельствуют о стабильно высоком содержании метана во всех исследованных стратиграфических горизонтах. Экспериментальные исследования СРМ были проведены с использованием катализатора состава 20Co-10Mg-20Al, синтезированного методом самораспространяющегося высокотемпературного синтеза (СВС). Каталитическая активность оценивалась по степени превращения метана и диоксида углерода, составу синтез-газа и температурной зависимости процесса. Предложены рекомендации по внедрению технологии сухого риформинга метана на газовом месторождении Анабай, а также рассмотрены перспективы интеграции данного подхода в экологически ориентированные энергетические схемы.

Ключевые слова: *газовое месторождение, сухой риформинг метана, синтез-газ, природный газ, метан, водород.*

SATBAYEV UNIVERSITY

Engineering Journal of Satbayev University

Volume 147 (2025), Issue 6, 48-52

https://doi.org/10.51301/ejsu.2025.i6.06

Snowmelt water breakthrough into coal mine

N.A. Miletenko*, V.N. Odintsev, E.V. Fedorov

Institute of Comprehensive Exploitation of Mineral Resources Russian Academy of Sciences, IPKON RAS, Moscow, Russia

**Corresponding author: nmilet@mail.ru*

Abstract. The paper addresses the mechanism of flood water inrush from a technogenic ground sinkhole into underground excavation. Basing on computer simulation it was demonstrated that an area of tensile stresses is formed in the zone affected by underground mining. A natural hydrofracture of rocks may develop from the sinkhole into the mine opening under the effect of tensile stresses and water hydrostatic pressure. Hazardous water inflow into underground mine opening may be associated both with direct hydrofracture crack egress into the opening and with preliminary intense filtration water inflow from the crack into the opening if the crack development slows down. On approaching the mine opening the fracture may stop growing due to local rock compression near the opening. The modeling has demonstrated that the actual picture of the catastrophic water inflow into the ventilation gallery cannot be explained by filtration mechanism only. The catastrophic water breakthrough may be caused by development of a major water-conducting crack growing from natural frost crack in the bottom of the sinkhole towards the mine opening.

Keywords: *underground mining, ground surface, sinkhole, floodwater, technogenic rock stresses, natural hydrofracture, filtration, water inrush.*

Received: 11 August 2025
Accepted: 15 December 2025
Available online: 31 December 2025

1. Introduction

Emergency situations caused by spontaneous hydrological events show a continuous trend towards increasing frequency and scale of consequences [1]. Major economic damage from floods due to snow melting is inflicted on engineering constructions on earth surface. However, under certain conditions meltwater may affect safety of underground mining. There are a variety of mechanisms of this impact. As a rule, they are associated with general increase in rock mass water saturation and intensification of filtration.

Underground mining of solid mineral resources at small depths is sometimes accompanied by local sinking of earth surface with rupture of rock continuity referred to as technogenic ground fall-through. The fall-through is caused by a shift of undermined rock into the opening. In Russia design and construction of buildings in such cases are done in accordance with appropriate codes of practice to avoid adverse effects [2].

The surface sinkholes are often filled with water. In this case, besides the dangerous geomechanical impact on mining safety, the sinkhole becomes a source of hydrogeological hazard as a reservoir of water that can breakthrough into the underground mine opening. The water breakthrough into the underground opening may proceed by various mechanisms depending upon rock mass geological structure, features of its stress state and water pressure. Water inflow into the underground opening from a surface reservoir in a rather homogeneous and well-penetrable rock mass may proceed by a water filtration mechanism [3, 4]. Another mechanism of water penetration into the underground opening may take place in rock mass with horizontal layers. In this case rock undermining is associated with generation of vertical rock mass tension, bending and disclosing of layer contacts, water filling of the layer contacts, rupture of some layers due to critical bending deformation, which results in water penetration into the opening [5, 6].

If vertical pressure of overlying rock is about twice as high as natural horizontal stress (this situation is characteristic of sedimentary rock in regions with rather calm geodynamical environment), fields of tensile horizontal technogenic stress may be generated in the undermined rock. Tensile cracks may develop and become filled with water in such regions. This water as a factor of force may play an active role in crack development due to pressure on the crack sides. Such fracture cracks may become major canals for water breakthrough into openings both from surface and underground reservoirs [7].

In subarctic regions water breakthroughs may also be caused by generation of so-called frost cracks due to extremely low negative temperature. The generation of frost cracks descending into depth up to ten meters is characteristic of subarctic regions and is not associated with mining activities. These cracks may be considered natural objects affecting subsequent technogenic geomechanical and hydrogeological processes in the rock [8].

Another mechanism for water breakthroughs from the sinkhole to the opening related to both to crack generation

nmilet@mail.ru; Odin-VN@yandex.ru; evfedorov58@gmail.com
Engineering Journal of Satbayev University. eISSN 2959-2348. Published by Satbayev University

and filtration flow is considered below on the example of the Yun-Yaga coal mine. As known, study of practical experience is the best way to understand specific mechanisms of events and to develop adequate methods for prediction of similar cases in future.

2. Water breakthrough from a sinkhole into a ventilation gallery at the Yun-Yaga mine

The now closed Yun-Yaga mine was used to extract coal from the Yun-Yaga coal deposit located in north-eastern part of the Pechora coal basin [9]. The climate of this region is subarctic with sharp temperature and pressure variations. Average temperature for a many-year period of observation is minus 6.3°C with absolute minimums of -42 to -52°C and maximums of +30 to +32°C.

The Yun-Yaga deposit is located in a region involving a zone of many-year frozen ground. The zone is 50-60% of the whole area, and there are multiple through taliks in the remaining portion, the zone maximum thickness is 180-200 m (average 50-70 m, predominant values up to 20-30 m), temperature ranges from -0.5 to -3.0°C. The through many-year taliks are as a rule located under large undrained lakes, the Yun-Yaga river, some streams and in a region of sinkholes.

The mine field geological structure has several water bearing sandstone layers located in roofs of coal seams under operation. The deposit natural hydrogeological conditions are impaired due to mine construction. The mine construction was accompanied by large water inflow (reaching 720 m^3/h). The underground water state underwent considerable change by the end of the construction. A large depression funnel was generated that reached and even went beyond the deposit outline involving the Yun-Yaga river-valley. The total decrease in the underground water level in main water-bearing horizons was 65 to 130 m.

A water breakthrough occurred from a rather small surface sinkhole into a ventilation gallery located at about 30m below the sinkhole. The sinkhole was formed in the area of influence of the excavation. However, the sinkhole had no hydrological connection with the ventilation gallery, which was explained by sufficiently plastic properties of the overlying rocks and rapid closing of induced cracks [10].

Water from the ventilation gallery penetrated further into the lava and the conveyor drift. Jumpers and water-resistant doors did not give effect due to water filtration through the surrounding rock mass and concrete partitions. Lack of power and flooding of the pumping stations led to flowage [11].

The breakthrough occurred during the period of high level of melt water (above 0.5 m) due to complete thawing of the overlying rock strata after their partial freezing in winter. The causes of the flood included limited water runoff and insufficient conveyance capacity of the hydrotechnical construction (bridge). The water breakthrough into the ventilation gallery began with weak dripping of water from the roof of the gallery, which turned into strong dripping with erosion and fall of loose roof rock and intense flow of water from the roof.

The coal seam thickness was 1.9 m and inclination was 10° (Figure 1). The immediate roof was a 1m siltstone layer of 40 MPa strength; the main roof was a sandstone layer about 14 m thick and 70-90 MPa strong. The overlying rock mass in weathering area was weakened by oxidation process and individual frost cracks.

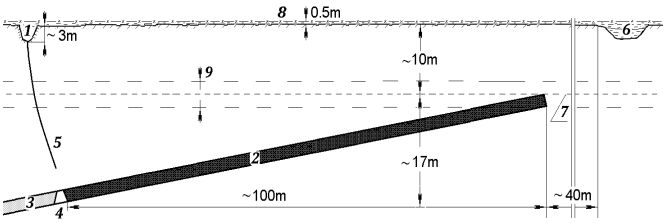

Figure 1. Scheme of water breakthrough in the Yun-Yaga mine: 1 –sinkhole; 2 – coal pillar; 3 – worked-out seam; 4 – ventilation gallery; 5 – water-conducting crack; 6 – river; 7 – coal seam egress under the bedrock, 8 – flood level at the event occurrence, 9 – natural talik

Check-up at the mine reported the following causes of the event:

a) absence of preventive activities such as sinkhole filling;

b) inadequate activities for isolation of the opening from the surface;

c) absence of hydrotechnical installations to prevent river overflow and water penetration into mining field at the seam egress under the overburdens;

d) insufficient conveyance capacity of the bridge over the river during water floods;

e) flood water rise higher than the maximum expected level, outflow beyond the protective pillar and breakthrough via the sinkhole into the ventilation gallery;

f) development of frost cracks;

g) development of a sinkhole in the earth surface along the frost cracks under the effect of flood water;

h) unfavorable complex of natural factors such as early and strong frost, deep freezing, small snow cover, short and violent spring water flood.

These causes were not supported by any calculations and were to a certain degree contradictory. For instance, a frost crack cannot be deeper than ten meters. The season-associated temperature variance has no effect at such a depth due to the talik impact. Development of the major crack should occur in another manner. Therefore, this event was considered abnormal and requiring a special examination.

3. Modeling of water breakthrough

An attempt was made to model the geomechanical and hydrogeological situation using the approach described in [12]. This approach assumes that the occurrence of a large water-supply crack is associated with the combined effect of technogenic pressure reduction of rocks and hydrostatic effect of water in the crack. The growing crack is actually a hydrofracture of the rock.

Since the initial geometric and geomechanical situation was not known in detail, different calculation schemes existed for the formulation of modeling problems. Each of the patterns included a rock mass up to 100 m deep and a 50-meter part of the excavations. On the part of the excavated seam (50 m in length) the resistance of the support to the movement of the overlying rocks was set by back pressure of 0.5 MPa. There was no back pressure in a small part of the excavation, including the ventilation gallery.

In the calculation the sinkhole was assumed to be an ellipsoid earth surface depression of about 3 m in depth, water pressure near the sinkhole bottom was 0.03 MPa. Since the sinkhole had no hydraulic connection with the mine

opening and the permafrost was absent in the considered area, rock mass was assumed to be homogeneous elastic solid medium with 10^3 MPa modulus of elasticity and Poisson's ratio of 0.3.

Rock pressure in the virgin rock mass was specified by the academician A.N. Dinnik hypothesis that vertical stresses were determined by weight of overlying rock (about 0.6 MPa at a 30 m depth), while side stresses depended upon Poisson's ratio of the rock. They were 0.25 MPa in the case considered.

The conditions of the absence of permafrost in the considered area of rock mass were considered. It was due to technogenic influence of mining and the influence of sinkhole. For this reason, the rock mass was considered an elastic medium without internal stress sources.

A variety of situations with initial crack starting from the sinkhole were considered including a small vertical frost crack beginning from the sinkhole bottom and a crack coming out from the sinkhole at an angle. As concerns crack growth two factors were considered, i.e. technogenic stress state of the rock mass and water pressure in the crack changing with depth by hydrostatics law.

Calculation of crack development was made by sequential steps according to the finite element method. Possibility of rock destruction at the crack end was assessed at each step by the Griffiths-Irwin criterion as described in. The vertical coordinate reflects the change in depth from the earth's surface. The horizontal coordinate defines the changes along the coal seam. If the criterion was met, a small length increment was specified along the direction of the highest tensile pressure of the rock. As a result of a sequence of calculation steps a trajectory was found for crack development from the sinkhole to the ventilation gallery due to rock natural hydrofracure.

4. Results and discussion

4.1. Stress-strain state and crack propagation

Figure 2 shows some results of stress calculation for a situation when a water-conducting crack approached the ventilation gallery (the distance from the crack end to the gallery was 2 m with a crack of 24 m in length). Figure 2a shows isolines of main stress which is the highest tensile stress leading to rock fracture. Figure 2b shows isolines of von Mises stress that allows assessment of the rock area of pre-destruction. Rock permeability is known to increase rapidly in this area [13].

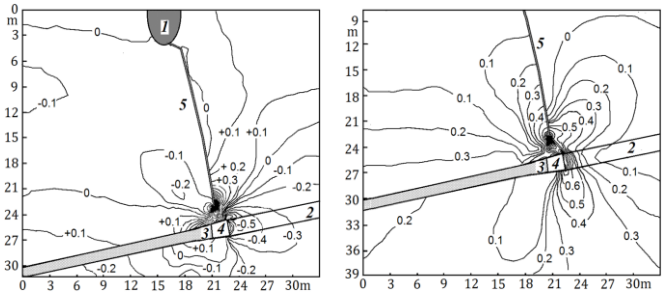

(a) (b)

Figure 2. Stress distribution in the rock mass during crack propagation toward the mine opening: (a) – isolines of the maximum tensile stress (MPa); (b) – isolines of the von Mises equivalent stress (MPa): 1 – sinkhole; 2 – coal seam; 3 – worked-out seam; 4 – opening; 5 – crack

Analysis of the stress-strain state of the rock mass near the end of the crack and the ventilation gallery shows that the crack can reach the roof of the gallery under some conditions or stop in its development under other conditions (due to the features of the geometry of the opening and the local compression of the rock). The first case is the situation with dynamic break of water into the crack at once, the second case reflects the possibility of water filtration into the opening.

4.2. Filtration flow and water breakthrough mechanism

The problem of filtration theory is solved to analyze the features of the filtration flow into the ventilation gallery, including the water filtration directly from the surface and sinkhole together with the water filtration from the water-conducting crack. The filtration coefficient of siltstone 0.001 m/s was used in the calculation

As follows from the calculations, for a crack less than 20 m in length the filtration flow of water from the surface and from the crack to the rock mass is extremely low. The situation changes when the crack approaches the mine opening. In this case interaction between the crack and the opening begins (Figure 3).

Figure 3a shows the situation for a 24 m long crack. In the figure the isolines of values of the filtration rate (m/s) are shown. These values must be multiplied by a correction factor of 10^{-3}. As seen, the filtration flow of water is strongly limited by the end of the crack. Figure 3b shows isolines in the immediate vicinity of the opening. These isolines are constructed on a different scale for a different finite element mesh to verify the correct calculation and to more accurately estimate the amount of possible water flow into the hole.

The assessment showed that the water flow through the free surface of 15 m^2 can reach about 50m^3 per hour. Such an intense water flow may really cause washout of weak rock in the roof of the ventilation gallery and partial roof fall into the opening with the major crack start and water breakthrough in the opening to follow, which was the actual case.

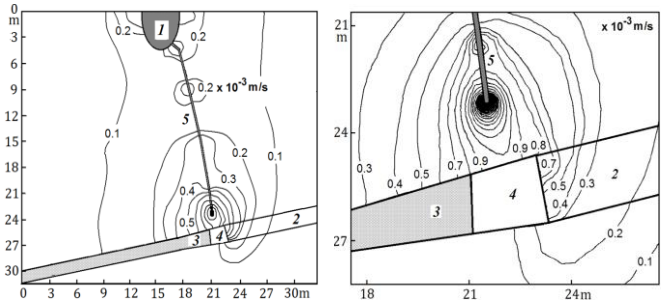

(a) (b)

Figure 3. Distribution of filtration flow in the rock mass during crack propagation toward the mine opening: (a) – isolines of filtration flow rate (m/s) for a crack length of 24 m; (b) – enlarged view of filtration flow isolines in the vicinity of the mine opening: 1 – sinkhole; 2 – coal seam; 3 – worked-out seam; 4 – opening; 5 – crack

The modeling has demonstrated that the actual picture of the catastrophic water inflow into the ventilation gallery cannot be explained by filtration mechanism only. The catastrophic water breakthrough may be caused by development of a major water-conducting crack growing from natural frost crack in the bottom of the sinkhole towards the mine opening.

It follows from the modeling that the major water-conducting crack may be considered as natural hydro fracture of rock mass in the area of low technogenic stress. Hydrostatic pressure in the crack increases during water flood and the crack may grow to a considerable depth. This factor is of much importance for a case when the sinkhole occurs near the border of projection of the undermined seam portion to earth surface.

So, possibility of water breakthrough into the mine opening is associated in some degree with a sinkhole of earth surface. Note that probability of occurrence of a technogenic sinkhole on the earth surface under conditions of simple geometry of mine opening and absence of geological faults may be assessed using a rather simple formula based on statistical analysis of data concerning the sinkholes [14]. For the case considered probability of sinkhole occurrence may be calculated by a rough formula:

$$q = (H/S^{1/2}), \quad (1)$$

where H is the excavation depth; S is transverse section of the mine opening.

If $q < 8$, the sinkhole is practically unavoidable; if $q > 16$ the sinkhole is very rare; if $8 < q < 16$ probability of a sinkhole is about 0.5. However, these relationships can hardly help in assessing details and consequences of the sinkholes especially when they are filled with water. To make such a study computer modeling of stress state and hydrogeological state of the rock mass should be used. Timely modeling of possible situations with due consideration of geomechanical and hydrogeological factors could help to predict hazardous situations and to prevent water breakthrough in the mine opening [15].

It should be noted however that in real conditions of block structure of the rock mass the induced deformations can form a more complex picture as established in [16]. Here we use the idea of rock mass with rheological properties. In this case the induced cracks are closing over time.

As follows from our modeling, the major rapidly growing crack may stop to develop near the mine opening. In this case a heavy local filtration inflow into the opening may occur. In practice such a local water filtration inflow in loose rock often leads to washout and fall of the rock from the roof of the opening. In the case considered the rock mass failure area reached the end of the water-conducting crack, which resulted in a powerful stream of water into the opening.

4.3. Implications for prediction of water breakthrough

The conclusion may be made that if water penetration into mine openings proceeds by the crack-and-filtration mechanism, heavy dripping from the opening wall and roof should occur before the catastrophic breakthrough. Therefore, one may predict the critical situation with breakthrough of the major portion of water into the mine opening and take preventive measures beforehand to reduce hazardous consequences of the water breakthrough.

Assessment of possibility of water breakthrough into underground openings in subarctic regions should involve assessment of possible effect of permafrost, which in general prevents water penetration into underground mine openings. However, one has to take into consideration that taliks may be generated in the rock mass under the effect of mining at small depth. In addition, the presence of natural and artificial water reservoirs on the surface further contributes to the generation of taliks. In this case the poorest conditions for water breakthrough into underground openings at small depth are formed due to spring thawing of subsurface rock.

5. Conclusions

The meltwater-filled sinkhole changes dramatically rock geomechanical state and makes conditions for generation of a hydrofracture crack to mine opening. Hazardous water inflow into underground mine opening may be associated both with direct hydrofracture crack egress into the opening and with preliminary intense filtration water inflow from the crack into the opening if the crack development slows down. In loose rock, an intense filtration inflow of water, which manifests itself by a very intense dripping of water from the roof of the mine, can be an indicator of the approaching washout of the rock and the flood of water from the water-conducting crack.

Author contributions

Conceptualization: NAM; Data curation: VNO; Formal analysis: VNO, EVF; Funding acquisition: VNO; Investigation: EVF, NAM; Methodology: NAM, EVF; Project administration: NAM; Resources: VNO, EVF; Software: EVF; Supervision: VNO, NAM; Validation: NAM; Visualization: NAM; Writing – original draft: NAM, VNO, EVF; Writing – review & editing: NAM, VNO, EVF. All authors have read and agreed to the published version of the manuscript.

Funding

This research received no external funding.

Acknowledgements

The authors express their sincere gratitude to the editor and anonymous reviewers for their constructive comments and valuable suggestions, which have significantly improved the quality of this manuscript.

Conflicts of interests

The authors declare no conflict of interest.

Data availability statement

The original contributions presented in this study are included in the article. Further inquiries can be directed to the corresponding author.

References

[1] The Ministry of the Russian Federation for Civil Defence, Emergencies and Elimination of Consequences of Natural Disasters. (2000). *Guidelines for the Organization and Carrying out of the Actions Directed on Reduction of Consequences of Spring Floods and Freshets*. Moscow

[2] The Ministry of Regional Development of the Russian Federation. (2011). *The Building Codes and Regulations «SNiP 2.01.09-91. Buildings and structures on the undermined territories and subsidence soil»*. Moscow

[3] Mironenko, V., & Strelsky, F. (1993). Hydrogeomechanical problems in mining. *Mine Water and the Environment*, *112*, 35-40

[4] Luckner, L., & Shestakov, V. (1991). *Migration Processes in the Soil and Groundwater Zone.* CRC Press, Boca Raton

[5] Iophis, M.A. (2002). The nature and mechanism of formation of water-conducting fractures in the rock mass. *Mining Informational and Analytical Bulletin*, *4*, 33-34

[6] Xing, M., Li, W., Wang, Q., & Yang, D. (2015). Risk Prediction of Roof Bed-Separation Water Inrush in Coal Mine, China. *Electronic Journal of Geothechnical Engineering*, *20*(1), 301-312

[7] Liu, Y., Liu, Q., Jin, Z., Cai, L., & Cui, X. (2014). A simulation study of support break-off and water inrush during mining under high confined and thick unconsolidated aquifer. *Open Journal of Geology*, *4*(12), 5990611. https://doi.org/10.4236/ojg.2014.412044
[8] Odintsev, V.N., & Miletenko, N.A. (2015). Water inrush in mines as a consequence of spontaneous hydrofracture. *Journal of Mining Science*, *51(3)*, 423-434
[9] Grechishchev, S.E., Chistotinov, L.V. & Shur, Y.L. (1984) *Fundamentals of modeling of cryogenic physical-geological processes. Nauka*
[10] Gorbachevskij, A.Y. (2007). Development of residual reserves of the Yunyaginsky deposit by the open method in the Arctic. *Mining Informational and Analytical Bulletin*, *1*, 258-265
[11] Kostarev, A.P., & Mitishova, N.A. (2000). Improving the effectiveness of measures to prevent water breakouts in coal mines. *Occupational Safety in Industry*, *1*, 35-38
[12] Miletenko, N.A. (2007). On the issue of water breakthroughs in underground mining. *Mining Informational and Analytical Bulletin*, *6*, 107-111
[13] Odintsev, V.N., & Miletenko, N.A. (2015). Water inrush in mines as a consequence of spontaneous hydrofracture. *Journal of Mining Science*, *51*(3), 423-434, https://doi.org/10.1134/S1062739115030011
[14] Stavrogin, A.N., & Protosenya, A.G. (1985). *Rock Strength and Stability of Mine Openings at Great Depths*. Nedra, Moscow
[15] Iophis, M.A. (2006). On the issue of forecasting and preventing the consequences of the collapse of tunnels. *Tunnel Association of Russia*. Moscow
[16] Iophis, M.A., Odintsev, V.N., Blokhin, D.I. & Sheinin, V.I. (2007). Experimental investigation of spatial periodicity induced deformation in a rock mass. *Journal of Mining Science*, *43*(2), 21-27

Еріген қар суларының көмір шахтасына енуі

Н.А. Милетенко*, В.Н. Одинцев, Е.В. Федоров

Ресей Ғылым академиясының пайдалы қазбаларды кешенді игеру институты (ИПКОН РҒА), Мәскеу, Ресей

**Корреспонденция үшін автор: nmilet@mail.ru*

Аңдатпа. Мақалада техногендік жер бетіндегі опырылмадан жерасты қазбасына тасқын суларының басып кіру механизмі қарастырылады. Компьютерлік модельдеу нәтижесінде жерасты кен өндіру әсер ететін аймақта созылу кернеулерінің аймағы қалыптасатыны көрсетілді. Созылу кернеулері мен судың гидростатикалық қысымының әсерінен жыныстардың табиғи гидрожарықшақтануы опырылмадан жерасты қазбасына қарай дамуы мүмкін. Жерасты қазбасына қауіпті су ағымы гидрожарықшақтың тікелей қазбаға жетуімен де, сондай-ақ жарықшақтың дамуы баяулаған жағдайда жарықшақтан қазбаға дейінгі алдын ала қарқынды сүзгілік су келуімен де байланысты болуы мүмкін. Қазбаға жақындаған кезде жыныстардың жергілікті сығылуына байланысты жарықшақтың өсуі тоқтауы ықтимал. Модельдеу нәтижелері вентиляциялық штрекке болған апатты су басуды тек сүзгілік механизммен ғана түсіндіру мүмкін еместігін көрсетті. Апатты су прорывы опырылма түбіндегі табиғи аяздық жарықшақтан басталып, жерасты қазбасына қарай өсетін ірі су өткізгіш жарықшақтың дамуына байланысты болуы мүмкін.

Негізгі сөздер: *жерасты пайдалы қазбаларды өндіру, жер беті, опырылма (карсттық ойыс), тасқын сулары, тау жыныстарындағы техногендік кернеулер, табиғи гидрожарықшақтану, сүзгілеу (фильтрация), су басып кіру*.

Прорыв талых снеговых вод в угольную шахту

Н.А. Милетенко*, В.Н. Одинцев, Е.В. Федоров

Институт комплексного освоения недр Российской академии наук (ИПКОН РАН), Москва, Россия

**Автор для корреспонденции: nmilet@mail.ru*

Аннотация. В работе рассматривается механизм прорыва паводковых вод из техногенного провала земной поверхности в подземную выработку. На основе компьютерного моделирования показано, что в зоне влияния подземных горных работ формируется область растягивающих напряжений. Под действием растягивающих напряжений и гидростатического давления воды может развиваться естественный гидроразрыв горных пород от провала к горной выработке. Опасный приток воды в подземную выработку может быть связан как с непосредственным выходом трещины гидроразрыва в выработку, так и с предварительным интенсивным фильтрационным притоком воды из трещины в выработку в случае замедления развития трещины. При приближении к выработке рост трещины может прекращаться вследствие локального сжатия пород вблизи выработки. Моделирование показало, что реальная картина катастрофического притока воды в вентиляционную галерею не может быть объяснена только фильтрационным механизмом. Катастрофический прорыв воды может быть обусловлен развитием крупной водопроводящей трещины, растущей от естественной морозной трещины в днище провала в сторону подземной выработки.

Ключевые слова: *подземная добыча полезных ископаемых, земная поверхность, провал (карстовая воронка), паводковые воды, техногенные напряжения в горных породах, естественный гидроразрыв, фильтрация, прорыв воды*.

Publisher's note

All claims expressed in this manuscript are solely those of the authors and do not necessarily represent those of their affiliated organizations, or those of the publisher, the editors and the reviewers.

CONTENTS

МАЗМҰНЫ

СОДЕРЖАНИЕ

Учредитель: Satbayev University

Регистрация:
Министерство информации и общественного развития Республики Казахстан
№ KZ19VPY00056529 от 30.09.2022

Официальный сайт: https://vestnik.satbayev.university/index.php/journal/

Основан в августе 1994 г. Выходит 6 раз в год

Адрес редакции:
г. Алматы, ул. Сатпаева,
22 тел.: 292-63-46